Doctorate Thesis

Study of the mechanism of coronal heating based on the statistical analysis of occurrence frequency distributions of solar flares

太陽フレア発生頻度分布の統計解析によるコロナ加熱機構に関する研究

By:
Toshiki Kawai

Supervisor:
Prof. Kanya Kusano

Nagoya University
January 2022

Abstract

To understand the mechanism of coronal heating, it is crucial to derive the contribution of small-scale flares, the so-called nanoflares, to the heating up of the solar corona. The power-law index of the occurrence frequency distribution of flares as a function of energy is one of the most important indicators for evaluating the contribution of small-scale flares to coronal heating. Over the past several decades, many attempts have been made to derive the power-law index using various instruments and methods. However, previous studies have some problems in their analysis. First, nanoflares cannot be distinguished from observation images because several nanoflares are overlapped in the line-of-sight direction. Second, previous studies generally estimated flare released energy based only on an X-ray and EUV thermal energy. Third, the results have varied significantly and the cause of this uncertainty is unknown owing to the diverse observation conditions.

To overcome the first problem, we introduce a new method to analyze small-scale flares statistically with taking into account the following conditions: (1) evolution of the coronal loop plasma heated by small-scale flares, (2) loops smaller than the spatial resolution of the observed image, and (3) multiwavelength observation. Our new method is based on a one-dimensional loop simulation and a machine-learning technique, that is, the genetic algorithm. First, we obtain six channels of Solar Dynamics Observatory (SDO)/ Atmospheric Imaging Assembly (AIA) light curves of the active-region coronal loops. Second, we carry out many coronal loop simulations and obtain the SDO/AIA light curves for each simulation in a pseudo-manner. Third, using the genetic algorithm, we estimate the best combination of simulated light curves that reproduce the observation. Consequently, the observed coronal loops are heated by small-scale flares with energy flux larger than that typically required to heat up an active region intermittently. Moreover, we derive the occurrence frequency distribution which has various power-law indices in the range from 1–3, which partially supports the nanoflare heating model. In contrast, we find that 90% of the coronal heating is done by flares that have energy larger than 10^{25} erg.

To solve the second problem, we statistically estimate the conversion rate of the energy released

during an active region transient brightening to Doppler motion and thermal and nonthermal energies. We used two types of data sets for the energy estimation and detection of transient brightenings. One includes spectroscopic images of Fe XIV,Fe XV, and Fe XVI lines observed by the Hinode/EUV Imaging Spectrometer. The other includes images obtained from the 211 Å channel of the SDO/AIA. As a result, the released Doppler motion and nonthermal energies were found to be approximately 0.1%–1% and 10%–100% of the change in the amount of thermal energy in each enhancement, respectively. Using this conversion rate, we estimated the contribution of the total energy flux of AIA transient brightenings to the active region heating to be at most 2% of the conduction and radiative losses.

According to the third problem, we investigated the dependence of the index on the solar activity, coronal features, released energy range, and active region properties such as magnetic flux, twist, and size. Our findings are as follows: (1) The power-law index in each year derived from time series of total solar irradiance (Sun-as-a-star observation) exhibits a negative correlation with the sunspot number. (2) The power-law index in the active region is smaller than that of the quiet Sun and coronal holes. (3) The power-law index is almost constant in the energy range of $10^{24} \lesssim E \lesssim 10^{30}$ erg. (4) Active regions that have greater magnetic free energy density, unsigned magnetic flux, and shear angles tend to have smaller power-law indices. Based on the results, we suggest that the active regions are more heated by magnetic reconnections, whereas the quiet Sun is mainly heated by Alfvén waves. Moreover, the ratio of nanoflare and wave heating is dependent on the magnetic properties, even among active regions.

Finally, we statistically investigated the contribution of impulsive heating to the active region heating. As a result, the heating flux of detected events is approximately from 0.01% to 1% of the radiation and conductive losses. Even considering the contribution of Doppler motion and nonthermal energies, the heating rate is only 2% of the requirement at most. Based on our suggestion, the remaining 98% of energy flux should be mainly provided by Alfvén waves. To supply the sufficient energy, the power-law distribution should be maintained at least 10^{19} – 10^{22} erg with the index greater than 2.

Acknowledgements

Foremost, I would like to express my sincere gratitude to my advisors: Prof. Kanya Kusano and Prof. Shinsuke Imada. I would have never complete this study without their assistance and knowledges.

Besides my advisors, I would like to thank Dr Haruhisa Iijima for his fruitful suggestions and supports for computers. I thank to Prof. KD Leka, Assoc. Prof. Satoshi Masuda, Assoc. Prof. Kyoko Watanabe, Dr. Satoshi Inoue, Dr. Sung-Hong Park, Dr. Yumi Bamba, Dr. Takafumi Kaneko, Dr. Takuma Matsumoto, Dr. Hisashi Hayakawa, Dr. Tomoya Iju, Dr. Takuya Shibayama, Dr. Pei-Hsuan Lin, Dr. Shohei Nishimoto, and Mr. Masashi Fujiyama for their supports and discussions. Also, I thank to all secretaries in Integrated Studies group in ISEE for helping my business trip and life in lab.

I would like to thank my thesis committee members for all of their guidance through this process; your discussion, ideas, and feedback have been absolutely invaluable.

I would like to acknowledge the Program for Leading Graduate Schools, "PhD Professional: Gateway to Success in Frontier Asia" by the Ministry of Education, Culture, Sports, Science and Technology for giving me chance to acquire various skills and participate overseas trainings. My work was supported by a Grant-in-Aid for 17K14401, 15H05816, and JSPS Fellows. A part of My work was carried by using the computational resource of the Center for Integrated Data Science, ISEE, Nagoya University.

Hinode is a Japanese mission developed and launched by ISAS/JAXA, in collaboration with NAOJ as a domestic partner and NASA and STFC (UK) as international partners. Scientific operation of the Hinode mission was conducted by the Hinode science team organized at ISAS/JAXA. This team mainly consists of scientists from institutes in partner countries. Support for the post-launch operation is provided by JAXA and NAOJ (Japan), STFC (U.K.), NASA (U.S.A.), ESA, and NSC (Norway). The Solar Dynamics Observatory is a part of NASA's Living with a Star program.

Finally, my thanks go to all the people who have supported me to complete the research work directly or indirectly.

Contents

List of Figures

List of Tables

Acronyms

AIA	The Atmospheric Imaging Assembly
AR	Active Region
CH	Coronal Hole
DEM	Differential Emission Measure
EIS	The EUV imaging spectrometer
EUV	Extreme Ultraviolet
GA	Genetic Algorithm
GOES	Geostationary Operational Environmental Satellite
HMI	The Helioseismic Magnetic Imager
NEI	Non-Equilibrium of Ionization
NOAA	National Oceanic and Atmospheric Administration
QS	Quiet Sun
SDO	The Solar Dynamics Observatory
SHARP	Spaceweather HMI Active Region Patch
SSW	Solar Software

Chapter 1

General Introduction

1.1 Coronal Heating Problem

The surface of the sun, called the photosphere, has a temperature of about 6,000 K. The temperature gradually decreases as it goes up, and reaches the lowest temperature layer at an altitude of about 500 km from the surface. However, above that, at altitudes of 1,000 to 2,000 km, there is a layer called the chromosphere with a temperature of about 10,000 K. Moreover, there is a tenuous atmosphere called the corona, which has a temperature of over 1 MK. The temperature changes rapidly in the thin region between the chromosphere and the corona, which is called the transition layer. On the other hand, the density decreases with the altitude, which is about 10^{17} cm^{-3} at the photosphere, while it is about 10^{9} cm^{-3} in the corona. Figure 1.1 shows the altitude profile from the surface with respect to temperature (dashed line) and density (solid line).

	QS	CH	AR
Conduction flux	2×10^5	6×10^4	10^5 - 10^7
Radiative flux	10^5	10^4	5×10^6
Solar wind flux	$\lesssim 5 \times 10^4$	7×10^5	$< 10^5$
Total	3×10^5	8×10^5	10^7

Table 1.1: Energy loss flux of the corona [erg cm^{-2} s^{-1}] estimated by Withbroe & Noyes (1977).

Understanding the mechanism of the heating up of the solar corona to a few million Kelvin or above is one of the long-standing problems in solar physics. Table 1.1 represents energy loss rate of

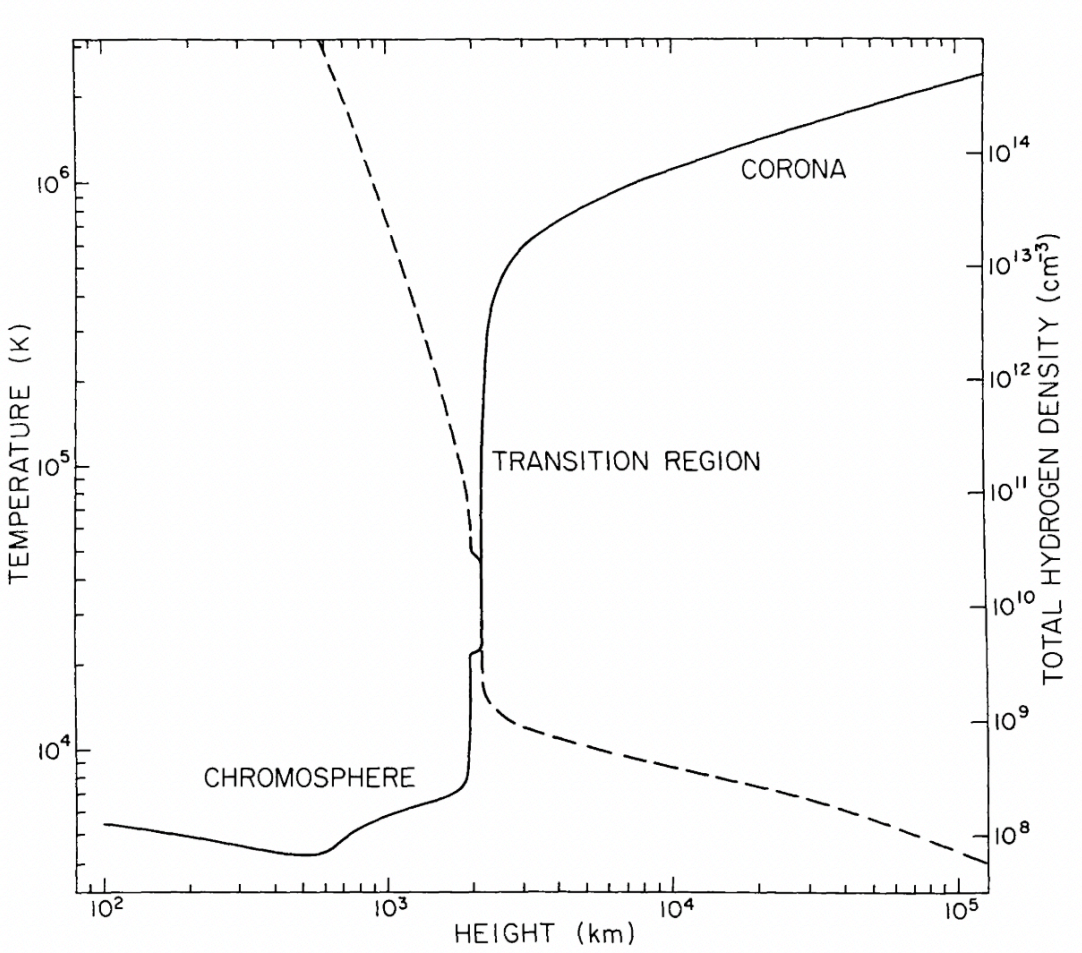

Figure 1.1: The altitude profile of a solar corona from the surface. The dashed and solid lines represent temperature and density, respectively (Withbroe & Noyes, 1977).

the corona in each segment estimated by Withbroe & Noyes (1977) based on the EUV and X-ray observations. Solar wind loss dominates the loss in CHs, while the conduction and radiation losses are dominant in ARs. In order to maintain a hot corona, energy flux equivalent to these losses must be injected. On the other hand, the turbulent and convective energies from the photosphere are estimated to be 10^9 erg cm^{-2} s^{-1}, indicating that 0.01-1% of these energies should be used to heat the corona.

To date, two primary mechanisms have been proposed to explain how the corona is heated, small-scale magnetic reconnection and wave dissipation. In the former model, the corona heats up due to small-scale impulsive heating events, so-called nanoflares ($E \simeq 10^{24}$ erg), which are related to coronal magnetic reconnections (*e.g.,* Parker, 1988). These magnetic stress dissipations are referred to as direct current (DC) heating. In the wave dissipation model, the corona heats up due to Alfvén waves propagated from the surface, which are excited due to convection (*e.g.,* Antolin & Shibata, 2010). This heating process is referred to as alternating current (AC) heating. In recent years, much progress has been made in regard to theories and observations for both models; however, a definitive solution to this problem is yet to be achieved (*e.g.,* Klimchuk, 2006, 2015). From the perspective of the nanoflare model, quantifying the contribution of small-scale flares in the heating up of the corona is crucial to understand their contribution to coronal heating.

1.2 Solar Flares

Before introducing nanoflare heating, we briefly describe general solar flares in this section. A solar flare, which is a sudden brightening observed in almost all wavelengths from radio waves to gamma rays, was first observed by Richard Carrington in 1859 (Carrington, 1859). Nowadays, it is believed that solar flare is a result of the rapid release of magnetic energy stored in the solar corona mainly occurs above a sunspot. A typical sunspot is composed of a pair of positive and negative magnetic fields, and arch-shaped magnetic field lines (coronal loops) exist at their feet. One standard model of flares that is based on magnetic reconnection is the CSHKP model (Carmichael, 1964, Hirayama, 1974, Kopp & Pneuman, 1976, Sturrock, 1966). In this model, a magnetic reconnection occurs above a coronal loop, and of the accelerated plasma, downward flows heat the loop with forming the shock, and upward flows cause a plasmoid eruption. Figure 1.2 shows a schematic diagram of a solar flare based on the CSHKP model. The characteristics predicted based on these models have been verified by modern observations (*e.g.*, cusp-like structure in soft X-ray images Tsuneta et al. (1992), hard X-ray sources above the flare loop Masuda et al. (1994), chromospheric evaporation Imada et al. (2015), Teriaca et al. (2003), reconnection inflows Yokoyama et al. (2001), reconnection

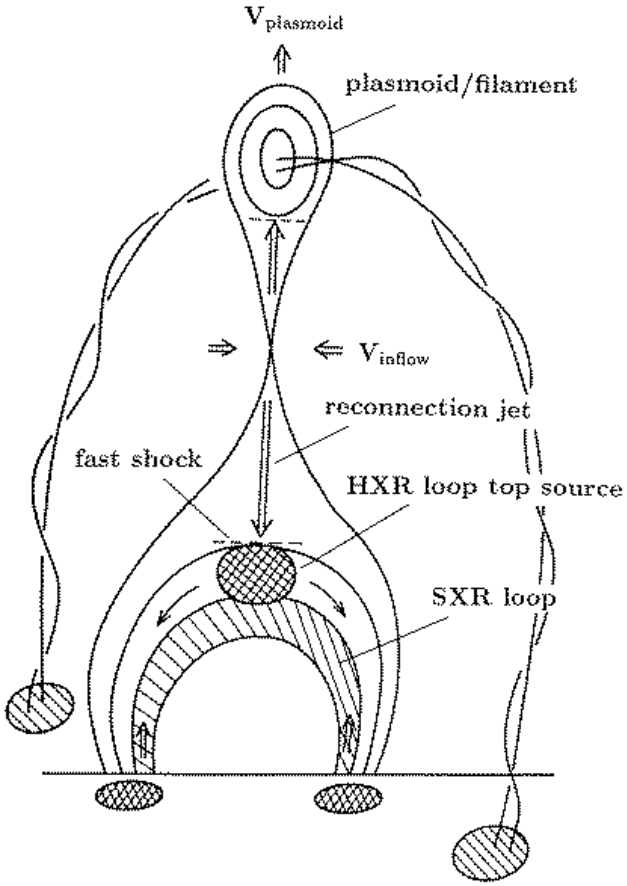

Figure 1.2: A schematic diagram of a solar flare based on CSHKP model (Shibata et al., 1995). A magnetic reconnection occurs above a loop structure which can be observed in soft X-rays. Hard X-rays are emitted from the loop top due to the shock formed by the reconnection. And plasma flows injected from the loop feet (chromospheric evaporation) and the upward plasma flow are shown.

outflows (off limb Imada et al. (2013), Innes et al. (2003), McKenzie & Hudson (1999), on disc Hara et al. (2011), plasmoid ejection Liu et al. (2013), Ohyama & Shibata (1998), and coronal mass ejections Imada et al. (2007), Svestka & Cliver (1992)). The energy released by a flare is very large, often reaching 10^{32} ergs within an hour. Such an extremely large event can cause serious problems such as communication failures, radiation exposure of astronauts, and satellite drag (Lean, 1997).

1.3 Nanoflare Heating Model

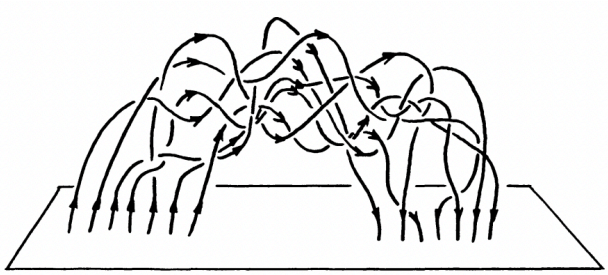

Figure 1.3: A schematic drawing of the cross section of the coronal loops (Parker, 1989).

Parker (1983, 1988) proposed that small-scale flares such as nanoflares are magnetic reconnections between the coronal magnetic fields tangled by the random motion of their foot points due to the convection of the surface as shown in Figure 1.3. However, recent studies, the term nanoflare means "an impulsive energy release on a small cross-field spatial scale without regard to physical mechanism" (Klimchuk, 2015). This change of terminology is caused by the prospect that waves can produce nanoflares (Klimchuk, 2006). Originally, Parker used the term of nanoflares to mention a brightening releases $E \simeq 10^{24}$ erg, which is approximately one billionth that of a large flare. Nowadays nanoflares are thought to have much smaller energy. Such small events are generally not resolved due to not only the lack of resolution and sensitivity but also the overlapping of event in the direction of the line of sight. Cargill (1994) reproduced the observed emission measure by modelling the active-region closed coronal loops as a bundle of numerous elemental loops that are randomly heated by nanoflares. Moreover, Schmelz et al. (2001) and Warren et al. (2008) suggested that a coronal loop is composed of finer tubes by spectroscopic observations. Each AR has probably upward of 100000 components.

A microflare was observed by the hard X-ray balloon observation in 1980 for the first time (Lin et al., 1984). After that, from the *Soft X-ray Telescope* (SXT: Tsuneta et al., 1991) onboard the Yohkoh satellite (Ogawara et al., 1991), it was revealed that many small explosive events occur in

ARs (Shimizu et al., 1994, 1992). (Testa et al., 2014) found a coronal nanoflare ($\lesssim 10^{25}$ erg) using IRIS (De Pontieu et al., 2014) observation. Current satellite observations cannot detect extremely small-scale flare due to lack of sensitivity and resolutions. On the other hand, a sounding rocket experiment, the High-resolution Coronal Imager (Hi-C: Kobayashi et al., 2014), detected a nanoflare that has $E \simeq 10^{23}$ erg at the foot point of a coronal loop in an AR by EUV observation (Testa et al., 2013). Moreover, another sounding rocket, the second flight of the Focusing Optics Solar X-ray Imager (FOXSI-2: Christe et al., 2016) detected the plasma of the upper 10 MK without any evident X-ray flare emissions (Ishikawa et al., 2017). This observation indicates that the plasma is heated by nanoflares. Such rocket experiments suggest the coronal heating by nanoflares, however, it is unable to statistically discuss whether or not there are sufficient nanoflares to heat the corona because the observation area and duration are very limited.

1.4 Energy Distribution of Flares

To validate the possibility of the coronal heating due to small-scale flares, it is necessary to derive the occurrence frequency distribution of flares as a function of the energy. It is known that the occurrence frequency of the flares is distributed as a power law with the following equation:

$$\frac{dN}{dE} = AE^{-\alpha} \tag{1.1}$$

where N, E, and α are the event number, energy of each event, and the power law index, respectively (Hudson, 1991). From this equation, the total energy released by all detected flares P can be calculated as

$$P = \int_{E_{\min}}^{E_{\max}} \frac{dN}{dE} E dE = \frac{A}{-\alpha + 2} \left(E_{\max}^{-\alpha+2} - E_{\min}^{-\alpha+2} \right) \tag{1.2}$$

where, A is a constant. Therefore, small-scale flares significantly heat up the corona when $E_{\min}$ is small enough and α is greater than 2.

In the case of solar and stellar flares in the energy range of $10^{27} \lesssim E \lesssim 10^{35}$ erg, α is estimated as approximately 1.8 (Collura et al., 1988, Datlowe et al., 1974, Dennis, 1985, Drake, 1971, Lin et al., 1984, Shakhovskaya, 1989), which does not support the nanoflare heating model. Recently, the power-law index of flares in smaller energy range was analyzed using various observational equipments and methods. Figure 1.4 represents examples of the derived occurrence frequency distribution of solar flares (Hannah et al., 2008). Shimizu (1995) reported that the power-law index to be 1.5 - 1.6 based on an AR study using the Yohkoh/SXT. Parnell & Jupp (2000) and

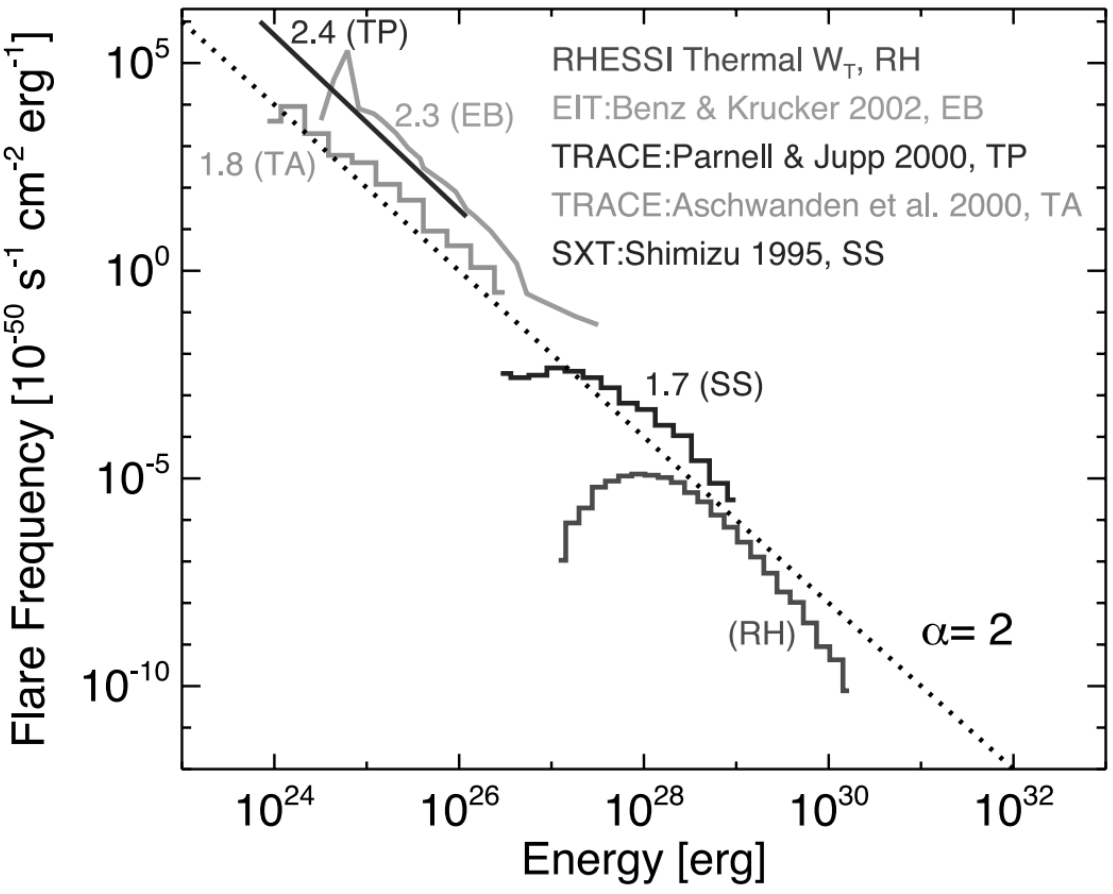

Figure 1.4: Examples of occurrence frequency distribution of solar flares as a function of energy. The dotted line indicates $\alpha = 2$ (Hannah et al., 2008).

Aschwanden et al. (2000) derived indices using the EUV telescope of the *Transition Region And Coronal Explorer* (TRACE: Handy et al., 1999). As a result, whereas Parnell & Jupp (2000) implied that the power-law index is greater than 2, Aschwanden et al. (2000) reported the index to be approximately 1.8. Moreover, certain studies suggested that the power-law index is greater than 2 (*e.g.,* Benz & Krucker, 2002), whereas others found that it is smaller than 2 (e.g., Jess et al., 2019, Tajfirouze et al., 2016). Table 1.2 represents the methods and results of these studies. Owing to the diverse instruments, observation dates, regions of interest, and energy ranges, the cause of the differences in the results remains unidentified. Ulyanov et al. (2019) surveyed the difference in the energy distribution of flares between the solar minimum and rising phase of cycle 24 in the quiet Sun (QS). The results demonstrated that the power-law index at the solar minimum ($\alpha \simeq 2.8$) is greater than that of the rising phase ($\alpha \simeq 2.3$). However, as they used different instruments (TESIS/CORONAS-PHOTON for the solar minimum and SDO/AIA for the rising phase), it is not clear whether this difference was actually owing to solar activity.

The energy distribution of stellar flares has also been investigated using various instruments for many years, with diverse results ($1.6 \lesssim \alpha \lesssim 2.7$; *e.g.,* Kashyap et al., 2002, Maehara et al., 2012, Shibayama et al., 2013, Wu et al., 2015). Wu et al. (2015) suggested that stars with a shorter rotation period have a larger power-law index according to their investigation of G-type stars observed by the *Kepler Mission* (Koch et al., 2010). However, Aschwanden & Güdel (2021) reported that the power-law index does not exhibit time variability and dependence on the stellar spectral types. Unlike stellar cases, to the best of our knowledge, no studies have focused on revealing the cause of uncertainty of the power-law index for solar flares.

Similar to the results of observational studies, the power-law indices that have been estimated by numerical simulations have also varied. Kanella & Gudiksen (2018) performed a three-dimensional magnetohydrodynamic (3D MHD) simulation of a loop-like magnetic structure. The obtained power-law index of the identified joule heating events was approximately 1.41 in the energy range of $10^{20} \lesssim E \lesssim 10^{28}$ [erg]. Bingert & Peter (2013) also employed 3D MHD simulation of an observed AR. The obtained distribution was not a single power-law and they fitted it as a double power-law distribution. The power-law index was 1.2 and 2.5 in the energy range of $10^{21} \lesssim E \lesssim 10^{24}$ and $10^{24} \lesssim E \lesssim 10^{26}$ [erg], respectively.

1.5 Scientific Objective

The power-law index of occurrence frequency distribution of flares is one of the most important indicators for evaluating nanoflare heating model. Therefore, many studies tried to derive the

Study	Instrument	Region	Energy range [erg]	Power-law index
Shimizu (1995)	Yohkoh/SXT	AR	$10^{27.0}$ – $10^{29.0}$	1.5-1.6
Berghmans et al. (1998)	SOHO/EIT	QS	$10^{25.5}$ – $10^{27.0}$	1.8-2.0
Parnell & Jupp (2000)	TRACE	QS	$10^{24.0}$ – $10^{27.0}$	2.0-2.6
Aschwanden et al. (2000)	TRACE	Mostly AR	$10^{24.0}$ – $10^{26.0}$	1.8
Benz & Krucker (2002)	SOHO/EIT	QS	$10^{24.5}$ – $10^{26.5}$	2.0-2.6
Jess et al. (2019)	SDO/AIA	AR	$10^{22.0}$ – $10^{25.0}$	1.8-1.9

Table 1.2: Some previous studies derived power-law index of solar flares.

power-law index using various instruments, observation dates, regions of interest. However, the indices estimated by previous studies are inconsistent, and the true index and the cause of such a difference are unknown.

Previous studies have some problems in their analysis. First, as described in Section 1.3, small-scale events such as nanoflares cannot be distinguished from observation images because several nanoflares are overlapped in the line-of-sight direction. However, most of previous studies did not take into account this fact for their observations. Tajfirouze et al. (2016) derived power-law index with considering the overlapping events using probabilistic neural network, but they only used 0D simulation and surveyed parameters are very limited. Therefore, in Chapter 2, using a GA, we derived the power-law index of flares occurred in an AR with taking into account (1) time evolution of coronal loop plasma heated by small-scale flares in 1D model, (2) overlapping events in the direction of the line-of-sight, and (3) multiwavelength observation.

Second, previous studies generally estimated flare released energy based only on an X-ray and EUV thermal energy. But the contributions of other components (nonthermal and Doppler motion energy) are unknown. Therefore, in Chapter 3, we estimated the energy conversion rate of small-scale events using spectroscopic observation. We also derived power-law indices as functions of not only thermal energy but also of nonthermal and Doppler motion energy. We investigated the contribution of these flares to the coronal heating for each energy component.

Finally, the variety of observation conditions obscures the actual power-law index. To reveal this uncertainty, it is essential to statistically investigate the power-law index in consistent observation manner. In Chapter 4, we surveyed the dependences of the power-law index on the solar activity, coronal features, released energy, and AR properties. From the results, we discuss the difference and similarity of heating processes in QS, quiet ARs, and active ARs.

Chapter 2

Energy Distribution of Small-scale Flares Derived Using a Genetic Algorithm

2.1 Introduction

Parker (1983, 1988) proposed that small-scale flares such as microflares and nanoflares are magnetic reconnections between the coronal magnetic fields tangled by the random motion of their foot points due to the convection of the surface. Cargill (1994) succeeded in reproducing the emission measure observation of *skylab* and *pre-skylab* by modelling the active-region closed coronal loops as a bundle of numerous elemental loops that are randomly heated by nanoflares. From the spectroscopic observations, Schmelz et al. (2001) and Warren et al. (2008) reported that a coronal loop consists of plasma that has a wide range of temperatures, which suggest that coronal loop is composed of finer tubes. The volumetric filling factor of the loop is estimated as approximately 10% by Warren et al. (2008). Vekstein & Katsukawa (2000) proposed the assumption that the cross-sectional area of each elemental loop can be derived from the balance between the plasma pressure inside the loop and the outer magnetic pressure. Based on this assumption, Sakamoto et al. (2009) revealed that the major differences between the soft X-ray (> 2 MK) and EUV ($\simeq 1$ MK) nanoflare-heated coronal loops are their magnetic field strength (40 G for soft X-ray and 8 G for EUV) and released energies of nanoflares (10^{24} – 10^{25} erg for soft X-ray and 10^{23} erg for EUV). They also estimated the volumetric filling factors of the loops as approximately 10% and 70% for soft X-ray and EUV,

respectively.

By using the 0-dimensional hydrodynamic coronal loop model EBTEL (Enthalpy Based Thermal Evolution of Loops Cargill et al., 2012, Klimchuk, 2015, Klimchuk et al., 2008) and probabilistic neural network, Tajfirouze et al. (2016) estimated the power-law index α and the number of elemental loops in one pixel of the EUV channel of *Atmospheric Imaging Assembly* (AIA: Lemen et al., 2012) onboard the Solar Dynamics Observatory (SDO: Pesnell et al., 2012). They concluded that α is approximately 1.5 and that 1000 loops are included in one pixel of an active region. However, they analyzed only the case of $\alpha = 1.5$ and 2.5, and the range of flare heating rate was very narrow (approximately from 0.01 to 0.5 erg cm^{-3} s^{-1}). Moreover, the location where nanoflare occurs is neglected because they used the 0-dimensional model. According to the model of Parker (1988), nanoflares may occur anywhere along the coronal loop. The plasma evolution depends on the nanoflare location even in one-dimensional coronal loop model (*e.g.,* Reale & Orlando, 2008). Therefore, to improve on this point, at least, a one-dimensional model must be used for analysis. The modelling of a coronal loop has been done for a few decades (*e.g.,* Priest, 1978). Generally, it is assumed that the temperature and density are almost the same as the surrounding corona, the magnetic pressure is dominant ($\beta \ll 1$), the confined plasma is a compressible fluid, and the energy is transported only along the magnetic field lines (*e.g.,* Rosner et al., 1978, Vesecky et al., 1979). Therefore, the evolution of the coronal loop plasma can be described using a one-dimensional model only in case neglecting the curvature, twisting, currents, waves, and non-uniform cross-section (see review by Reale, 2014, for details).

In this chapter, we derive the occurrence frequency distribution of small-scale flares as a function of energy while considering the following:

1. Evolution of coronal loop plasma heated by small-scale flares in the one-dimensional model
2. Elemental loops smaller than the spatial resolution of the observed image
3. Multiwavelength observation

As far as we know, there are few studies that derive the frequency distributions of small-scale flares with taking into account all the above conditions. We succeeded in carrying out such an analysis by using one of the machine learning techniques called genetic algorithm (GA), which is effective at optimizing parameter combinations.

This chapter is organized as follows: The active region observation, which we applied in our new method, is shown in section 2.2. We describe the set of small-scale flare heating coronal loop simulations in section 2.3. In section 2.4, we present how we derive the flare parameter and energy

distribution by using GA. Section 2.5 gives the obtained results. Finally, we summarize this paper and discuss the validity of our method and the nanoflare heating model in section 2.6.

2.2 Data and Observations

In this study, we use the coronal EUV images of NOAA active region 12712 between 03:00 and 04:00 UT on 30 May 2018, using six filters of the SDO/AIA, which consists of 94 ($\log T \simeq 6.8$), 131 ($\log T \simeq 7.0$), 171 ($\log T \simeq 5.8$), 193 ($\log T \simeq 6.0$ for quiet region and $\log T \simeq 7.3$ for flaring region), 211 ($\log T \simeq 6.3$), and 335 ($\log T \simeq 6.4$) Å (Lemen et al., 2012). This active region is suitable for small-scale flare analysis because it is relatively calm and produces no eruptions greater than a GOES B-class flare. The pixel size and time resolution of each filter is 0.6" and 12 s, respectively. The SDO/AIA data are calibrated by the `aia_prep` routine in SolarSoftWare (SSW: Freeland & Handy, 1998). We obtain light curves at the loop tops for our analysis. Figure 2.1 shows the observed active region obtained from the AIA 171 Å filter. The red crosses and red line indicates the foot points of coronal loops and their vertical bisector, respectively. This red line corresponds to the observation locations. The length and location of the red line is defined to avoid the active region core and is extended to where the existence of the loop can be visually confirmed.

Figure 2.2 shows the intensity distribution along the red line in figure 2.1. We regard spikes in this profile as coronal loops. Each loop we detect is enhancements above $3\sigma_{\rm ph}$, where $\sigma_{\rm ph}$ represents photon noise. In this study, we estimate $\sigma_{\rm ph}$ as the square root of mean intensity along the red line. The red and blue crosses in figure 2.2 represents the peak and bottom of each large spikes. We estimate the minimum coronal loop radius as the minimum FWHM of these which is 5.2 pixels along the vertical bisector. Therefore, light curves are summed in each 4×4 pixels along the red line ($5.2/\sqrt{2} \simeq 4$).

Figure 2.3 presents a cropped map of figure 2.1. Each red square indicates pixels used in the light curve. The size of each square is 4×4 pixels as described above. The number of the observation locations is 40.

The latitude of this active region is approximately 15 deg north. To track the movement of this active region due to the rotation, we calculate the apparent velocity as follows:

$$v_{\rm app} = \frac{2\pi R_\odot \cos\phi}{360} v_{\rm rot} \text{ km day}^{-1} \tag{2.1}$$

where, $R_\odot$, ϕ, and $v_{\rm rot}$ represent the solar radius, latitude, and the rotation rate. According to the result of Snodgrass & Ulrich (1990), the rotation rate of this active region is estimated as

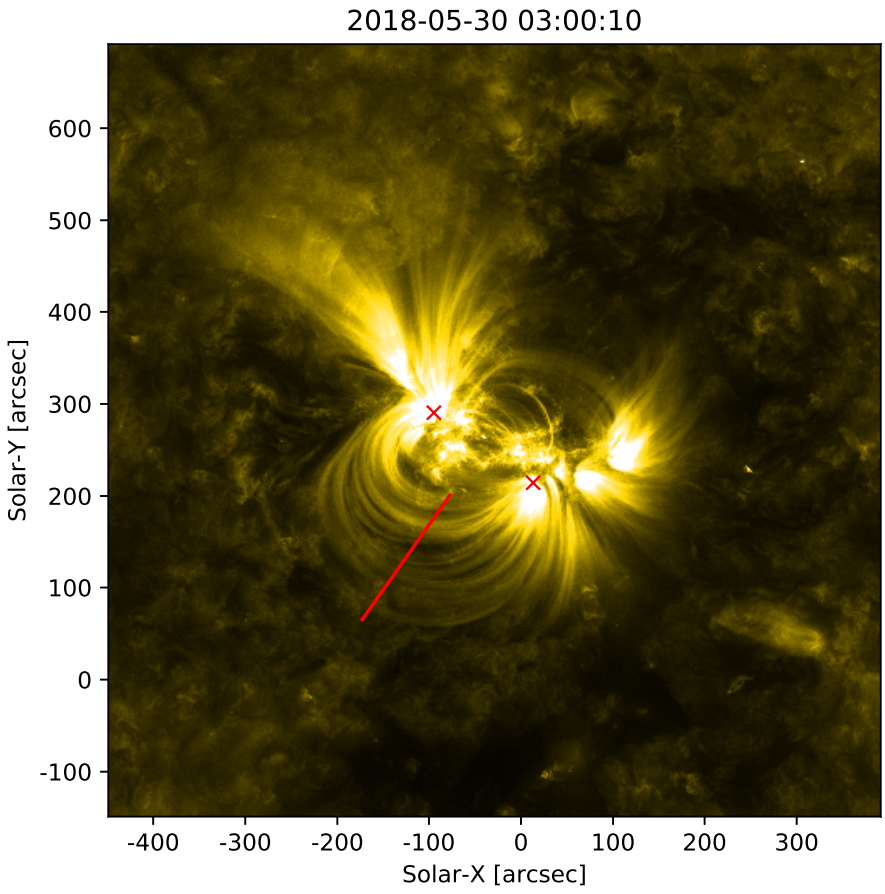

Figure 2.1: A snapshot of NOAA active region 12712 between 03:00 – 04:00 UT on 30 May 2018 obtained by the SDO/AIA 171 Å. The red crosses represent the locations of loop foot points. The red line represents the vertical bisector of both foot points.

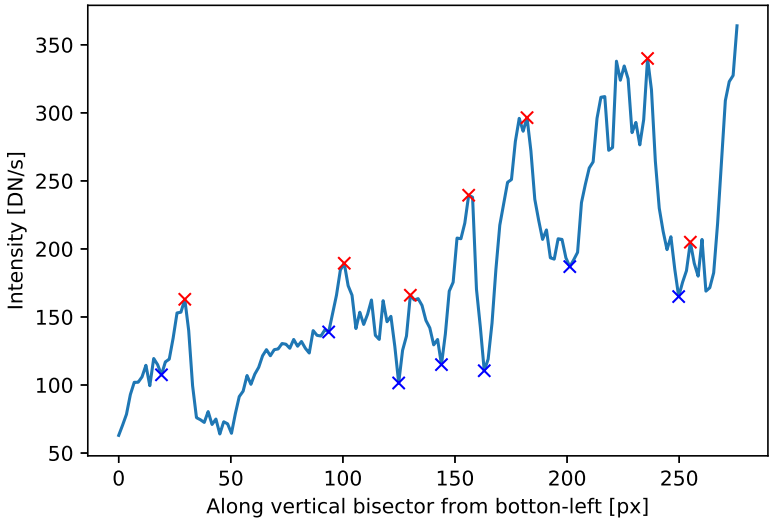

Figure 2.2: Intensity distribution along the vertical bisector of loop foot points (Red line in figure 2.1). Red and blue crosses represent peaks and bottoms of large enhancements, respectively.

approximately 14.54 deg day^{-1}. Therefore, $v_{\rm app}$ can be estimated as 1.7×10^5 km day^{-1} We assume that 1 "along the solar-X at this active region is equivalent to 730 km. This assumption is reasonable because the longitude of this active region is almost zero. We calculate the apparent velocity of this active region as 9.8 $''$ h^{-1}. The apparent motion is corrected for by moving the pixels in the light curve accordingly.

We obtain the light curves of the six filters in each red box. For example, Figure 2.4 represents the observed light curves in one red box. Some enhancements can be seen in the cooler channels (171, 193, 211 Å), while the intensities of hotter channels (335, 94, 131 Å) are very low and noisy. The loop lengths can be roughly estimated as 200 – 400 Mm.

2.3 Numerical Simulation

We calculate the evolution of a coronal loop plasma heated by flares with a one-dimensional model. In this study, we use CANS (coordinated astronomical numerical software [1]) 1D solar flare package.

[1]Details are available at the website `http://www.astro.phys.s.chiba-u.ac.jp/netlab/astro/index2-e.html`. We used the version of 21 September 2019 distributed at `http://www-space.eps.s.u-tokyo.ac.jp/~yokoyama/etc/`

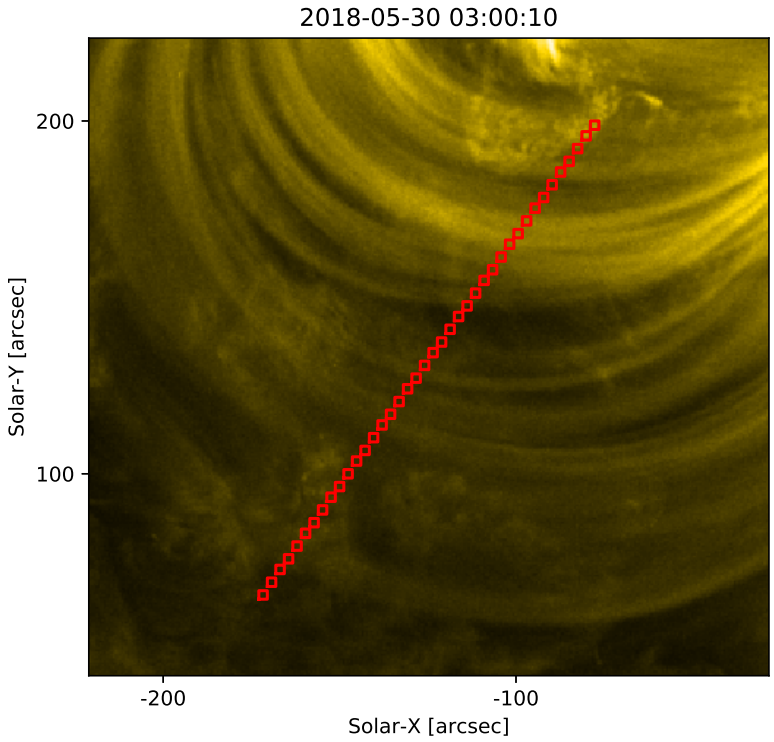

Figure 2.3: Trimmed image of figure 2.1. Forty red squares indicate the area where the light curves are obtained.

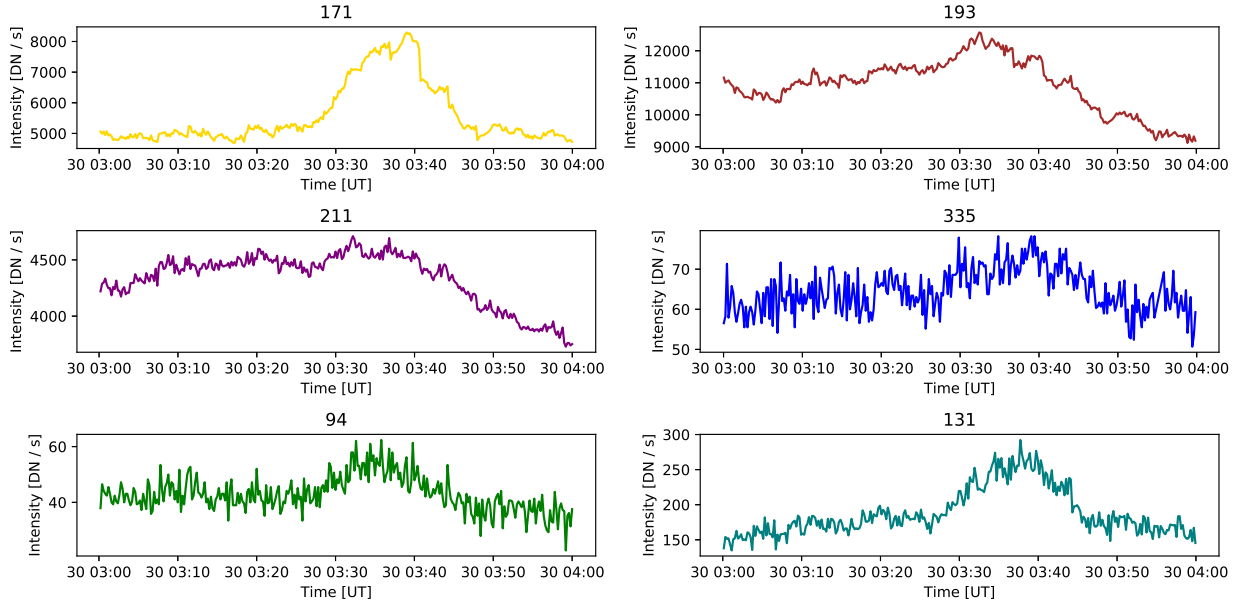

Figure 2.4: An example of light curves of one observational region (top-right red square in Figure 2.3) obtained from six filters of SDO/AIA.

The fundamental equations are as follows:

$$\frac{\partial}{\partial t}(\rho S) + \frac{\partial}{\partial x}\left(\rho V_x S\right) = 0 \tag{2.2}$$

$$\frac{\partial}{\partial t}\left(\rho V_x S\right) + \frac{\partial}{\partial x}\left[\left(\rho V_x^2 + p\right) S\right] = \rho g S \tag{2.3}$$

$$\begin{aligned} \frac{\partial}{\partial t}\left[\left(\frac{p}{\gamma - 1} + \frac{1}{2}\rho V_x^2\right) S\right] + \\ \frac{\partial}{\partial x}\left[\left(\frac{\gamma}{\gamma - 1}p + \frac{1}{2}\rho V_x^2\right) V_x S - \kappa \frac{\partial T}{\partial x} S\right] = \\ \left(\rho g V_x + H - R + H_f\right) S \end{aligned} \tag{2.4}$$

$$p = \frac{k_B}{m}\rho T \tag{2.5}$$

where, p, T, v_x, ρ, $\gamma = 5/3$, S, g, H, R, H_f, k_B, κ, and m represent the pressure, temperature, plasma velocity along the loop, density, heat capacity ratio, cross-sectional area, gravitational acceleration, static heating, radiative cooling, flare heating, Boltzmann constant, thermal conductivity, and mean particle mass, respectively. The simulation assumes that the length and cross section of the loop do not change with time; the cross section is uniform along the loop; the flow is inviscid and compressible; and the location where the flare occurs is fixed at the loop top. The Spitzer thermal conductivity (Spitzer, 1956) and gravity are taken into account as follows.

$$\kappa = \kappa_0 T^{5/2} \tag{2.6}$$

$$g = g_0 \cos\left(\frac{\pi}{2L}x\right) \tag{2.7}$$

where, $\kappa_0 = 10^{-6}$ cgs, $g_0 = 270$ m/s^2 and L represent thermal conductivity strength, a gravitational acceleration at the photosphere, and the half loop length.

An approximation to correct for the effects of high-density plasma is included in the radiative cooling model as following equations:

$$R = \rho^2 \Lambda_\rho(\rho)\Lambda(T) \tag{2.8}$$

$$\Lambda_\rho(\rho) = \frac{\rho_{\rm cl}}{\rho}\tanh\left(\frac{\rho}{\rho_{\rm cl}}\right) \tag{2.9}$$

where, $\rho_{\rm cl} = 10^{12}$ cm^{-3}. The radiative cooling function $\Lambda(T)$ is approximated by an algebraic

---

`cans/index-e.html`.

function as follow:

$$\Lambda(T) \approx \Lambda_0 10^{\Theta(T)} \tag{2.10}$$

$$\theta \equiv \log_{10}\left(\frac{T}{T_{\rm cl}}\right) \tag{2.11}$$

$$\Theta(\theta) = 0.4\theta - 3 + 3 \times \frac{2}{e^{1.5(\theta+0.08)} + e^{-2(\theta+0.08)}} \tag{2.12}$$

where, $\Lambda_0 = 8 \times 10^{-22}$ cgs and $T_{\rm cl} = 2 \times 10^5$ K.

This simulation includes not only the corona but also the transition region and chromosphere. The flare energy input is represented by the following equations:

$$H_f = H_{f0} \cdot q(t) \cdot f(x) \cdot g_1(x) \cdot g_2(x) \tag{2.13}$$

$$q(t) = \frac{1}{4}\left\{1 + \tanh\frac{t - t_{i0}}{0.1\tau_0}\right\}\left\{1 - \tanh\frac{t - t_{i1}}{0.1\tau_0}\right\} \tag{2.14}$$

$$f(x) = \frac{1}{\sqrt{2\pi}} \exp\left[-\frac{(x - x_i)^2}{2w_f^2}\right] \tag{2.15}$$

$$g_1(x) = \frac{1}{2}\left\{1 + \tanh\frac{x - 20\mathcal{H}_0}{3\mathcal{H}_0}\right\} \tag{2.16}$$

$$g_2(x) = \frac{1}{2}\left\{1 - \tanh\frac{x - (2L - 20\mathcal{H}_0)}{3\mathcal{H}_0}\right\} \tag{2.17}$$

where, $w_f = 6000$ km, $\mathcal{H}_0 = 200$ km, and $\tau_0 = 20$ s represent the width along the loop of the flare, the scale height, and sound wave traveling time at the surface ($x = 0$), respectively. t_{i0}, t_{i1}, and x_i represent the beginning and finishing time and location of heating by the ith flare, respectively. $q(t)$ is a function of time to make the heating impulsive. The role of $g_1(x)$ and $g_2(x)$ is to prevent the heat pulse from entering directly into the chromosphere. This simulation uses the modified Lax–Wendroff scheme which is second-order accurate in both space and time. The boundary conditions at $x = 0$ and $x = 2L$ are as follows:

$$\frac{\partial \rho}{\partial x} = 0 \tag{2.18}$$

$$\frac{\partial p}{\partial x} = 0 \tag{2.19}$$

$$V_x = 0 \tag{2.20}$$

This simulation setup is mostly the same as that of Hori et al. (1997), Imada & Zweibel (2012),

Parameter	Minimum	Maximum
Heating rate [erg/s/cm^3]	10^{-2}	10^2
Flare duration [s]	1	300
Flare occurrence time [s]	$t = 0$	$t = 5600$
Flare location	$x = 0$	$x = 2L$
Loop length [Mm]	100	500

Table 2.1: Free parameters in the simulation and their ranges

Kawai et al. (2020).

To demonstrate the simulation, we show a simple example in figure 2.5. Each panel presents the temporal variation and spatial distribution of temperature, density, pressure, and plasma velocity along the loop, respectively. As each horizontal axis indicates coordinates along the loop, the left-hand edge ($x = 0$) is the surface and the right-hand edge is the loop top. The region where the temperature and pressure change rapidly ($x \simeq 0.3$ Mm) is the transition region, and the chromosphere is in the left of this region. Line color indicates the progress of time in the simulation, from blue to red. This result is for a single flare occurrence at the loop top at the beginning of the simulation. When a flare occurs, the temperature of the loop top is increased and is transported to the foot points of the loop by thermal conduction. Then, the temperature and pressure of the chromosphere are rapidly increased by the incoming high-temperature plasma. As a result, high-density plasma in the chromosphere is ejected into the corona by the pressure gradient force; this is referred to as chromospheric evaporation. Consequently, the coronal loop is filled with high-density plasma, and emits soft X-ray and EUV irradiance.

To use various results in GA later, we carry out the simulation with random flare heating rates, heating duration, occurrence time, occurrence location, number, and loop length. Table 2.1 represents the parameters and their possible ranges. According to the study of Testa et al. (2014), an energy flux of a nanoflare ($10^{24} \lesssim E \lesssim 10^{25}$ erg) is approximately 7×10^7 – 2×10^9 erg/s/cm^2. Therefore, the range of flare heating rate in the simulation is roughly $10^{-0.9}$ – $10^{0.5}$ erg/s/cm^3 because the width along the loop of flare is 6000 km. However, to include weaker and stronger heating, we defined the range of heating rate as 10^{-2} – 10^2 erg/s/cm^3. The heating duration of a nanoflare in Testa et al. (2014) is from 10 to 30 s. We define the range of heating duration in our simulation from 1 (10 times shorter than the minimum) to 300 (10 times longer than the maximum) s. Testa et al. (2014) also suggested that the duration of heating event is similar to that of transition region brightenings. The heating duration range in our simulation almost covers the

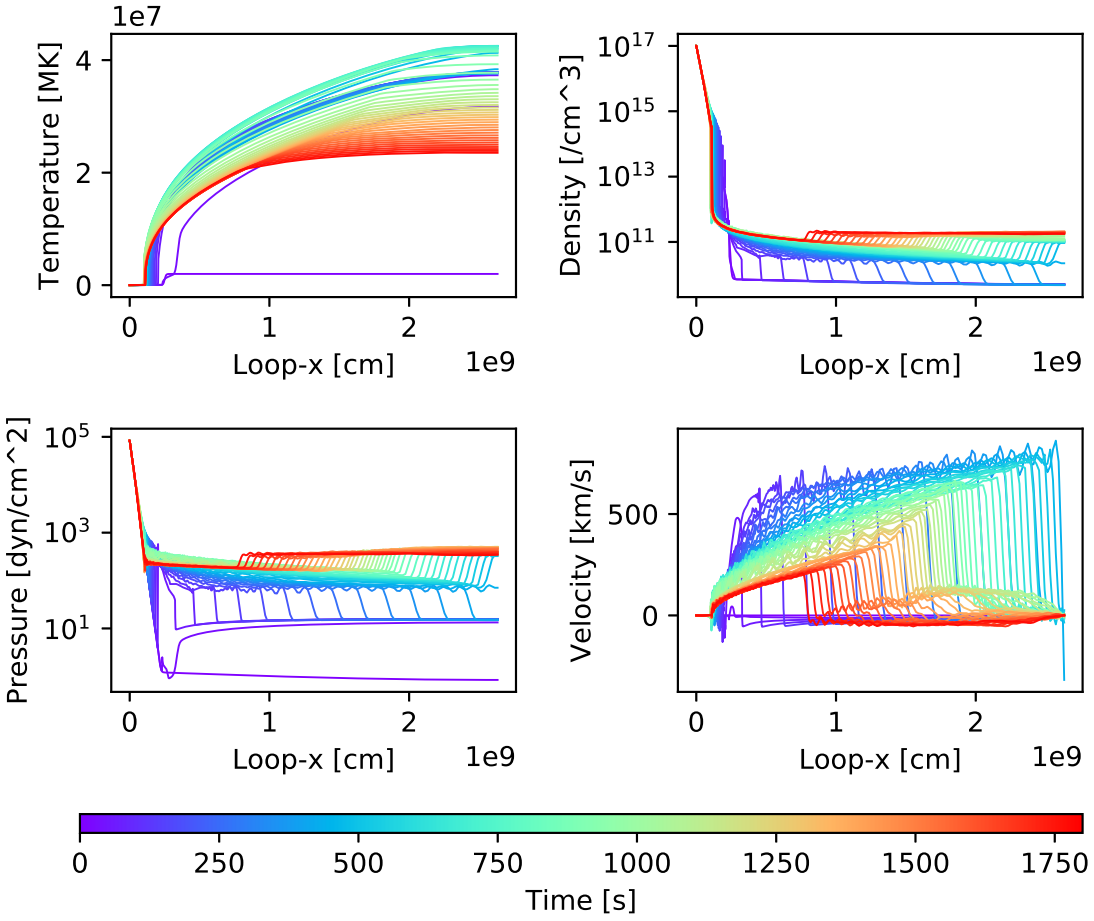

Figure 2.5: Results of the hydrodynamic simulation. Each panel presents the time evolution of the temperature distribution (left-top), density (right-top), pressure (left-bottom), and plasma velocity along the loop (right-bottom) with 30-s cadence. Each horizontal axis represents the loop coordinates from the surface to the loop top. Line color indicates the progress of time (from blue to red).

typical lifetimes of compact transition region brightenings, that is from a few tens of seconds to several minutes (Tiwari et al., 2019). The probability distributions of heating rate and flare duration are uniform in a logarithmic scale while those of flare occurrence time, location, and loop length are uniform in their ranges. This maximum number of flares is roughly determined to distinguish each heating event in each run even when flares have the longest duration. The wider the parameter range, the more various the simulation results, but the more calculations are required to reproduce the observed light curves well. These parameter ranges are wider than those of Tajfirouze et al. (2016) and enough to reproduce the observations because we focus on relatively calm coronal loops. The cadence of the simulation output is 2 s.

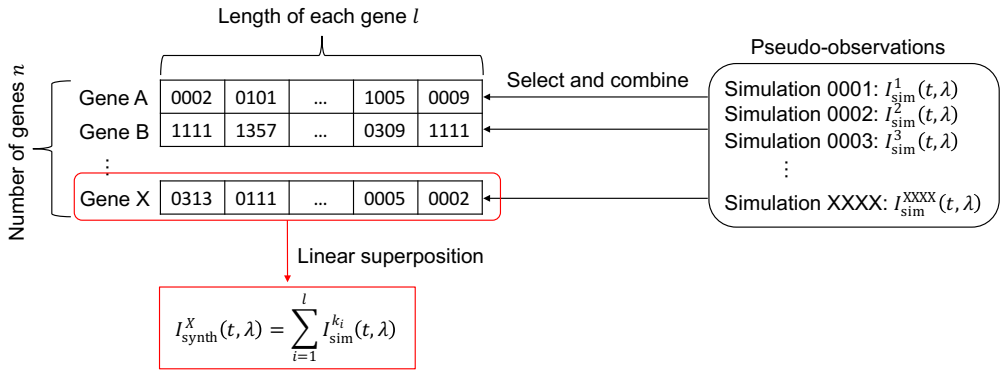

Figure 2.6: A schematic architecture of a gene used in this paper. Each gene represents a synthetic light curve $I_{\rm synth}(t,\lambda)$, which is described as a linear superposition of l of simulated light curves.

The original CANS solar flare package calculates only half of the loop (foot point to top) under the symmetry assumption as shown in figure 2.5. his assumption should work well when a flare occurs at the top like in figure 2.5. However, according to the Parker's model, nanoflares can occur everywhere along the loop and this symmetric assumption might be violated. Therefore, in this study, we extend it to calculate the whole loop (one foot point to another foot point) to consider various heating locations. Moreover, to simplify the discussion, we remove static heating ($H = 0$) and assume the loop is heated by only flares. There are two reasons for this assumption. One is that the mechanism and intensity of background heating is also unclear, therefore, another assumption is needed anyway. The second reason is that the contribution of background heating must be relatively small even when the loop is heated by small-scale flares.

In some conditions, the calculation is broken due to an overheating or overcooling of the loop. We do not use simulation results, which has density of over 10^{12} cm^{-3} around the loop top. This high density loop is sometimes caused by overcooling due to the imbalance between the flare heating

and radiative and conductive cooling. This imbalance mostly occurs when the flare heating is too large.

Because the observation duration is one hour, as described in Section 2.2, the simulation also needs to be calculated for one hour. However, to make various initial conditions, we calculate time in advance of observation duration. As can be seen in the simulation results, the variety of light curve becomes the maximum around $t = 2000$ s even for the longest loops. Therefore, we calculate for 5600 s and remove the first 2000 s for the optimization. As describe above, the number of flares are 15 in each run, however, some or all of them can occur during the first 2000 s. Therefore, the range of number of flares is from 0 to 15 during the latter one hour calculation. In this study, we ran approximately 5,000 random simulations.

As described in section 2.2, we obtain a light curve of the SDO/AIA 4×4 pixels ($\simeq 1.8\times1.8$ Mm^2) at the loop top by the observation. Therefore, we derive the SDO/AIA light curve in the 1.8 Mm range at the loop top of each calculation as well. Using the temperature response function of each SDO/AIA channel (Lemen et al., 2012), we obtain the intensities in each time and grid from the simulation result. The response functions are available from the SolarSoftWare (SSW: Freeland & Handy, 1998) procedure `aia_get_response.pro`. We assume the emission measure to be ρ^2 and derive the light curve per cross-sectional area (DN s^{-1} cm^{-2}) for each calculation. We assign the identification to each run to use them for optimization, which is described in the next section.

2.4 Genetic Algorithm

We estimate the best combinations of the results of simulations that reproduce actually observed coronal loop light curves by using GA. GA is a machine learning technique that is effective at solving optimization and searching problems and is based on the concept of Darwin's theory of evolution. "Genes" and an "environment" are necessary for GA. GA can search the gene that is optimized best for the environment through natural selection, crossover, and mutation. In this study, each gene is a list of the simulation IDs that are assigned in section 2.3. Each gene expresses the synthetic light curve by linear superposition of its simulation results. Therefore, a synthetic light curve $I^X_{\rm synth}$ of a gene X can be described as follows:

$$I^X_{\rm synth}(t,\lambda) = \sum_i^l I^{k_i}_{\rm sim}(t,\lambda) \tag{2.21}$$

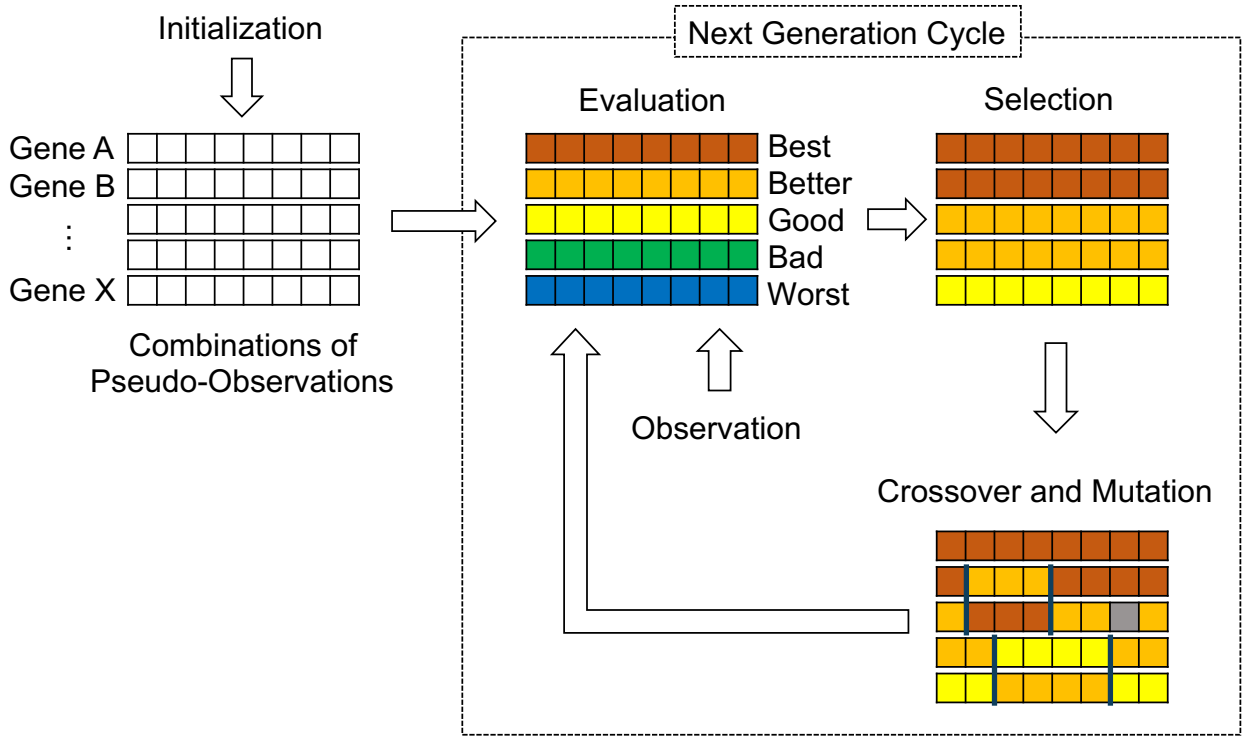

Figure 2.7: A schematic flow of GA. Firstly, initial genes generated randomly are evaluated based on the correlations between observed $I_{\rm obs}(t, \lambda)$ and synthetic $I_{\rm synth}(t, \lambda)$ light curves. Second, based on the evaluation, better genes are left or duplicated probabilistically, while worse genes are eliminated. Third, the remaining genes swap their information partially with each other. Sometimes a mutation occurs to avoid a local minimum. The best gene that reproduces the observed light curves can be estimated by continuing this iteration.

where, l and $I^k_{\rm sim}$ represent the length of gene (the number of simulated loops to combine) and simulated light curve of simulation ID k, Figure 2.6 represents the schematic organization of the genes. In this paper, gene length l and the number of gene n are 100 and 500, respectively. l is defined based on the analysis of Tajfirouze et al. (2016), which suggests that the number of loops in each SDO/AIA pixel is approximately 1000. However, only one flare occurs on each coronal loop in their study while at most 15 flares occur on each loop in our simulation. Therefore, we roughly estimate the number of elemental loops in each red square in figure 2.3 as 100. The accuracy of reproduction of light curves increases as the number of genes n increases. We define $n = 500$ based on available computational resources. However, even if n is smaller, the reproducibility can be improved by increasing the number of iteration.

The main components of GA are a natural selection, crossover, and mutation. Figure 2.7 schematically shows the procedures. Genes have a random list of IDs at the beginning. First, in natural selection, while better genes are left or multiplied, worse genes are eliminated stochastically. Each gene is evaluated by the averaged correlation between observed and synthetic light curves in six AIA filters. Therefore, the selection probability of gene i can be described as follows:

$$p_i = \frac{c_i}{\sum_{k=1}^{n} c_k} \tag{2.22}$$

where, c_i represents the averaged correlation of gene i. Genes in the next generation are decided by this probability. However, in this case, even the best gene among the generation has a possibility to be eliminated. Therefore, we leave at least one of the genes which have the highest correlation to the next generation, which is typical for GA. This can accelerate the learning while it may increase the likelihood of getting a local solution due to the lack of variety of genes.

Second, in crossover, we search for new better solutions by swapping information partially between the pair of the genes. In this study, we choose two-point crossover for this procedure. We randomly choose pairs of genes and two crossover points (black vertical lines in figure 2.7) from within the genes. The IDs between the crossover points are exchanged with each other. These new genes are populations for the next generation. 90 % of all genes are crossed over in each generation.

Third, some genes are mutated to maintain diversity and avoid local minima. In a mutation, a few IDs in the genes are randomly replaced to the another ID with a low probability. In this paper, 1 % of all IDs in the genes are mutated in each generation.

We estimate the gene that can best reproduce the observed light curves by iterating these procedures 1,000 times for each observational area. The gene is a list of simulation results and we know the inputs of flare parameters of each simulation. Therefore, we can estimate the combination of flare parameters that reproduce observational results best by GA.

When synthetic light curves $I_{\rm synth}$ are satisfactorily correlated to observational results $I_{\rm obs}$, the relationship between them can be written as follows:

$$I_{\rm obs}(t, \lambda) \simeq A(\lambda) \times I_{\rm synth}(t, \lambda) + B(\lambda) \tag{2.23}$$

where, A and B are coefficients derived by least squares. A and B indicate the ratio of amplitudes of fluctuations between $I_{\rm obs}$ and $I_{\rm synth}$ and the background component of $I_{\rm obs}$, respectively. As mentioned above, $I_{\rm sim}$ is the time series of emissions from the coronal loop whose cross-sectional area is 1 cm^2. Therefore, the cross-sectional area of elemental coronal loops in each observation

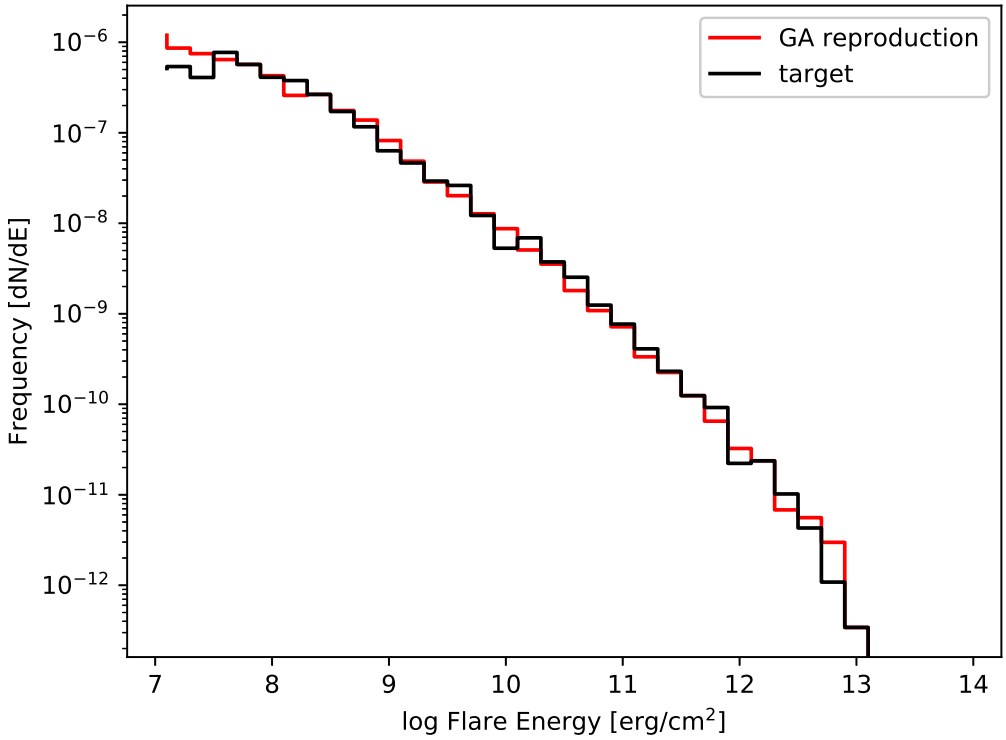

Figure 2.8: An example of frequency distribution of flares as a function of energy. Black and red lines indicate the distribution of input of the target simulations and of estimation by the GA, respectively.

region can be estimated as $\Delta S_{\rm loop}(\lambda) = A(\lambda)$ [cm^2].

2.5 Result

At first, to verify the robustness of our procedure, we test whether the GA can estimate the correct combination of simulations from light curves generated by random set of genes. We create SDO/AIA synthetic light curves from 100 sets of simulation results as a target. The created light curves have a random gaussian noise whose standard deviation is 10% of the intensity. The estimated genes are not exactly the same with the target gene, however, the derived distribution of flares are very

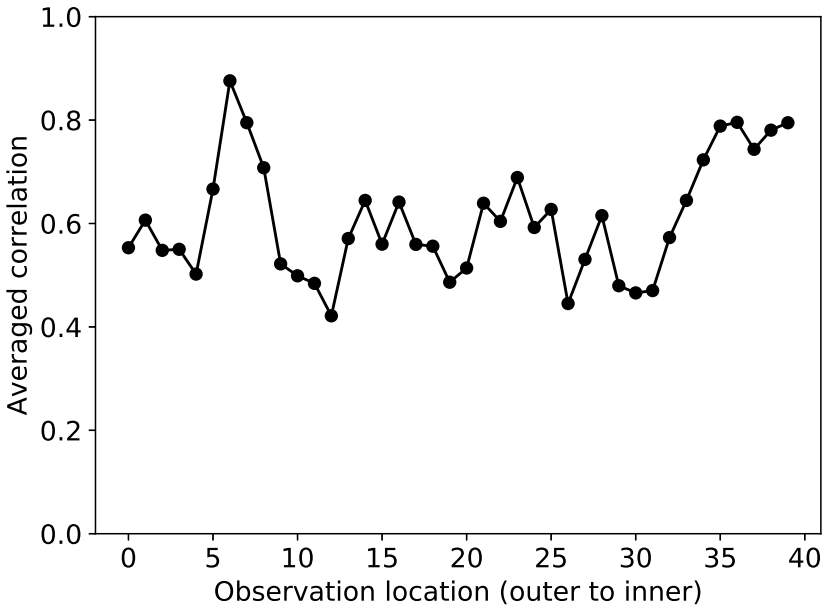

Figure 2.9: Averaged correlations between observed and the best synthetic light curves in each observation region. The horizontal axis indicates the observation location (from outside to inside).

similar to the input of that. Figure 2.8 represents an example of occurrence frequency distribution of flares in unit of cross sectional area. Red and black histograms represent distributions of GA reproduction and input of target simulations. In this case, the mean correlation between target and reproduced light curves is approximately 0.97. We continue this test 25 times to define the uncertainty of this method. We define the uncertainty of the occurrence frequency distribution, σ_f, as a standard deviation of the difference between target and reproduced one in each energy bin.

Figure 2.9 represents the average correlations between observed and optimized synthetic light curves. The horizontal axis indicates observation locations (red squares in figure 2.1), from outside to inside. The correlations are approximately 0.4 – 0.9, though they depend on the regions.

Figure 2.10 shows an example of observed light curves obtained from SDO/AIA six channels (solid lines) and synthetic ones estimated by GA, which reproduces the observation best (dashed lines). These light curves are obtained from the region where the average correlation is the best ($\simeq$ 0.9). Large fluctuations are reproduced accurately, however, smaller fluctuations other than photon noise are not reproduced well.

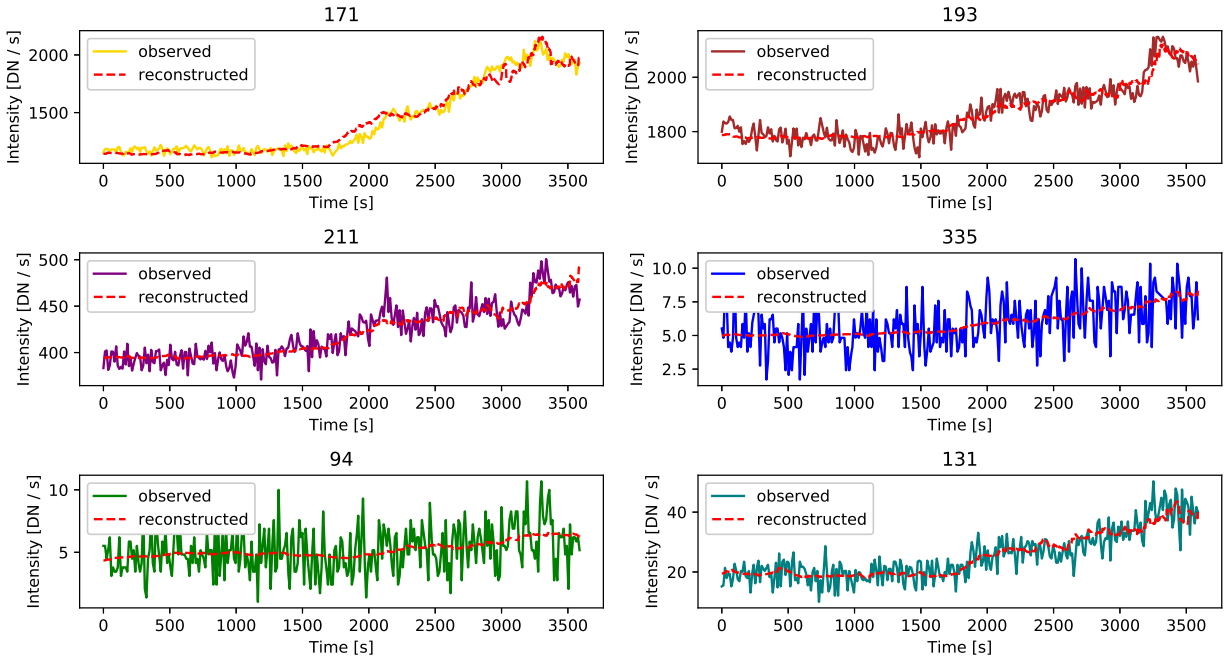

Figure 2.10: Sample of observed SDO/AIA light curves (solid lines) and synthetic ones which are optimized to reproduce the observation the most by GA (red dashed lines), which has the best average correlation ($\simeq 0.9$).

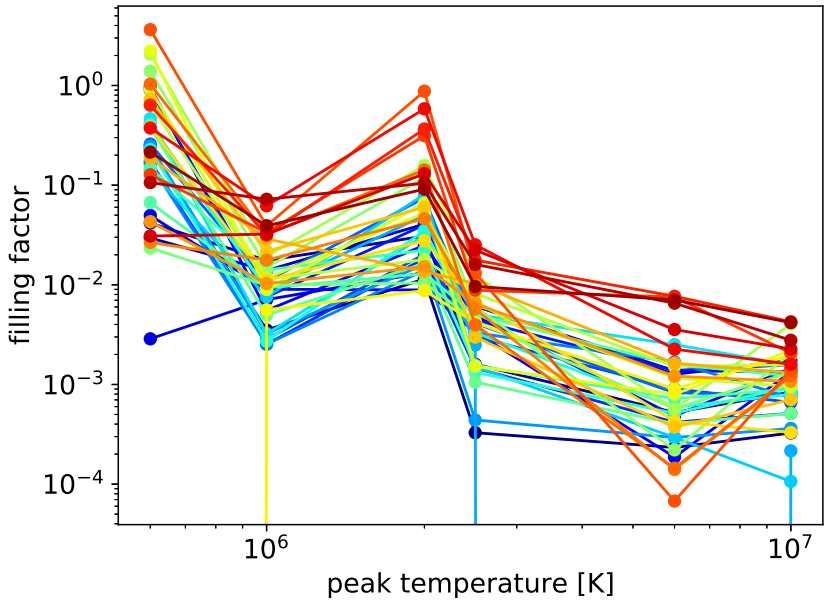

Figure 2.11: Filling factors of heated coronal loop in each observation location and filter. Horizontal axis represents the peak temperature of response function of each SDO/AIA channel. Colder (Warmer) color indicates farther distance from (closer to) the core.

We define a cross sectional area along the loop of each observation region (red square in figure 2.1) as $S_{\rm obs} = w^2$, where w represents the width of each red square. In this study, the size of each red square is 4×4 pixels, and hence, $w \simeq 1.75$ Mm and $S_{\rm obs} \simeq 3.1$ Mm^2. We define the filling factor of the coronal loop ϕ as follows:

$$\phi(\lambda) = \frac{l \times \Delta S_{\rm loop}(\lambda)}{S_{\rm obs}} \tag{2.24}$$

where, l represents the length of each gene. Figure 2.11 presents the estimated filling factors of all observation areas for each AIA filter. The warmer color indicates observation locations which are closer to the core. The horizontal axis represents the peak temperature of the response function of each AIA channel. As a result, the higher the plasma temperature, the lower the filling factor. In addition, the location closer to the core tends to have larger filling factor.

The energy flux by flares can be described as:

$$F(t) = \frac{1}{l} \sum_{i}^{l} H_f^{k_i}(t) \ [\mathrm{erg/s/cm^2}] \tag{2.25}$$

where H_f^k is the flux caused by flares in simulation ID k. Each panel of figure 2.12 represents the estimated time series of energy flux by flares in each observation area. The color indicates the observation location as same as figure 2.11. The panel without lines shows that the GA determines that the calculations without flares from $t = 2000$ to $t = 5600$ are the best to reproduce the observed light curves. Almost all observed regions are heated by flares intermittently, which have energy flux above the typical requirement (10^7 erg/s/cm^2: Withbroe & Noyes, 1977).

Figure 2.13 presents the frequency distribution of detected flares as a function of energy. Vertical lines indicate uncertainties defined by the test described in the beginning of this section as follow:

$$\sigma'_f = N_{\rm obs} \times \Delta S_{\rm loop}(94) \times \sigma_f. \tag{2.26}$$

where, $N_{\rm obs}$ represents the number of observation regions (40 in this study). The volume of the heated loop is necessary for the energy estimation; however, it depends on the filter. Therefore, in this study, we estimate the energy with $\Delta S_{\rm loop}(94)$, which is the most similar to the X-ray observational study of Shimizu (1995). The number of all detected flares is approximately $37,000$. Generally, the occurrence frequency distribution of flares as a function of energy show the power-law. However, the result does not have a single power-law index through the energy range. Therefore, we calculate the power-law index of the distribution in each energy bin as shown in Figure 2.14. The size of each bin is defined as the width by which the flare energy on a logarithmic scale changes

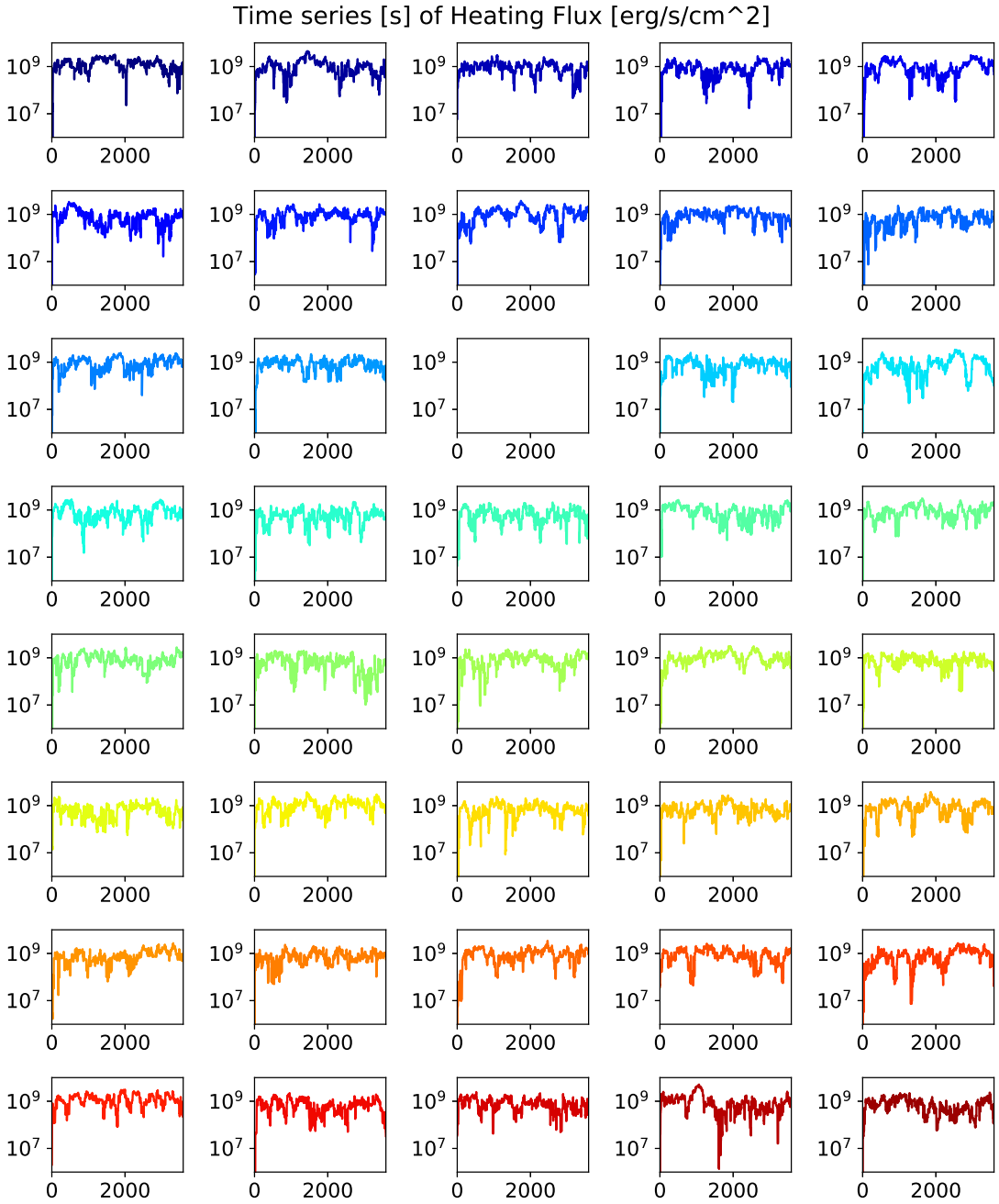

Figure 2.12: Time series of energy flux of flares in each observation region derived by GA. Colder (Warmer) color indicates farther distance from (closer to) the core. The panel without lines indicates that the GA determines that the calculations without flares from $t = 2000$ to $t = 5600$ reproduce the observed light curves best.

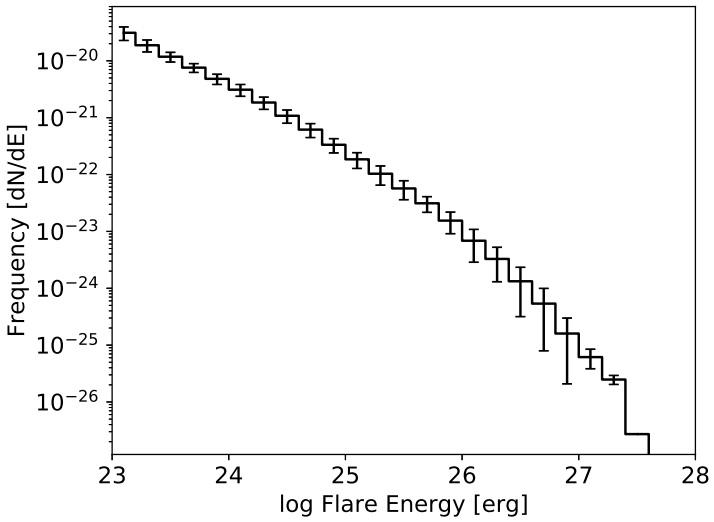

Figure 2.13: Frequency distribution of flares as a function of energy estimated by GA. vertical lines indicate errors which defined by the test described in the beginning of Section 2.5. The number of all detected flares is 37,458.

by one. Horizontal axis indicates median of flare energy of each bin. In most cases, the power-law index increases with flare energy. The power-law index is greater than 2 in the energy range from 10^{26} to 10^{27} erg and above. On the other hand, the index is approximately 1 in the energy range smaller than $10^{25.5}$ erg. This energy range is probably lower than the detection limit of our method because the index of simulation input is also approximately 1.

The blue line (left axis) in figure 2.15 represents the contribution of flares to heat the corona in each energy range. The red line (right axis) represents the cumulative contribution from high energy. Vertical lines indicate the errors calculated from σ_f defined in the beginning of this section. Flares that contribute the most to the heating of the corona are those in the energy range of $10^{26} \lesssim E \lesssim 10^{27}$ erg. Moreover, the 90% of the coronal heating is done by flares that have energies greater than 10^{25} erg.

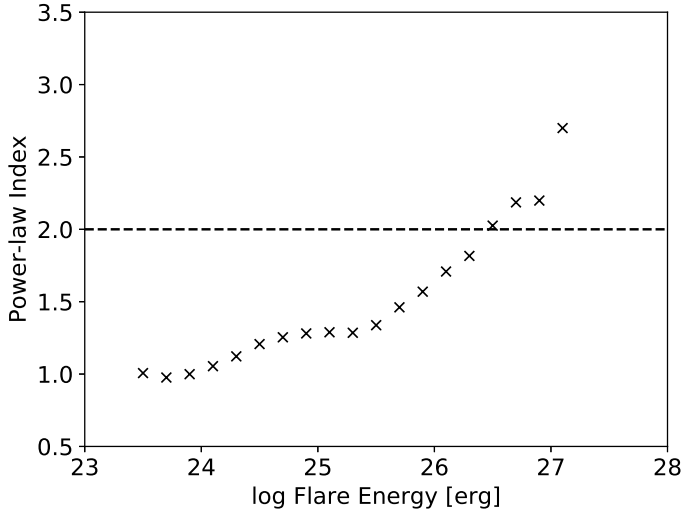

Figure 2.14: Series of power-law indices of the occurrence frequency distribution shown in Figure 2.13 in each energy bin. The size of each bin is the width that the flare energy on a logarithmic scale changes one. Dashed horizontal line indicates where power-law index becomes 2 which implies whether smaller flares are dominant in the coronal heating or not.

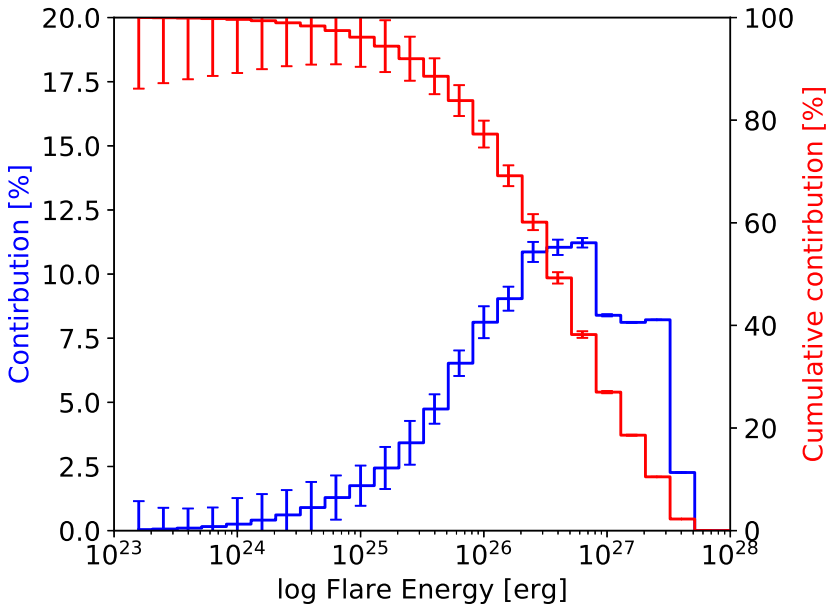

Figure 2.15: Contribution of flares to the coronal heating in each energy range (left axis, blue) and the cumulative contribution from high energy (right axis, red). Vertical lines indicate the errors calculated from the definition of the standard deviation σ_f described in the beginning of Section 2.5.

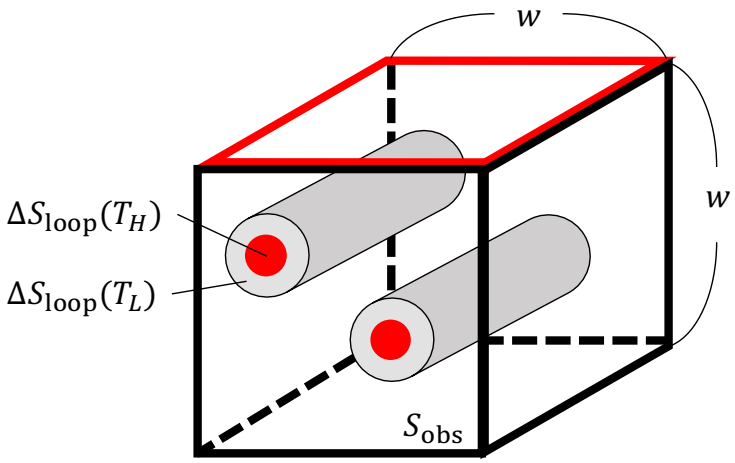

Figure 2.16: Schematic picture of coronal loops in the observation region. $\Delta S_{\rm loop}(T_H)$ and $\Delta S_{\rm loop}(T_L)$ represents the cross sectional areas of loops composed of hotter and cooler plasmas, respectively. Red square represents the observation region depicted in Figure 2.1.

2.6 Discussion

In this paper, we introduced a new method for detection and energy estimation of small-scale flares by using one-dimensional simulation and GA, which is a machine learning technique. We applied our method to the active-region coronal loop observation by SDO/AIA and obtained the time series of energy flux of flares, occurrence frequency distribution as a function of energy, and filling factors.

The occurrence frequency distribution generally can be fitted by the power-law distribution, however, the power-law index of the derived distribution depends on the fitting range. As a result, the power-law index is found to be greater than 2 in flare energy range of $10^{26} < E < 10^{28}$ erg (Figure 2.14). In this energy range, smaller flares are dominant in heating the corona, which is in line with the nanoflare heating model. On the other hand, the power-law index is approximately 1 in the energy range of smaller than $10^{25.5}$ erg. This is probably caused by the detection limitation of our method because the distribution is similar to that of simulation inputs. Moreover, we found that the coronal loops are heated by flares that have enough energy flux to heat the corona intermittently (Figure 2.12). This is mainly because we calculate the fine structure of the loop that cannot be resolved. From figure 2.11, we found that the volume that is heated by flares is much smaller than the observational resolution though it depends on the temperature and region. On the other hand, we found that the flares in energy range of $10^{26} \lesssim E \lesssim 10^{27}$ erg contribute to the coronal heating the most. In addition, 90% of the energy flux comes from flares that release energies greater than

10^{25} erg. It has been thought that smaller flares (10^{23} – 10^{24} erg) contribute the most to heat the corona because the energy flux of detected flares are not enough. There are some reasons why our result is incompatible with previous studies. We calculate the plasma evolution of coronal loops taking into account smaller loops than the observational resolution unlike previous studies. It is possible that the flare energy and occurrence frequency could be derived more accurately than previous studies by considering such a process. This is because our energy estimation is based on physics unlike the method that defines a flare energy as a difference of thermal energy of a loop (*e.g.,* Shimizu, 1995). However, our method has some shortcomings. First, our results do not explain the balance of energy on the whole active region because we focus only on the coronal loop and not on the core region. Second, as we mentioned above, our method might be unable to detect small-scale flares which have an energy less than approximately 10^{24} erg. Third, our combined synthetic light curves reproduce large fluctuations in the observation while smaller fluctuations are not reproduced well.

We found that the filling factor increases as we get closer to the core, and the variation between the minimum and maximum is approximately three orders of magnitude. This is probably because the loops closer to the core can experience more magnetic pressure from the outer loops. This tendency is acceptable because the loops closer to the core are brighter than those in the outer region. As shown in figure 2.11, the higher the peak temperature of each SDO/AIA filter, the lower the filling factor of coronal loops. This tendency is in agreement with the study of Sakamoto et al. (2009), which compared the filling factors of the soft X-ray and EUV loops. This temperature dependence implies that the hotter coronal loops have a sparser structure than the cooler ones. Figure 2.16 presents the schematic picture of coronal loops in each observation region. $\Delta S_{\rm loop}(T_H)$ (red circle) and $\Delta S_{\rm loop}(T_L)$ (gray circle) represents the cross-sectional areas of each loop composed of hotter and cooler plasmas, respectively. The red square corresponds to that depicted in Figure 2.1.

The largest filling factor is greater than 100%. This can be caused by the assumption that the observational region is regarded as a cube. Coronal loops might be distributed along the line-of-sight direction deeper than observational width w. On the other hand, in some cases, the filling factor is very small, approximately 0.01%. Assuming l of the elemental loops exist in each observation region, the half radius of each elemental loop d can be described as:

$$d = \sqrt{\frac{S_{\rm obs}\phi}{\pi l}}. \tag{2.27}$$

Therefore, in case of $0.01\% < \phi < 100\%$,

$$10 \lesssim d \lesssim 990 \text{ [km]}. \tag{2.28}$$

This result roughly corresponds to the maximum half radius of the elemental loop estimated by sounding rocket experiment, which is approximately 15 km (Peter et al., 2013). 10 km is roughly equivalent to 0.014 $''$ at the solar surface, which is about 2.3 % of the resolution of SDO/AIA.

To make large amounts of simulation results for GA, we use the one-dimensional coronal loop model which has a low computational cost. As mentioned in section 2.1, the evolution of the coronal loop can be described in 1D when ignoring some processes. Strictly speaking, flares are magnetic reconnections between the loops that cannot be described using the one-dimensional model. Instead of this process, we directly substitute the flare heating term into the energy equation. However, making thousands of simulation results by using multidimensional model is unrealistic for current computational performance.

We use CANS solar flare package to calculate a coronal loop heated by small-scale flares. Therefore we neglect some important processes in small-scale flare analysis such as non-equilibrium of ionization (NEI), radiative transfer, and nonthermal electron beams. Imada et al. (2015, 2011b), Reale & Orlando (2008) suggest that NEI should have effects on the emission from the plasma which is impulsively heated by flares. Using the HYDRAD model (*e.g.,* Bradshaw & Cargill, 2010), Bradshaw & Klimchuk (2011) studies a NEI effect on the coronal loop emissions for the case that a loop is heated by nanoflares. Because our simulation neglects NEI unlike HYDRAD, energy of small-scale flares may be estimated smaller than the actual and some small-scale events cannot be distinguished. Including this process to the simulation should make the analysis more accurate. Polito et al. (2018b) suggest that the Si IV Doppler velocity at the chromosphere is a good indicator for detection of nanoflares ($\simeq 10^{24}$ erg) from the analysis based on the RADYN model (*e.g.,* Allred et al., 2015). It is necessary to validate the result by analyzing both coronal loops and chromospheres. Testa et al. (2014) also use the RADYN model and reveal that an observation of small and rapid variability of intensity and velocity at the loop foot point is consistent with heating by nonthermal electron beams generated by nanoflares. These processes should also be included in our analysis, however.

We must derive the combination of simulations which reproduce the observations the most. Therefore, we use GA, which is used to solve optimization and searching problems such as the traveling salesman problem. GA is suitable for statistical analysis, however, it has initial value dependence and may find only a local minimum. Moreover, it is difficult to prove that the combined synthetic light curve has only one combination because all combinations ($_{5000}\mathrm{C}_{100} > 10^{200}$) must be calculated to prove that. In addition, GA has some free parameters such as length of each gene and the number of genes and iterations. The larger number of genes and iterations can make the correlation better, and thus, they should be as large as possible. On the other hand, the length

of each gene defines the number of elemental loops in each observation region. In this paper, we assume that the number of loops in each macro pixel is 100 and try to estimate the best combination of simulations under this condition. However, the number of elemental loops in each identifiable loop is high and under discussion (*e.g.,* Polito et al., 2018b, Tajfirouze et al., 2016). Therefore, it is necessary to analyze flares in various cases of the length of each gene.

Chapter 3

The Energy Conversion Rate of an Active Region Transient Brightening Estimated by Hinode Spectroscopic Observations

3.1 introduction

Parker (1988) proposed that nanoflares are magnetic reconnections between the coronal magnetic fields tangled by the foot point motions due to the convection, as described in Parker (1983). To validate the nanoflare heating model, it is essential to reveal the occurrence frequency distribution of the flares as a function of energy. The frequency distributions of smaller flares have been estimated using various methods and instruments for a few decades. In some studies, power-law index α was found to be greater than the threshold 2 (*e.g.,* Benz & Krucker, 2002, Parnell & Jupp, 2000), which suggests that the frequency distribution at smaller energies can be broken to heat the corona sufficiently, whereas other studies found that α is smaller (e.g., Aschwanden et al., 2000, Jess et al., 2019, Shimizu, 1995, Tajfirouze et al., 2016). This uncertainty might be caused by the failure to detect the smallest events or energy estimation due to instrumental limitations or wrong methods. One of the problems in these studies is that their analysis is based on EUV and X-ray thermal energies but not on kinetic or nonthermal energies. We derived the contribution of small-scale flares using one-dimensional loop simulation and a genetic algorithm in Chapter 2. One of the strengths

of their study is that the method can consider the distribution of released energy to thermal and nonthermal energy using simulations.

Spectroscopic observations have successfully achieved significant progress in coronal plasma physics for example, flares (Imada et al., 2013, 2014, Polito et al., 2018a), jets (Kawai et al., 2019, Matsui et al., 2012, Young & Muglach, 2014), dimmings (Imada et al., 2011a), and coronal loops (Schmelz et al., 2001, Warren et al., 2008). One of the strengths of spectral observations is the ability to derive a line-of-site plasma velocity for each ion species. Testa et al. (2014) reported the rapid variation of intensity and velocity by the *Interface Region Imaging Spectrograph* (IRIS: De Pontieu et al., 2014) launched in 2013. IRIS provides imaging and spectral observations of the chromosphere and transition region at high spatial, temporal, and wavelength resolutions. According to the comparison with a simulation, this event is caused by a nonthermal electron beam accelerated by a nanoflare that has an energy of 10^{25} erg. Using one-dimensional coronal loop simulation, Polito et al. (2018b) suggested that up to 20 km s^{-1} of the Doppler blueshift can be seen in the *IRIS* Si IV line when nonthermal electron beams are produced even by 10^{24} erg events. Brooks & Warren (2016) reported that the mean value of nonthermal velocity in the non-flaring active region is approximately 18 km/s from observations of the *EUV Imaging Spectrometer* (EIS: Culhane et al., 2007) on board Hinode (Kosugi et al., 2007). This nonthermal velocity is much smaller than that expected from high-temperature reconnection jets in the nanoflare heating model.

In this study, we estimate Doppler motion and nonthermal energies of nanoflares and the changes in the amount of thermal energy during them to compare the energy balance between them. Section 3.2 shows observational data of an active region obtained from *Hinode*/EIS and the *Atmospheric Imaging Assembly* (AIA: Lemen et al., 2012) on board the *Solar Dynamics Observatory* (SDO: Pesnell et al., 2012). Sections 3.3 and 3.4 present the method of detecting events and calculating their Doppler motion and nonthermal and thermal energies. Section 3.5 provides our results, and we discuss the energy balance between them and the contributions to active region heating in Section 3.6. The implications of our results for the future satellite mission are discussed in Section 3.7.

3.2 Data and Observations

In this study, we estimate Doppler motion and nonthermal energies of nanoflares and the changes in the amount of thermal energy during them to compare the energy balance between them.

In this study, we used two series of EUV images of the NOAA active region 11890 observed from 18:07 UT on November 09, 2013, to 14:20 UT on the next day. The first series includes

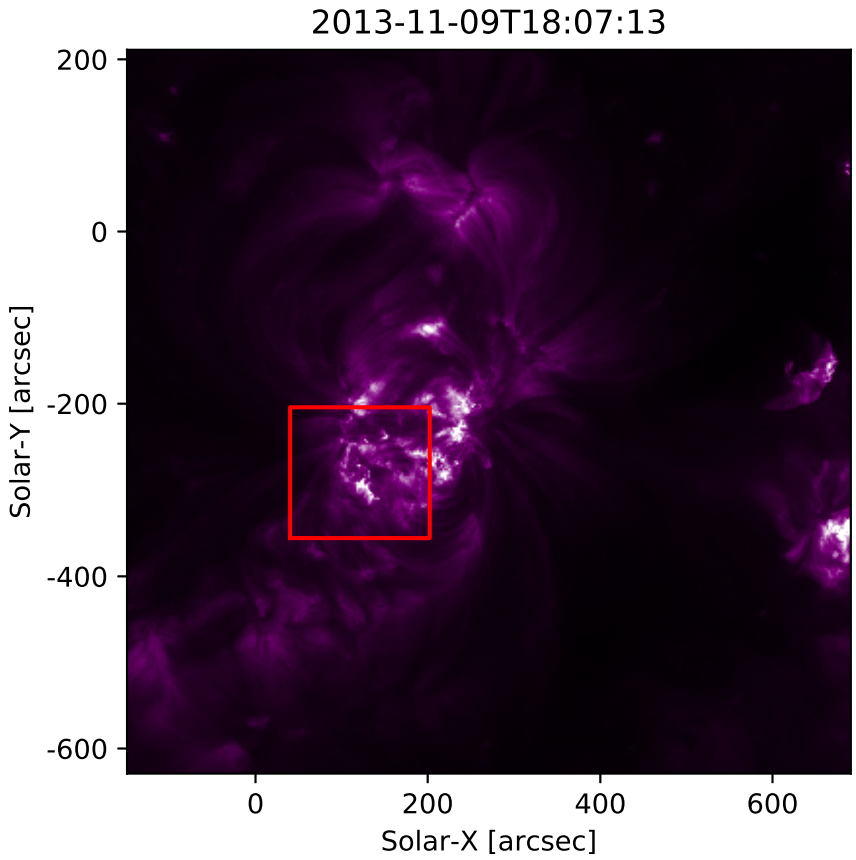

Figure 3.1: An example of maps of active region 11890 obtained from SDO/AIA 211 Å. The coordinates of this active region are approximately (Solar-X, Solar-Y) = (100″, −200″). The red square indicates the field of view of the EIS at that time.

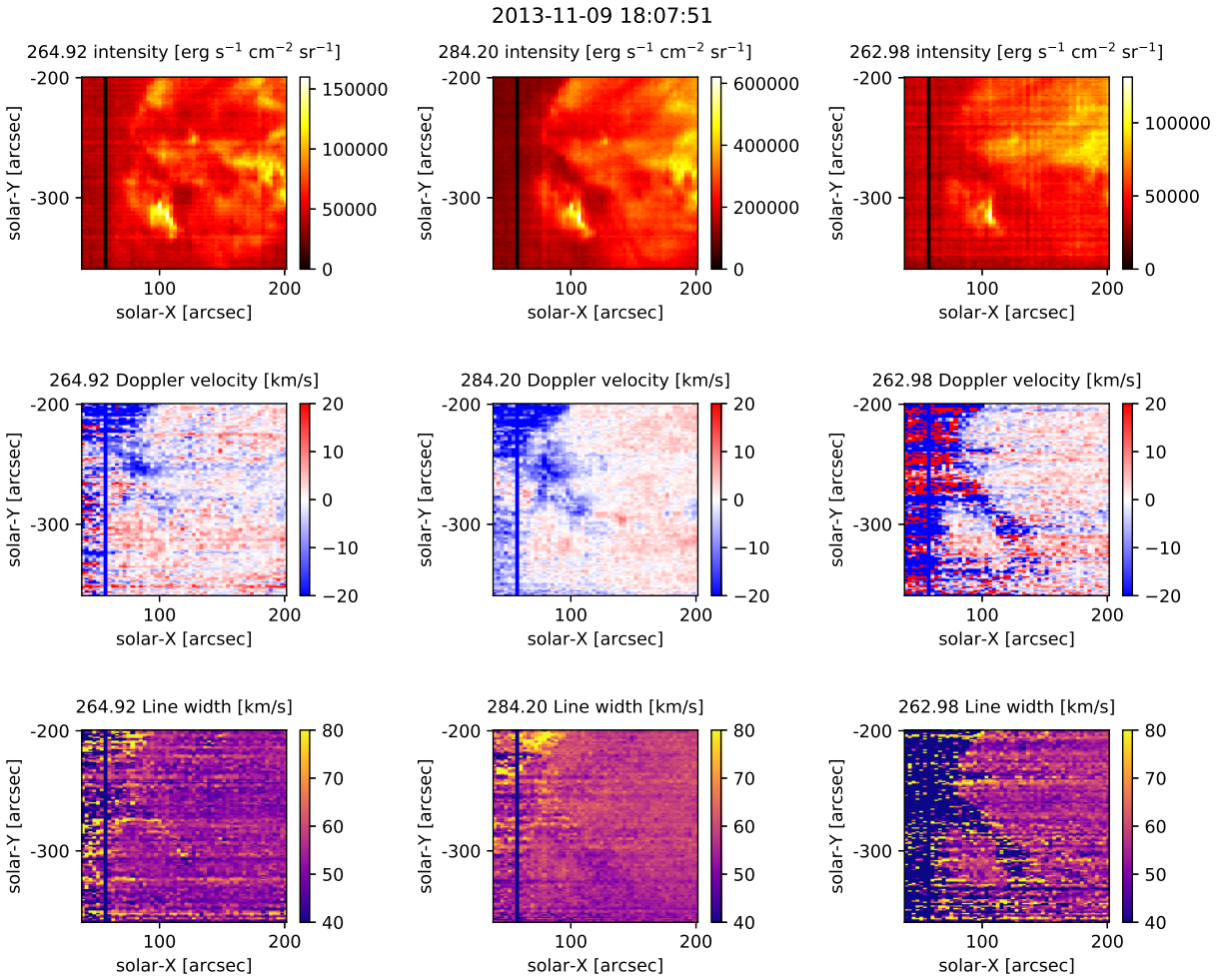

Figure 3.2: An example of maps of active region 11890 obtained from Hinode/EIS Fe XIV (*left*), Fe XV (*center*), and Fe XVI (*right*). *top*, *middle*, and *bottom* panels present maps of the intensity, Doppler velocity, and line width, respectively.

Ion species	Wavelength [$\AA$]	log (Formation T [K])
Fe X	184.54	6.1
Fe VIII	185.25	5.7
Fe XII	186.88	6.2
Fe XXIV	192.03	7.2
Ca XVII	192.83	6.8
Fe XII	195.12	6.2
Fe XVII	255.05	6.8
Fe XVI	262.98	6.8
Fe XXIII	263.69	7.2
Fe XIV	264.92	6.3
Fe XIV	274.37	6.3
Fe XV	284.20	6.4

Table 3.1: Line list of Hinode/EIS study ID 485

spectroscopic images obtained from Hinode/EIS, and the other includes the EUV images observed by the SDO/AIA. Figure 3.1 presents a snapshot of the active region at the beginning of the observation duration. The red square indicates the field of view of the EIS at that time. The coordinates of this active region are approximately (Solar-X, Solar-Y) = ($100''$, $-200''$) at the beginning of the observation. This active region causes GOES X1.1 flare, which begins at 05:08 UT on November 10 and continues for 10 min according to the Hinode Flare Catalog (Watanabe et al., 2012). This large brightening makes it difficult to detect small-scale events; however, as described below, we did not use the data around this time. There are no more flares that are greater than the GOES C-class.

We used the data series of the Hinode EIS Study ID 485, which was designed for flare observations. This study included 12 wavelength windows, as described in Table 3.1. The formation temperatures were obtained from the line list of the atomic database CHIANTI version 9.0.1 (Dere et al., 2019). We selected the Fe XIV, Fe XV, and Fe XVI lines for our analysis because they have suitable formation temperatures for small-scale heating events and have less noise. Figure 3.2 presents the first snapshot of the observations obtained by the Fe XIV (*left*), Fe XV (*center*), and Fe XVI (*right*). The *top*, *middle*, and *bottom* panels show maps of the intensity, Doppler velocity, and line width, respectively. The method for calculating the Doppler velocity and line width is described in the next section. In cases data are lacking, as shown by the vertical line around the solar-X $\simeq 50\ ''$ in

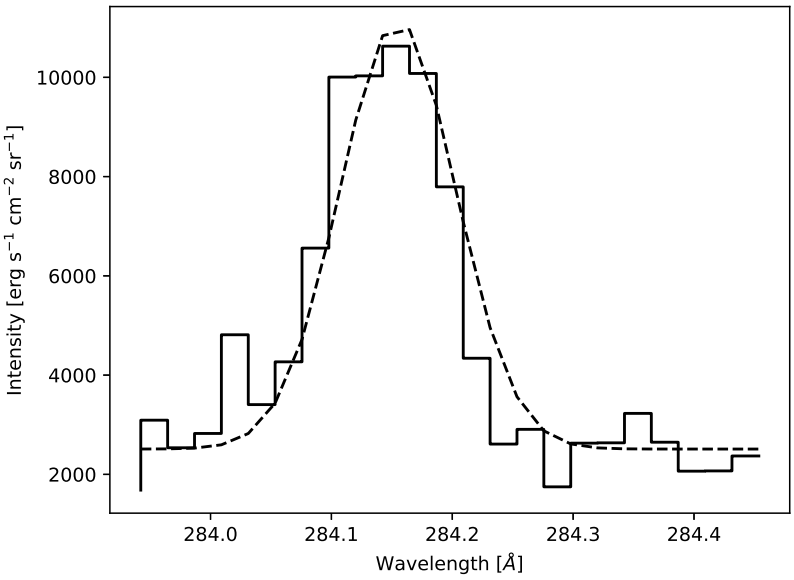

Figure 3.3: An example of the observed spectra obtained from the EIS Fe XV window. The dashed line indicates the Gaussian fitted curve.

Figure 3.2 and Fe XVI, because the data are relatively noisy. The field of view (FOV) of this study was 162 ″ for solar-X and 152 ″ for solar Y. The number of pointing positions, slit width, scan step size, exposure time, and exposure delay were 54, 2 ", 3 ", 3 s, and 0 s, respectively. The resolution along the solar-Y is 1 ". Time to complete each raster scan for making an image is approximately 254 s. Level 0 data can be retrieved from [1]Hinode/EIS website. EIS data from the raster were processed using procedures provided in SolarSoftWare (SSW: Freeland & Handy, 1998) to correct for flat fields, dark current, cosmic rays, hot pixels, and slit tilts. Owing to the temperature variation of the telescope, there was an orbital change in the line center, which caused an artificial Doppler shift of at most ±20 km s^{-1}. This error was corrected using the housekeeping data by Kamio et al. (2010). Except for suspensions over 300 s, the observation duration was 30,831 s in total. We used 130 datasets for analysis in this study.

Owing to the large amount of spectral data, each observed spectrum was automatically fitted

[1]`http://solarb.mssl.ucl.ac.uk/SolarB/index.jsp`

by a single Gaussian function, as follows:

$$f(\lambda) = A_0 \exp\left[-\frac{1}{2}\left(\frac{\lambda - A_1}{A_2}\right)^2\right] + A_3 \tag{3.1}$$

where Gaussian coefficients from A_0 to A_3 represent the height, center, standard deviation, and constant bias of the Gaussian, respectively. After fitting, the mean Doppler velocity and nonthermal velocity of the plasma can be retrieved from the spectrum. First, we defined the line-of-site velocity in each pixel $v'_{\rm Dop}$ as follows:

$$v'_{\rm Dop} = \frac{A_1 - \lambda_0}{\lambda_0} c \tag{3.2}$$

where λ and c are the target wavelength and speed, respectively. Then, we defined the Doppler velocity by calibrating $v'_{\rm Dop}$ using their median in each image as

$$v_{\rm Dop} = v'_{\rm Dop} - {\rm Median}\left(v'_{\rm Dop}\right). \tag{3.3}$$

The line width of each spectrum, which indicates the nonthermal velocity, can be derived as follows:

$$\delta\lambda = \frac{1}{\sqrt{4\ln 2}} \frac{c}{\lambda_0} A_2. \tag{3.4}$$

However, this line width is generally estimated to be larger than the nonthermal velocity of the plasma because w includes line broadening due to instrumental width. Therefore, we estimated the nonthermal velocity $v_{\rm nth}$ according to Brooks & Warren (2016).

$$v_{\rm nth} = \sqrt{\delta\lambda^2 - \left(\frac{2k_B T_i}{m_i} + \sigma_I^2\right)} \tag{3.5}$$

where λ_0, k_B, T_i, m_i, and σ_I represent the line centroid, Boltzmann's constant, ion temperature, mass, and instrumental width, respectively. The line centroid, λ_0, and ion temperature, T_i, are defined based on the values on the line list of the CHIANTI database. The instrumental width was measured in the laboratory before the launch of the Hinode by Korendyke et al. (2006). Young (2011) derived the Y-axis variation of the instrumental width from off-limb quiet sun observations. The slit width, which includes their correlation, is provided in SSW as a routine called `eis_slit_width`. We used values in this routine for σ_I similar to Brooks & Warren (2016). The mean ion mass value we used was 9.27×10^{-23} g, according to the mass of the iron ion.

An example of the observed spectra (solid) and Gaussian fitted curve (dashed line) is shown in

Figure 3.3. This spectrum is obtained from the EIS Fe XV window. In this case, the Doppler and nonthermal velocities are -26 km s^{-1} and 42 km s^{-1}, respectively.

The time resolution of EIS raster images was slightly long to analyze small-scale brightenings that have time scales of tens of seconds or several minutes. Therefore, we used images obtained from the SDO/AIA observations, which have a higher time resolution. The SDO/AIA instrument takes full-sun images of nine UV and EUV broadband channels. Among these channels, we chose 211 Å , which is responsive to the emission of $10^{6.3}$ K plasma (Boerner et al., 2012). The pixel size and time resolution of each filter were $0.6''$ and 12 s, respectively. AIA images were calibrated by the `aia_prep` routine in SSW to eliminate instrumental effects.

3.3 Event Detection

Figure 3.4 presents a schematic diagram of the flow of the detection of the EIS Doppler/nonthermal velocity enhancements. We assumed that small-scale flares are enhancements of either Doppler or nonthermal velocities defined by the following equation:

$$\delta v > 3 \times \sigma \tag{3.6}$$

where δv and σ represent changes in the absolute value of the Doppler/nonthermal velocity and the standard deviation for 10 min before the beginning of the enhancement, respectively. Sometimes, Doppler and nonthermal velocities are not derived accurately because of the lack of intensity, especially in Fe XIV and XVI. Therefore, we neglected the pixels that had an intensity less than 5×10^4 erg s^{-1} cm^{-2} sr^{-1} as noise. We decided this threshold based on the median of a Fe XVI intensity map shown in Figure 3.2 ($\simeq 4.9 \times 10^4$ erg s^{-1} cm^{-2} sr^{-1}) because the Doppler velocity and line width in about half the area of the map are unstable. After the detection of enhancements, we obtained the solar-X and -Y coordinates and the scan time of each enhancement. When peaks of multiple enhancements appear at adjacent pixels simultaneously, they are regarded as a single event. In this case, the event coordinate and energy are defined as the geometric center of gravity and their sum in each pixel, respectively. We derived the occurrence time of each enhancement using solar-X and the scan step time because small events are thought to be sensitive to time resolution. The EIS raster scan begins from the west side and requires approximately 4.6 s for each scan step (pointing position). This detection was performed for Fe XIV (264.92 Å), XV (284.20 Å), XVI (262.98 Å) images.

We obtained SDO/AIA light curves around energy enhancements detected by EIS observations.

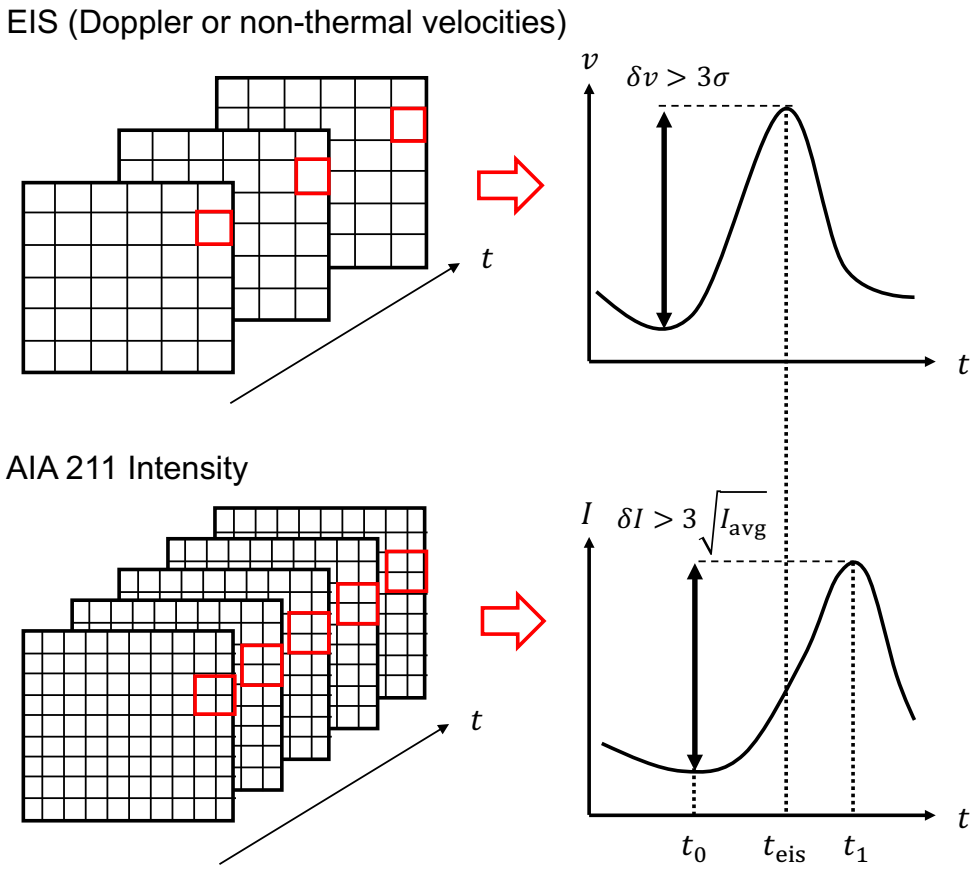

Figure 3.4: Flow of the detection of EIS Doppler/nonthermal velocity enhancements. First, we detect a Doppler/nonthermal velocity enhancement that exceeds the threshold. Second, an intensity enhancement of the AIA 211 Å light curve around the velocity enhancement is detected if it exists. Finally, only velocity enhancements with peaks ($t_{\rm eis}$) between t_0 and t_1 are selected as valid events for later analysis.

However, it is necessary to align both the coordinates of the Hinode/EIS and SDO/AIA data. We applied a template matching method between a pair of EIS and AIA images. First, an EIS raster image was converted to have the same spatial resolution as the AIA using bilinear interpolation. Second, we rigidly slide the converted EIS intensity image as a template over the AIA image and calculate the square root of difference in intensities between them at each location. Finally, we derive the spatial offset from where the difference becomes the minimum. We used the EIS Fe XIV (264.92 Å) and the AIA 211 Åimage observed at 18:12:04 UT and 18:11:59 on November 09 for the matching. The intensities in both snapshots are normalized to 0 – 1 range because the response is different from each other. Then, we applied the spatial offset found as described above to all other EIS images.

After the EIS-AIA calibration, we obtained an AIA light curve around the EIS velocity enhancement for 150 s before and after the occurrence. We used this time range because small-scale heating events such as microflares and nanoflares are thought to have time scales of tens of seconds or several minutes. The AIA lightcurve is obtained by integrating over 16×16 pixels centered on the calibrated location of the EIS enhancement. This area is somewhat large when compared to the smallest event; however, we used this value by considering the inaccuracy of the estimated EIS-AIA spatial offset. In fact, as we will show later (Figure 3.5), the locations of EIS and AIA enhancements are sometimes misaligned. Moreover, this area might be smaller than the largest AIA enhancement. However, even if the entire AIA brightening does not fit the lightcurve area, it does not affect our quantitative analysis; while we need the AIA lightcurve for the event selection, the Doppler velocities, nonthermal, and thermal energies all needed to derive the energy conversion rate use solely the EIS data (see next section). We detected enhancements in the AIA 211 Å light curve accompanying EIS energy enhancement. An AIA enhancement begins when the time difference of intensity exceeds the threshold $3\sqrt{I_{\rm avg}}$, where $I_{\rm avg}$ represents the square root of the average intensity 1 min before the beginning of the EIS enhancement. Sometimes, multiple AIA enhancements existed for single EIS enhancements; therefore, we chose the AIA enhancement that begins at the time closest to the EIS event. When there were no AIA enhancements that satisfy the condition above, EIS enhancement was not employed for the analysis below.

We selected EIS velocity enhancements that occur with AIA enhancement to compare the energy balance between them. We derived the relative time of the EIS energy enhancement to an AIA light curve enhancement $t_{\rm rel}$ using the following equation:

$$t_{\rm rel} = \frac{t_{\rm eis} - t_0}{t_1 - t_0} \tag{3.7}$$

where $t_{\rm eis}$, t_0, and t_1 represent the time when the EIS velocity enhancement is detected, and the

beginning and peak of the AIA enhancement.

Figure 3.5 presents an example of temporal series of the Fe XV Doppler velocity, line width, and intensity and AIA 211 Å maps. The first and second rows show the Doppler velocity and line width maps around the detected enhancement and the temporal series at the center (black ticks) of the maps. The third and fourth rows represent the time series of the intensity maps and light curves around the velocity enhancement obtained from the EIS and AIA, respectively. Comparing the panels in the second column, the location of an event seems slightly misaligned between the EIS and AIA (the AIA enhancement has a larger solar-Y). This gap is caused by the inaccuracy of our alignment; however, this misalignment is compensated for by obtaining the AIA light curve over a somewhat large area (16×16) to avoid missing events.

3.4 Energy Estimation

To determine the Doppler motion, nonthermal, and thermal energies, we estimated the electron density using the `eis_density` function in SSW. This function returns the electron number density as a response to the input of a pair of spectra in the Fe XIV windows. Sometimes, the density derived by this method does not have a valid number owing to photon noise or lack of data. Pixels with these errors are neglected in later analysis.

The Doppler motion energy in each EIS pixel is defined as follows:

$$E_{\mathrm{Dop}} = \frac{1}{2} m n_e v_{\mathrm{Dop}}^2 S_{\mathrm{eis}}^{\frac{3}{2}} \tag{3.8}$$

where m represents the mean particle mass, and its value is 2.08×10^{-24} g in this study. n_e and S_{eis} represent the electron number density estimated by the `eis_density` function and 1 pixel area of the EIS image, respectively. Similarly, nonthermal energy is defined as

$$E_{\mathrm{nth}} = \frac{1}{2} m n_e v_{\mathrm{nth}}^2 S_{\mathrm{eis}}^{\frac{3}{2}}. \tag{3.9}$$

When multiple enhancements are detected in adjacent pixels at the same time, the summed energy is multiplied by $\sqrt{N}$, the number of pixels, to correct the volume.

We compared the Doppler motion and nonthermal energies at the peak of each enhancement and the difference in thermal energy between the peak and the background. We define the indicator

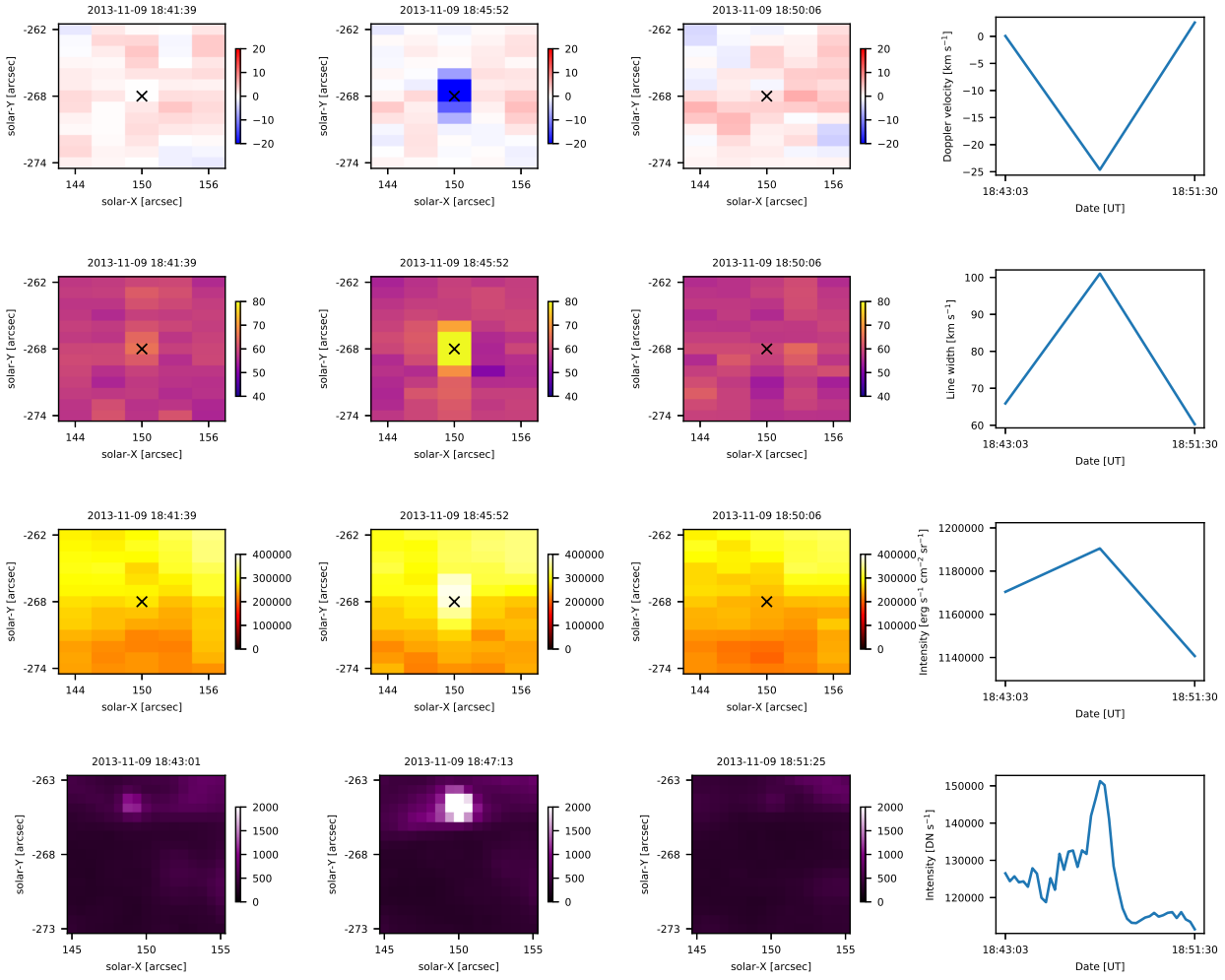

Figure 3.5: An example of time series of the Fe XV Doppler velocity (first row), line width (second row), EIS intensity (third row), and AIA 211 Å intensity (fourth row) around a detected enhancement. The first and third columns represent the maps before and after enhancement. The maps in the second column are those at the peak of the Doppler velocity enhancement. The right column shows a temporal series of the velocities at the center (black ticks) of the map and the light curves around the enhancement obtained by EIS and AIA.

of the energy balance $\phi_{\rm Dop}$ and $\phi_{\rm nth}$ using the following equation:

$$\phi_{\rm Dop} = \frac{\Delta E_{\rm th}}{E_{\rm Dop}} \tag{3.10}$$

$$\phi_{\rm nth} = \frac{\Delta E_{\rm th}}{E_{\rm nth}} \tag{3.11}$$

where $\Delta E_{\rm th}$, $E_{\rm Dop}$, and $E_{\rm Dop}$ represent the changes in thermal energy, Doppler motion, and non-thermal energies, respectively. This difference of thermal energy is estimated as follows:

$$\Delta E_{\rm th} = 3k_B n_{e1} T_1 S_{\rm eis}^{\frac{3}{2}} - 3k_B n_{e0} T_0 S_{\rm eis}^{\frac{3}{2}} \tag{3.12}$$

where subscripts 0 and 1 indicate the background and peak, respectively. We assume that the background temperature T_0 and density n_{e0} are medians of those estimated by the entire EIS observations. We did not use pre-event temperature and density for background values because the time scale of transient brightenings or nanoflares (from tens of seconds to several minutes) is shorter than that of EIS observations ($\geq$ 254 s).

3.5 Result

Based on the criteria in Section 3.3, the numbers (occurrence frequencies [$\rm s^{-1}cm^{-2}$]) of the detected Doppler velocity enhancements with AIA enhancements are 6077 (1.5×10^{-21}) for Fe XIV, 10727 (2.7×10^{-21}) for Fe XV, and 4183 (1.0×10^{-21}) for Fe XVI. Those of the nonthermal velocity are 583 (1.4×10^{-22}) , 889 (2.2×10^{-22}), and 1 (2.5×10^{-25}) for Fe XIV, Fe XV, and Fe XVI, respectively.

The first and third rows in Figure 3.6 present the entire distributions of the relative occurrence time of EIS energy enhancements to AIA enhancements, $t_{\rm rel}$, detected using Doppler and nonthermal velocities, respectively. The second and fourth rows represent the detailed distributions of $t_{\rm rel}$ between -0.5 – 1.5. The solid lines indicate $t_{\rm rel} = 0$ and $t_{\rm rel} = 1$, which indicate the beginning and peak of the AIA enhancement, respectively. The dashed line in each panel in Figure 3.6 indicates the median of $t_{\rm rel}$ for each wavelength. We find that around 40% of the velocity enhancements occur between $t_{\rm rel} = 0$ and $t_{\rm rel} = 1$. The median $t_{\rm rel}$ is 0.4 – 0.5 for each channel except for the Doppler velocity enhancements detected by Fe XVI. According to some loop heating simulations (*e.g.,* Botha et al., 2011, Bowness et al., 2013), the released energy is converted into kinetic energy just after the beginning of an enhancement, prior to $t_{\rm rel} \approx 0.5$ after which it is transformed into thermal energy. Accordingly, $t_{\rm rel}$ should distribute just after the beginning (for example, $t_{\rm rel} \simeq 0.1$).

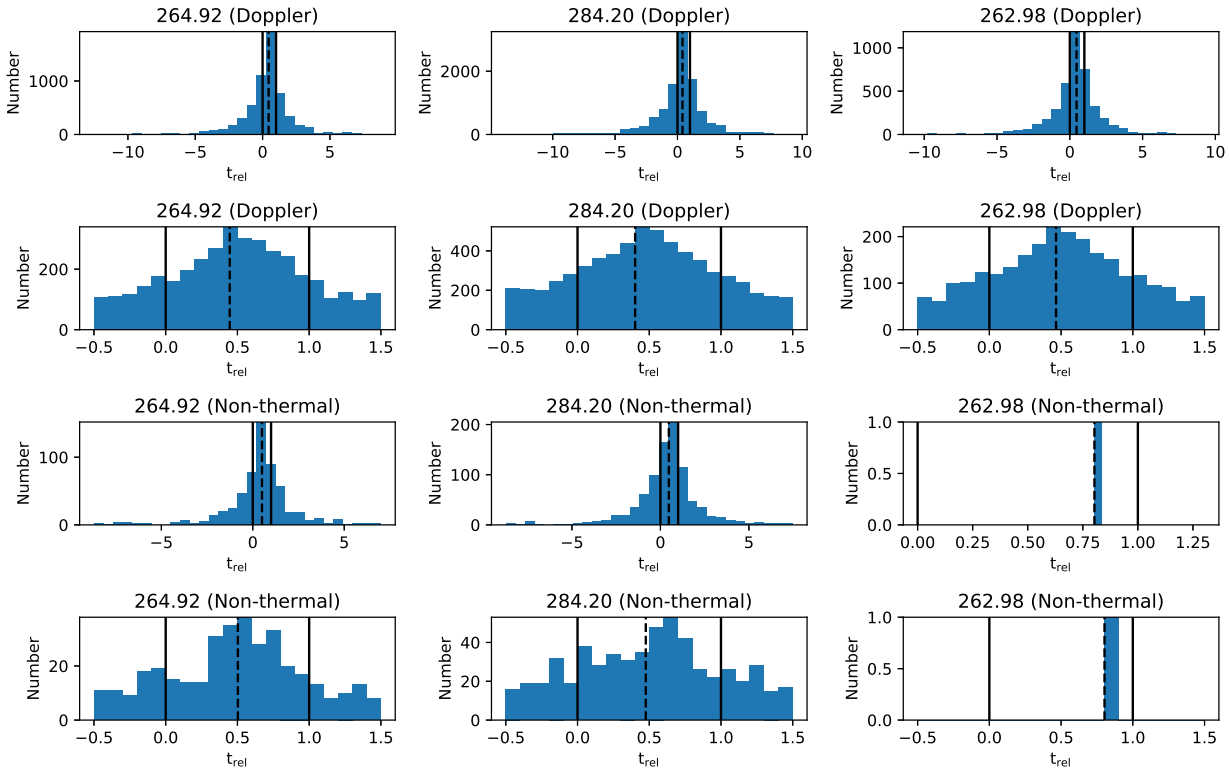

Figure 3.6: The first and third rows represent the entire t_{rel} distributions of energy enhancements. The second and fourth rows show the detailed distributions of the first and third rows in the range of $-0.5 \leq t_{\mathrm{rel}} \leq 1.5$. The solid lines indicate $t_{\mathrm{rel}} = 0$ and $t_{\mathrm{rel}} = 1$. The dashed line in each panel indicates the median of t_{rel}.

The distribution of $t_{\rm rel}$ shown here does not directly support this process.

Figure 3.7 presents the occurrence frequency distributions as a function of energy derived by Fe XIV (left), Fe XV (center), and Fe XVI (right). The top and bottom panels represent the distributions detected using Doppler and nonthermal velocities, respectively. The black, red, and blue lines represent the distributions of Doppler motion, nonthermal energy, and thermal energy, respectively. The dotted lines indicate power-law fitted lines in the energy range of $10^{21} \leq E \leq 10^{23}$ [erg] (Doppler), $10^{23} \leq E \leq 10^{25}$ [erg] (nonthermal), and $10^{24} \leq E \leq 10^{26}$ [erg] (thermal). The numbers in the legend represent the power-law indices. We chose the above energy ranges to roughly maximize the indices; however, there are no distributions which have a power-law index greater than two, *i.e.,* the results do not meet the condition necessary for nanoflare heating to be dominant.

Figure 3.8 presents the associations between $t_{\rm rel}$ and the energy ratio $\phi_{\rm Dop}$ and $\phi_{\rm nth}$. The top and bottom panels show enhancements detected using Doppler and nonthermal velocities, respectively. Black ticks and red circles represent the scatter plot of $\phi_{\rm Dop}$ and $\phi_{\rm nth}$. The horizontal solid line in each panel indicates where $\phi = 1$, which implies that the released thermal and Doppler motion (nonthermal) energies are balanced. The black and red dashed lines represent the medians of $\phi_{\rm Dop}$ and $\phi_{\rm nth}$, respectively. According to the medians, the released Doppler motion energy is 0.1 – 1% of the change in thermal energy. In addition, the released nonthermal energy is approximately 10 – 100% of the difference in thermal energy. There are no clear correlations between $t_{\rm rel}$ and ϕ.

3.6 Energy Balance Analysis

In this section, we estimate the energy balance between the energy losses by radiation and thermal conduction, and the heat flux inputs, for the detected enhancements.. First, we derive the radiative and conductive energy loss of the observed active region. Assuming the active region as a half-sphere, the radius r can be described as $r = \sqrt{S/\pi}$, where $S = 8.7 \times 10^{19}$ cm^2 represents the EIS observation area. First, radiative loss flux is estimated as follows:

$$F_r = n_e^2 P(T) V S^{-1} \tag{3.13}$$

$$P(T) = 10^{-17.73} T^{-\frac{2}{3}} \tag{3.14}$$

$$V = \frac{2}{3}\pi r^3 \tag{3.15}$$

where $n_e = 1.8 \times 10^9$ cm^{-3} and $T = 2.7 \times 10^6$ K represent the medians of electron density estimated by the `eis_density` function and temperature, respectively. The mean temperature was derived by

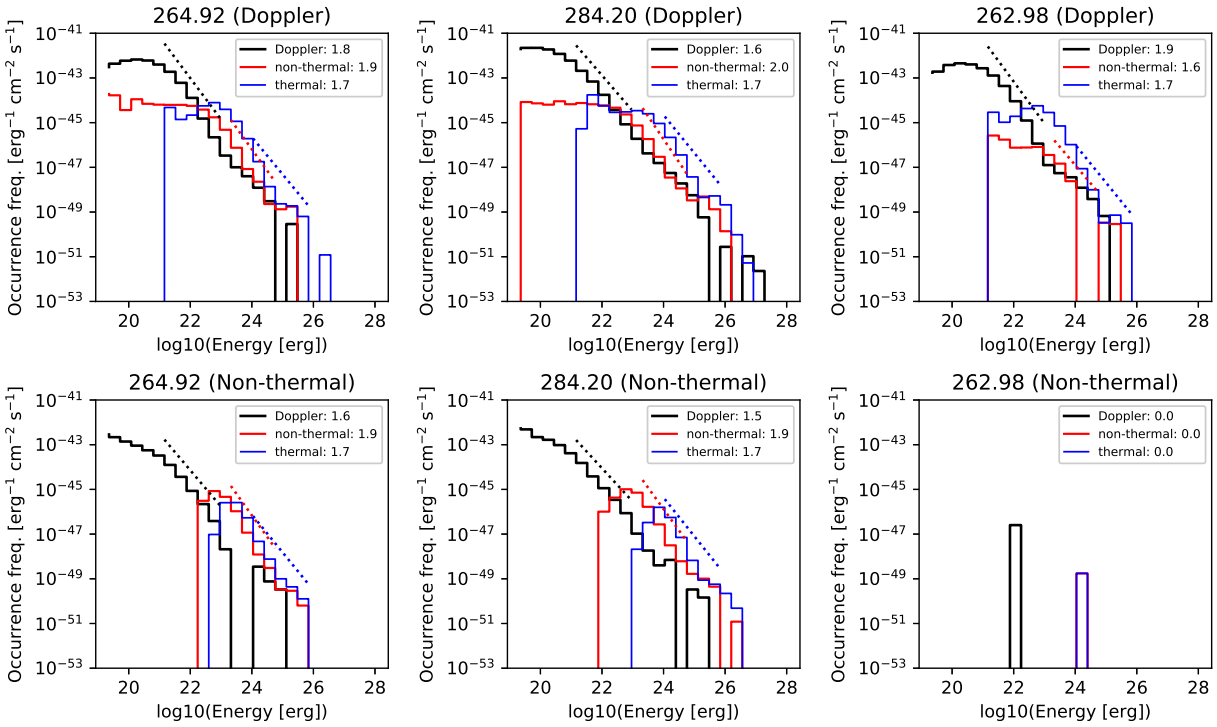

Figure 3.7: Occurrence frequency distributions of enhancements detected by Fe XIV (*left*), Fe XV (*center*), and Fe XVI (*right*). The top and bottom panels represent the distributions detected using Doppler and nonthermal velocities, respectively. The black, red, and blue solid lines represent distributions of Doppler motion, nonthermal energy, and thermal energy, respectively. The dotted lines indicate power-law fitted lines in the energy range of $10^{21} \leq E \leq 10^{23}$ [erg] (Doppler), $10^{23} \leq E \leq 10^{25}$ [erg] (nonthermal), and $10^{24} \leq E \leq 10^{26}$ [erg] (thermal). The numbers in the legend represent the power-law indices.

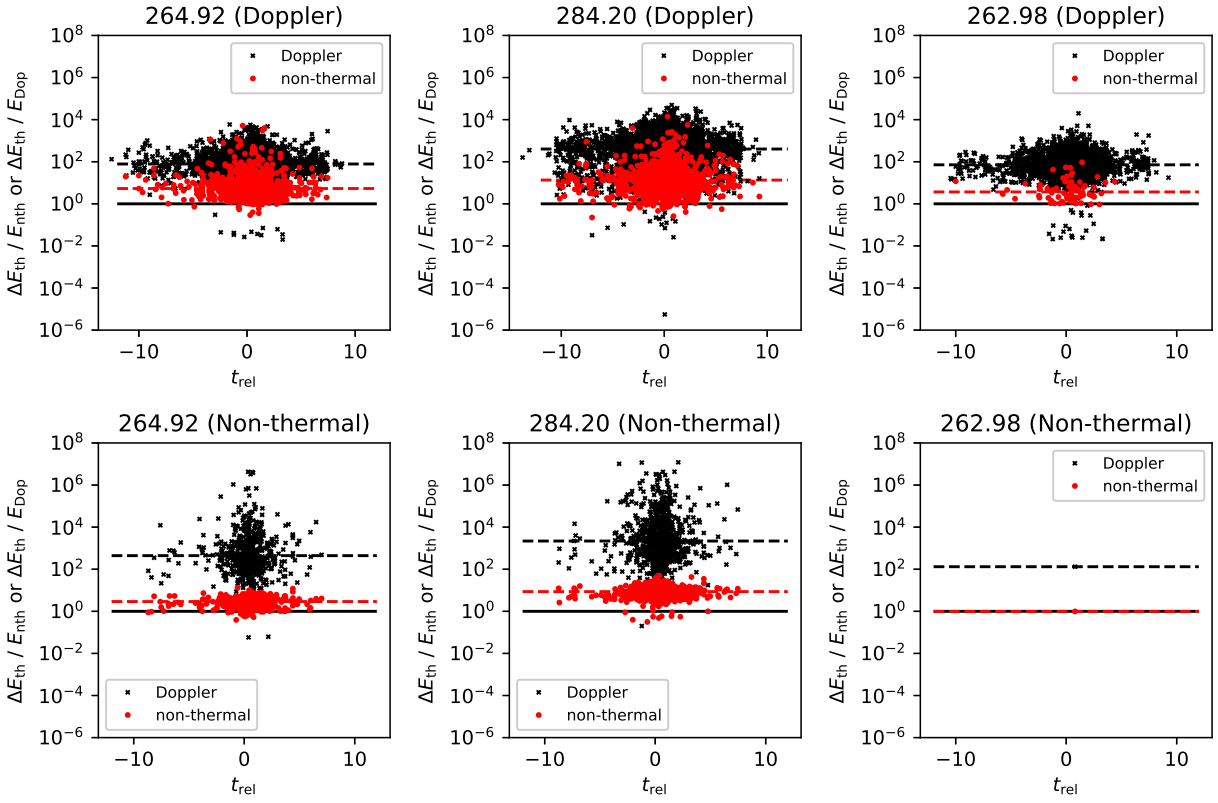

Figure 3.8: Relative times of an EIS energy enhancement to an AIA enhancement $t_{\rm rel}$ vs energy ratio $\phi_{\rm Dop}$ and $\phi_{\rm nth}$ estimated by Fe XIV (*left*), Fe XV (*center*), and Fe XVI (*right*). The top and bottom panels present the distributions of Doppler and nonthermal velocity enhancements, respectively. Black and red circles represent the distributions of $\phi_{\rm Dop}$ and $\phi_{\rm nth}$, respectively. The horizontal solid line indicates the location $\phi = 0$. The black and red dashed lines indicate the medians of $\phi_{\rm Dop}$ and $\phi_{\rm nth}$, respectively.

comparing the observed ratio of Fe XIV and Fe XVI with that of the CHIANTI database, although the estimated temperature depends on the selected ion pair. We used medians of density and temperature instead of their average values because these parameters are highly sensitive to the observational noise, especially in the case of dense plasma. $P(T)$ is the radiative loss function when $10^{6.3} < T < 10^{7.0}$ K (Raymond et al., 1976, Rosner et al., 1978). In contrast, conduction loss flux is derived as follows:

$$F_c = 2\kappa T^{\frac{7}{2}} \pi r S^{-1} \tag{3.16}$$

where $\kappa = 1.1 \times 10^{-6}$ erg cm^{-3} s^{-1} K$^{\frac{7}{2}}$ (Spitzer, 1956). Consequently, the radiative and conductive loss fluxes are 1.1×10^6 erg s^{-1} cm^{-2} and 1.4×10^7 erg s^{-1} cm^{-2}, respectively. Therefore, the total loss flux is approximately 1.5×10^7 erg s^{-1} cm^{-2}. This value is consistent with the result of Withbroe & Noyes (1977) ($\simeq 10^7$ erg s^{-1} cm^{-2}).

Second, we estimated the mean heating flux from AIA 211 Å intensity enhancements. We derived the flux using 1 h AIA observation maps similar to Figure 3.1 from 18:07:13 UT on November 09. From the light curve of each 4×4 macro-pixels, an AIA enhancement begins when the increase in intensity exceeds the threshold 3σ, where σ represents the 1 min mean intensity before the beginning of the enhancement. The events in adjacent pixels that have any overlap in the rising phase are regarded as a single event. The event area is calculated from the number of pixels where the enhancement spans. The released energy of each enhancement is defined as the change in the amount of thermal energy, similar to Equation 3.12. Electron densities n_{e0} and n_{e1} are defined as follows:

$$n_e = \sqrt{\frac{\mathrm{EM}}{S_{\mathrm{aia}}^{\frac{3}{2}}}} \tag{3.17}$$

$$\mathrm{EM} = \frac{I}{F(T)} \tag{3.18}$$

where EM, I, S_{aia}, and $F(T)$ represent the emission measure, intensity of AIA 211 Å, event area, and response of AIA 211 Å filter to plasma at temperature T (Boerner et al., 2012). The filling factor is assumed to be unity in this study. We assumed that T_0 and T_1 to be 1 MK and 5 MK similar to the method of Shimizu (1995). We avoid using the EIS density and temperature for this calculation because the temporal resolution of the EIS images is about 20 times longer than that of AIA. Moreover, there are many AIA enhancements which have a time scale shorter than the cadence of EIS observations as we will show later (Figure 3.9). Thus, the number of detected events is approximately 1.6×10^4 with the occurrence frequency of 1.2×10^{-21} s^{-1}cm^{-2}. The mean flux of the detected enhancements is approximately 1.2×10^5 erg s^{-1} cm^{-2}. Based on our results, the

Ion species	Doppler flux	Nonthermal flux	Thermal flux	Required flux
Fe XIV (Dop.)	3×10^1 (10^{-4}%)	1×10^2 (10^{-3}%)	7×10^2 (10^{-2}%)	1.5×10^7 (100%)
Fe XIV (nonth.)	4×10^0 (10^{-5}%)	5×10^1 (10^{-4}%)	1×10^2 (10^{-3}%)	
Fe XV (Dop.)	7×10^2 (10^{-2}%)	6×10^2 (10^{-3}%)	6×10^3 (10^{-2}%)	
Fe XV (nonth.)	1×10^1 (10^{-4}%)	2×10^2 (10^{-3}%)	9×10^2 (10^{-2}%)	
Fe XVI (Dop.)	2×10^1 (10^{-4}%)	2×10^1 (10^{-4}%)	3×10^2 (10^{-3}%)	
Fe XVI (nonth.)	3×10^{-3} (10^{-8}%)	4×10^{-1} (10^{-6}%)	4×10^{-1} (10^{-5}%)	

Table 3.2: Energy flux of EIS Doppler/nonthermal velocity enhancements [erg $s^{-1}cm^{-2}$] and contribution to the heating [%]

Doppler kinetic and nonthermal energies of AIA enhancements can be roughly estimated as 1.2×10^2 – 1.2×10^3 erg s^{-1} cm^{-2} and 1.2×10^4 – 1.2×10^5 erg s^{-1} cm^{-2}, respectively. Therefore, the total AIA energy flux is approximately 1.3×10^5 – 2.4×10^5 erg s^{-1} cm^{-2}, which is approximately 1 – 2% of the sum of the conduction and radiative loss fluxes.

We calculated the energy flux of the detected EIS Doppler motion and nonthermal enhancements accompanied by the AIA intensity enhancement as follows:

$$F_i = \sum ES^{-1}\tau^{-1} \tag{3.19}$$

where E represents the estimated Doppler, nonthermal or thermal energies of each enhancement. The observation duration τ is 30,831 s, as described in Section 3.2. Table 3.2 shows Doppler motion, nonthermal and thermal energy fluxes detected using Doopler/nonthermal velocity by each ion channel and their contribution to the active region heating. The fluxes depend on the wavelengths and velocities; however, the detected input flux is much less than the loss flux in any case. The ratio of contributions are roughly $F_{\rm Dop} : F_{\rm nth} : F_{\rm th} = 1 : 10 : 100$.

3.7 Discussion

In this study, we estimated the ratio of the difference in thermal energy $\Delta E_{\rm th}$ to $E_{\rm Dop}$ based on Doppler motion and $E_{\rm nth}$ based on nonthermal velocities using Hinode/EIS Fe XIV, Fe XV, and Fe XVI spectroscopic observations. As a result, $E_{\rm Dop}$ and $E_{\rm nth}$ tend to be 0.1 – 1% and 10 – 100% of $\Delta E_{\rm th}$ in the typical enhancements detected by all three wavelengths, respectively. The contribution of the energy fluxes of detected EIS velocity enhancements was less than 0.1% of the estimated

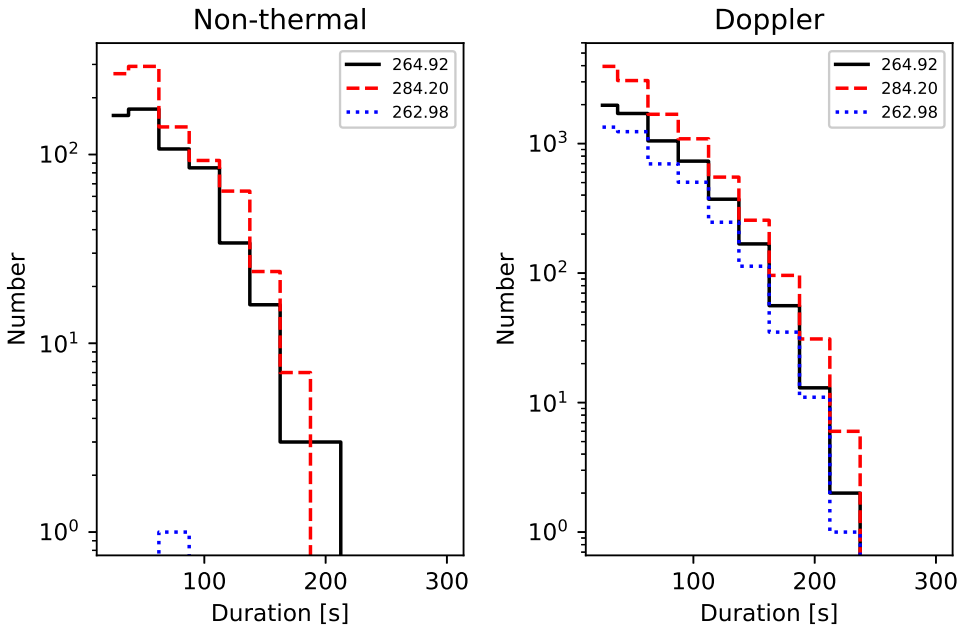

Figure 3.9: Distribution of durations from beginnings of AIA enhancements to their peaks, which have an EIS velocity enhancement between them. The left (right) panel shows the distribution of Doppler (nonthermal) velocity. The black, red, and blue dotted lines represent the histograms of Fe XIV, Fe XV, and Fe XVI, respectively.

total losses due to radiation and conduction for all three ion channels. Moreover, using the energy conversion rate (Section 3.5), we estimated the contribution of AIA transient brightenings to active region heating to be at most 2% of these losses. This shortage is probably caused by the lack of detection and/or the contribution of other processes.

Each histogram in Figure 3.9 represents a distribution of durations from the beginning of AIA brightening to its peak accompanying EIS velocity enhancement. The Black solid, red dashed, and blue dotted lines represent distributions derived from Fe XIV, Fe XV, and Fe XVI, respectively. The medians of durations derived from these distributions are approximately 48 s. We estimated the required cadence of EUV spectroscopic imaging observations to detect enhancements of Doppler and nonthermal velocities. As described in Section 3.5, the median of $t_{\rm rel}$ is approximately 0.4. Then, the time scale of medium EIS velocity enhancements is roughly estimated as $48 \times 0.4 \simeq 19$ s, whereas the cadence of Hinode/EIS data used in this study is 254 s. The next Japanese satellite mission, Solar-C/EUV High-throughput Spectroscopic Telescope (EUVST), will achieve a temporal

resolution that is approximately 10 times higher than that of Hinode/EIS. Therefore, the EUVST will provide a more accurate process of energy release during these transient brightenings after its launch in mid 2020s.

According to the distributions in Figure 3.7, the smallest released energy is much smaller than that of previous observations. However, the Doppler velocity is corrected using the median of each snapshot. This correction might cause underestimation of the Doppler velocity. In contrast, the Doppler and nonthermal energies estimated by Fe XVI are much larger than those of the other channels. This is probably because many pixels in this channel have spectra that do not have an adequate photon count to derive the velocities accurately, although we neglected darker pixels in the detection criteria.

We used some threshold for our detection criteria to avoid detecting noise as an event. Definitely, the looser the thresholds to use, the greater the number of events. However, as shown in Figure 3.7, the power-law indices are less than two in all occurrence frequency distributions. Therefore, the energy contribution of smaller events than those we detected in this study is not a dominant if we assume that the power-law index does not change even in smaller energy range.

There are some neglected processes and influential assumptions in our analysis. Schmelz et al. (2001) and Warren et al. (2008) revealed that a coronal loop contains plasma that has a wide temperature range, which implies that the loop consists of finer tubes. The volumetric filling factor of the loop was estimated to be approximately 10% by Warren et al. (2008). In contrast, Sakamoto et al. (2009) showed that the volumetric filling factors for *SXT* and the *Transition Region And Coronal Explorer* (TRACE: Handy et al., 1999) loops are $\simeq 2\%$ and $\simeq 70\%$, respectively. These results suggest that the filling factor depends on the observational wavelength. Accordingly, the input energy flux might be overestimated by an order of magnitude because we assume the filling factor as unity to estimate the AIA thermal energy. Moreover, we assumed that the ion temperature is the same as that of the electrons; however, Imada et al. (2009) reported that they have different temperatures, especially in an active region core. Non-equilibrium ionization (NEI) also affects the detection and energy estimation of impulsive heating events (Imada et al., 2011b, Orlando et al., 1999, Reale & Orlando, 2008). As for energy balance analysis, heating input from dark jets, those events showing Doppler shift but no enhancements in AIA images as reported by Young (2015), are neglected. The energy contribution of these events will be derived in the future works.

Chapter 4

Factors that determine the power-law index of an energy distribution of solar flares

4.1 Introduction

As described in Chapter 1, the power-law indices derived in previous studies were very different, despite this index being critical for evaluating the nanoflare heating model. Therefore, the motivation of this study was to reveal the factors that determine the power-law index of a flare occurrence frequency distribution. To this end, we investigated the dependence of the index on the solar activity, coronal features, released energy range, and AR properties. We compare temporal series of the power-law index derived by Sun-as-a-star observation and that of the sunspot number in Section 4.2.1. We present the differences in the power-law index in ARs, QS, coronal holes, and off-limb in Section 4.2.2. In Section 4.2.3, we discuss the occurrence frequency distributions from nanoflares to the largest flares. We investigate the relationships between certain AR parameters, such as the total unsigned flux and power-law index, in Section 4.2.4. Finally, we discuss possible scenarios that can explain the revealed dependences in Section 4.3.

4.2 Methods and Results

We used observation data that were obtained from the *Atmospheric Imaging Assembly* (AIA: Lemen et al., 2012) on board the *Solar Dynamics Observatory* (SDO: Pesnell et al., 2012). This instrument captures full-sun images of nine UV and EUV broadband channels. We selected six EUV channels (94, 131, 171, 193, 211, and 335 Å), which are responsive to the emission of coronal plasma (Boerner et al., 2012). The spatial and temporal resolutions of each channel were $0.6''$ and 12 s, respectively. The observation data are available at [1] JSOC. All AIA images that were used in this study, except for the Sun-as-a-star observation, were calibrated using the `aia_prep` routine that is provided in SolarSoftWare (SSW: Freeland & Handy, 1998).

4.2.1 Power-law Index vs Solar Activity

We performed a Sun-as-a-star observation using the AIA data over approximately 11 years to derive the occurrence frequency distribution of larger flares. In Sun-as-a-star observation, the intensity in a snapshot is integrated and only the temporal variation is analyzed, as with stellar observations. The observation duration used for this analysis was August 05, 2010 to December 31, 2020. We used the time series of the total intensity of each snapshot normalized by the exposure time for each channel. To reduce the artificial fluctuation, we only used data for which the `QUALITY` keyword was zero.

We detected significant intensity enhancements from the light curves for each year and each channel. First, we detected all of the enhancements from the light curve. The detection threshold was defined by the following equation:

$$\delta I > 3 \times I_{\rm avg}, \tag{4.1}$$

where δI and $I_{\rm avg}$ represent changes in the light curve from the beginning to the peak of enhancement and the 1 min average before the beginning of the enhancement, respectively. We neglected the enhancements of only a single snapshot to reduce the effect of noise on the analysis. Figure 4.1 presents an example of light curves and detection results. The blue and red ticks represent the beginnings and peaks of the detected enhancements, respectively.

We estimated the flare released energy of each enhancement, assuming that it was the change in thermal energy between the onset and peak. The thermal energy was estimated based on the

[1] `http://jsoc.stanford.edu/`

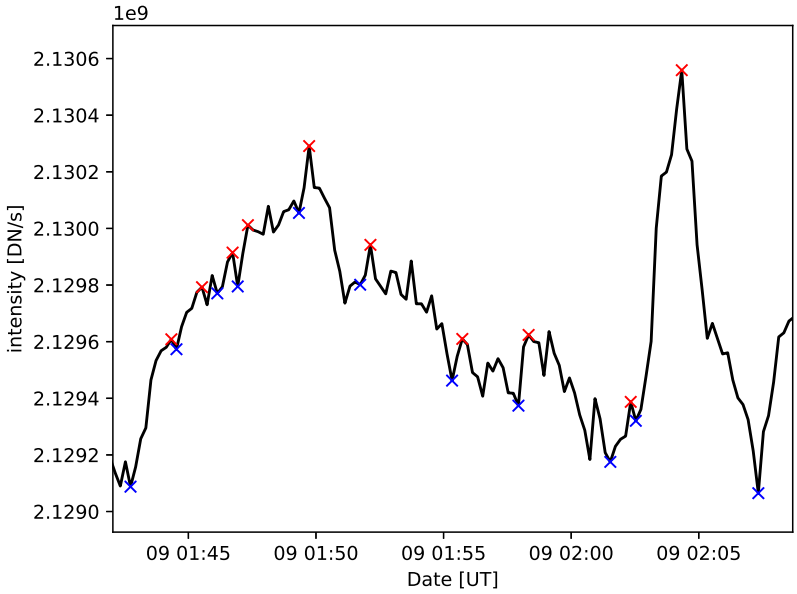

Figure 4.1: Example of obtained AIA light curves and detected enhancements. The blue and red ticks represent the beginnings and peaks of the enhancements.

Differential Emission Measure (DEM) calculated by the DeepEM code that was developed by Paul Write[2] . DeepEM is a convolutional neural network that is trained to output the DEM when six EUV AIA channels are input. The training was performed using the solutions of Cheung et al. (2015). We selected DeepEM for our analysis because other inversion methods (*e.g.,* Aschwanden et al., 2013b) would be too computationally heavy to calculate all of the AIA data that we used.

As described in Aschwanden et al. (2015), thermal energy can be calculated using the following equation:

$$E_{\rm th} = \sum_k 3k_{\rm B}V^{1/2}T_k{\rm EM}_k^{1/2}, \tag{4.2}$$

where $k_{\rm B}$, V, T_k, and ${\rm EM}_k$ represent the Boltzmann's constant, volume, temperature, and emission measure of the temperature range ΔT_k. The temperature is discretized in the logarithmic range of $\log T = 5.5, 5.6, ..., 7.2$ equidistantly.

As the DEM is derived from Sun-as-a-star observation, the event volume is assumed to be the entire coronal volume in the field-of-view. Therefore, we assumed the event volume as the following equation:

$$V = \frac{2}{3}\pi\{(R_{\rm AIA})^3 - R_\odot^3\}, \tag{4.3}$$

where $R_{\rm AIA} \simeq 897$ Mm and $R_\odot \simeq 696$ Mm represent the half-length of a side of the field-of-view of the AIA and solar radius, respectively.

Each panel in Figure 4.2 displays an occurrence frequency distribution of flares detected by AIA 193 Å as a function of energy for each year. The red solid line represents the power-law fitted line. The power-law distribution was effectively reproduced in the energy range of $10^{27} \lesssim E \lesssim 10^{30}$ erg. The fitted energy range was defined by the following procedures:

1. Determine the width of the energy range $\Delta E_{\rm fit}$ to be fitted.
2. Derive the power-law fitted line in the energy range of $E_{\rm min} \leq E \leq E_{\rm min} + \Delta E_{\rm fit}$, where $E_{\rm min}$ represents the minimum energy bin of the histogram.
3. Calculate the mean squared error (MSE) between the histogram and fitted line.
4. Shift the fitting energy range using the step of the energy bin size.
5. Perform 2 - 4 until the energy range reaches the maximum flare energy.

[2] `https://github.com/PaulJWright/DeepEM`

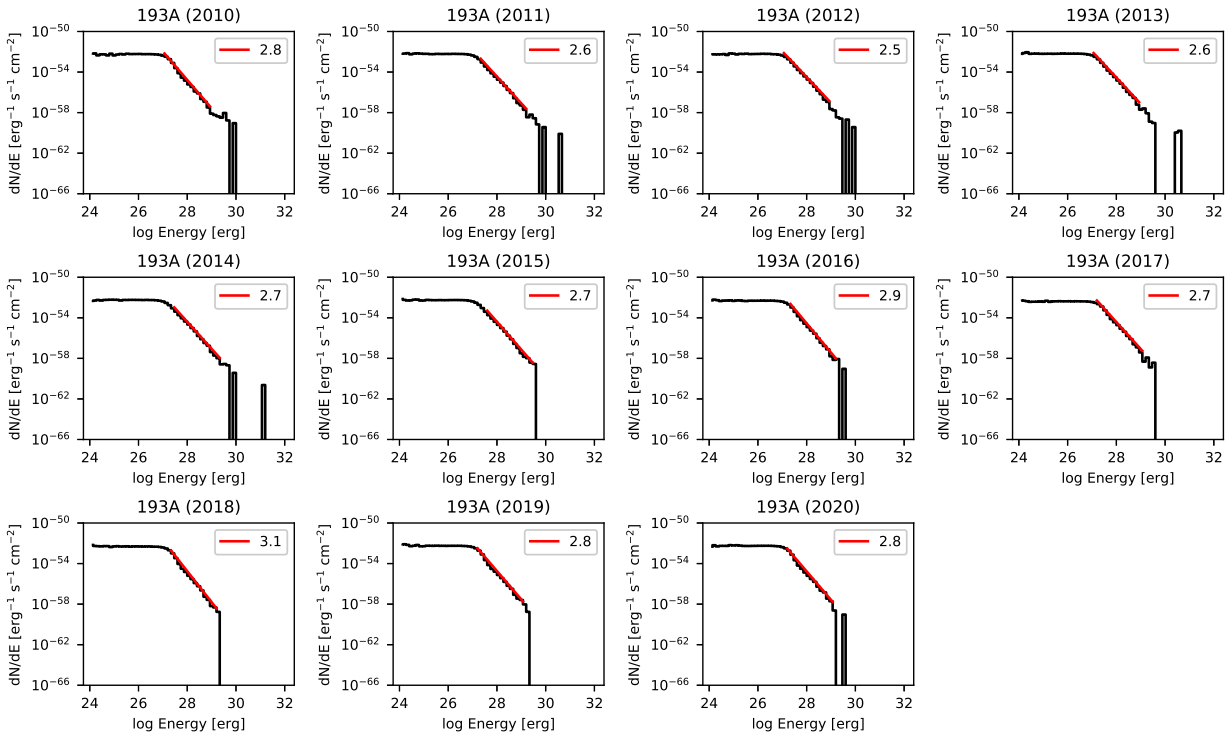

Figure 4.2: Energy distributions of flares detected by Sun-as-a-star observation using SDO/AIA 193 Å channel in each year. The red lines are the power-law fitted lines. The values in the legend are the power-law indices.

6. Obtain the fitted line of the energy range, where the MSE is the least and the power-law index is greater than 1.

In this study, we defined $\Delta E_{\rm fit} = 2$ in a logarithmic scale.

We compared the power-law index of the derived flare distribution in each year with the solar activity. The top panel of Figure 4.3 depicts the annual time series of the power-law index that was obtained from each AIA channel. The black line in the bottom panel indicates the time series of the monthly-averaged sunspot numbers. We used the monthly smoothed sunspot number of the Observed Solar Cycle Indices Data provided by [3]the Space Weather Prediction Center of NOAA. The red line indicates the annual moving average. This figure shows negative correlations between the sunspot number and power-law indices that were derived from all channels. The correlation coefficients are described in the legend in the top panel.

4.2.2 Power-law Index vs Coronal Features

We derived the flare occurrence frequency distribution in each coronal feature, including the ARs, QS, coronal holes (CHs), and off-limb. We used image series of the AIA EUV channels from 08:00 UT to 09:00 UT on February 25, 2014, including several ARs and CHs on the disk. First, we calculated 4×4 macro-pixel DEM maps in each snapshot using the DeepEM code. With reference to Adithya et al. (2021), we divided each image into ARs, QS, CHs, and off-limb based on the obtained DEM maps according to the following criteria:

1. ARs
   (a) Calculate the medians of the peak temperature T_p and emission measure EM_p from the derived DEM in each snapshot.
   (b) Detect the macro-pixels that satisfy $T_p > 1.3\times\mathrm{Median}(T_p)$ and $\mathrm{EM}_p > 1.3\times\mathrm{Median}(\mathrm{EM}_p)$.
   (c) Apply morphological closing with a 15×15 kernel to smooth the contours.
   (d) Determine the connected macro-pixels that have an area greater than 256 macro-pixels (4096 AIA pixels).
2. CHs
   (a) Detect the macro-pixels that satisfy $T_p < 0.8\times\mathrm{Median}(T_p)$ and $\mathrm{EM}_p < 0.8\times\mathrm{Median}(\mathrm{EM}_p)$.

[3]`https://www.swpc.noaa.gov/products/solar-cycle-progression`

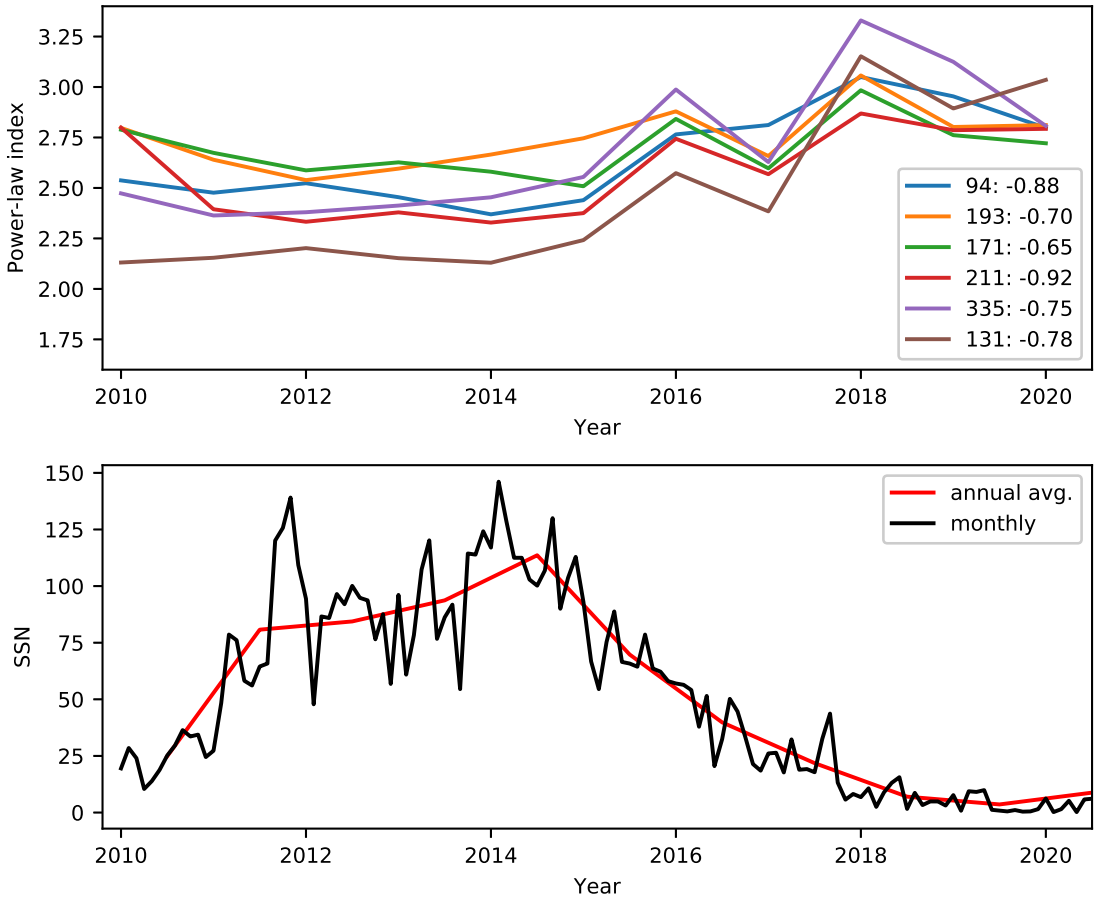

Figure 4.3: The top panel displays the annual time series of the power-law indices derived by Sun-as-a-star observation using each SDO/AIA channel. The bottom panel shows the monthly (black) and annual (red) time series of the sunspot number. The correlation coefficients between the power-law indices and yearly sunspot number are described in the legend of the top panel.

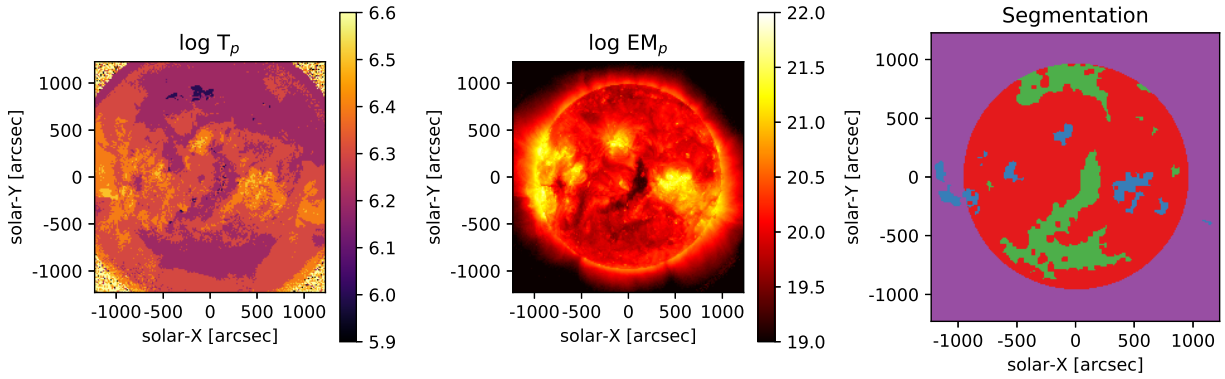

Figure 4.4: The left and middle panels show T_p and EM_p of the derived DEM calculated from the AIA EUV channels. The right panel presents an example of the segmentation results. The red, blue, green, and purple indicate the QS, ARs, CHs, and off-limb, respectively.

(b) Remove the macro-pixels where the distance from the disk center is greater than $R_\odot$.

(c) Apply morphological closing with a 15×15 kernel to smooth the contours.

(d) Determine the connected macro-pixels that have an area greater than 256 macro-pixels.

3. QS

(a) Identify the macro-pixels where the distance from the disk center is less than $R_\odot$.

(b) Determine macro-pixels other than ARs or CHs.

4. Off-limb

(a) Determine the macro-pixels where the distance from the disk center is greater than $R_\odot$.

(b) Identify macro-pixels other than ARs.

Figure 4.4 displays an example of the macro-pixel maps of the T_p (left), EM_p (center), and segmentation results (right). The red, blue, green, and purple in the segmentation results indicate the QS, ARs, CHs, and off-limb, respectively.

We applied the macro-pixel method as used in Shimizu (1995) so as not to miss faint enhancements and to reduce the computational cost. As with the segmentation, the size of a macro-pixel was 4×4 in this study. We detected significant enhancements from the light curve in each macro-pixel. The detection criterion was the same as that of the Sun-as-a-star observation. When rising phases

of multiple enhancements overlapped at adjacent macro-pixels, they were regarded as a single event. The segment of each event was assigned based on its center of gravity. The thermal energy was estimated using equation 4.2 as well. However, the event volume V was assumed to be $S^{3/2}$, where S represents the event area.

Figure 4.5 presents the energy distributions of flares detected by AIA 171 Å in the QS (top left), ARs (top right), CHs (bottom left), and off-limb (bottom right) in 2014 (solar maximum). The power-law fitting criterion was the same as that of the Sun-as-a-star observation. N represents the number of detected events. The power-law distributions were effectively reproduced in all of the segments.

Figure 4.6 depicts the power-law indices in each region and of the events that were detected in each channel. The results demonstrate that the power-law index of the flares detected in the ARs tended to be smaller than those of the QS, CHs and off-limb. This result appears to be consistent with the negative correlation between the power-law index and sunspot number. In darker channels (94, 131, and 335 Å), the derived distributions sometimes could not be fitted by a single power-law using our algorithm owing to the lack of an energy range of the detected events.

4.2.3 Power-law Index vs Released Energy

Figure 4.7 depicts the concatenated energy distribution using the results of the Sun-as-a-star observation in 2014 and the macro-pixel AR observations. The values in the legend represent the power-law indices. The power-law index was almost consistent over the energy range of $10^{24} \lesssim E \lesssim 10^{30}$ erg. In a higher energy range, the index increased, which is clearly shown in the result of the 193 and 171 Å channels. We discuss this point in Section 4.3.

4.2.4 Power-law Index vs AR Properties

We used the Spaceweather HMI Active Region Patch (Bobra et al., 2014, SHARP) dataset to investigate the dependence of the power-law index on the AR properties. SHARP includes various space weather parameters that are calculated from the photospheric vector magnetic field. We used the data series of `hmi.sharp_720s` in this study. Table 4.1 presents the SHARP parameters compared to the power-law indices in this study. Thousands of AR data are stored in the dataset; however, it is difficult to investigate all of the ARs owing to the computational cost. Therefore, we selected 108 ARs from the largest area in the available data for the analysis. We obtained six AIA EUV observation data over 20 min for each AR. The beginning of the observation was when

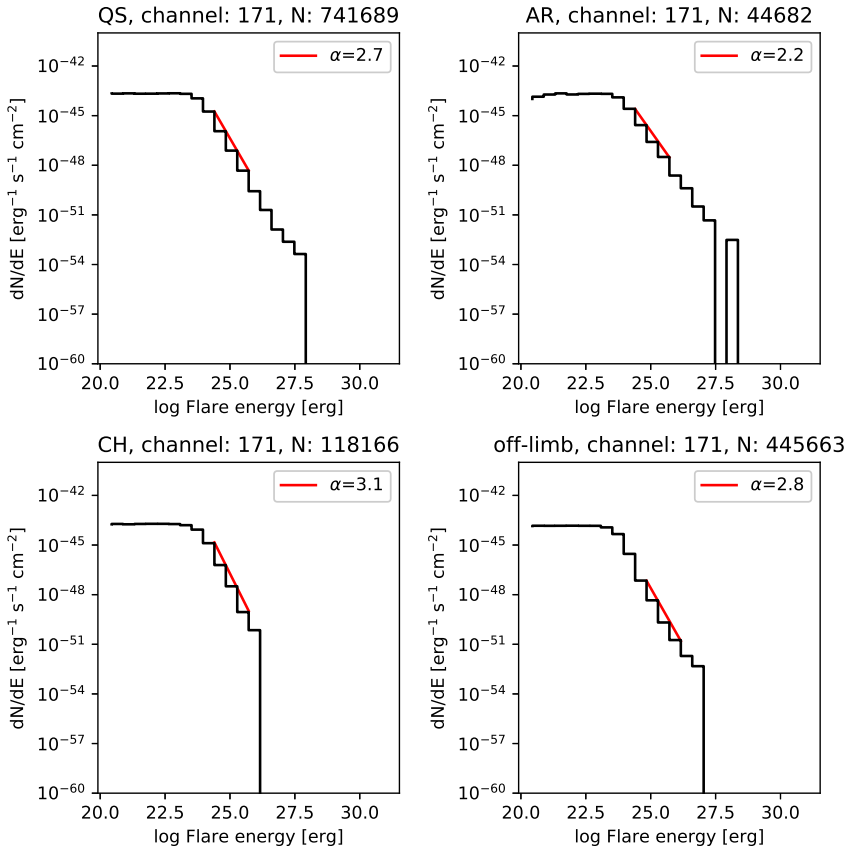

Figure 4.5: Energy distributions of flares detected in QS (top left), ARs (top right), CHs (bottom left), and off-limb (bottom right) using AIA 171 Å. The red lines are the power-law fitted lines defined by the procedure described in Section 4.2.1. N represents the number of detected events.

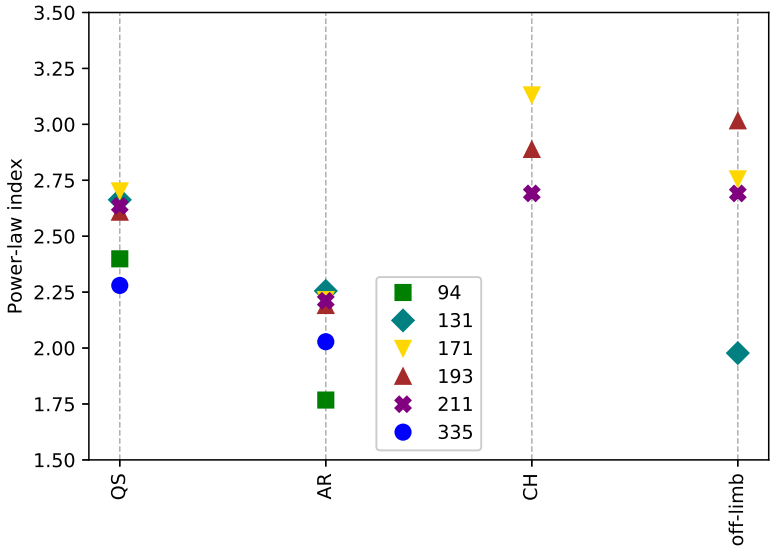

Figure 4.6: Power-law indices of detected flares using each AIA channel in QS, ARs, CHs, and off-limb.

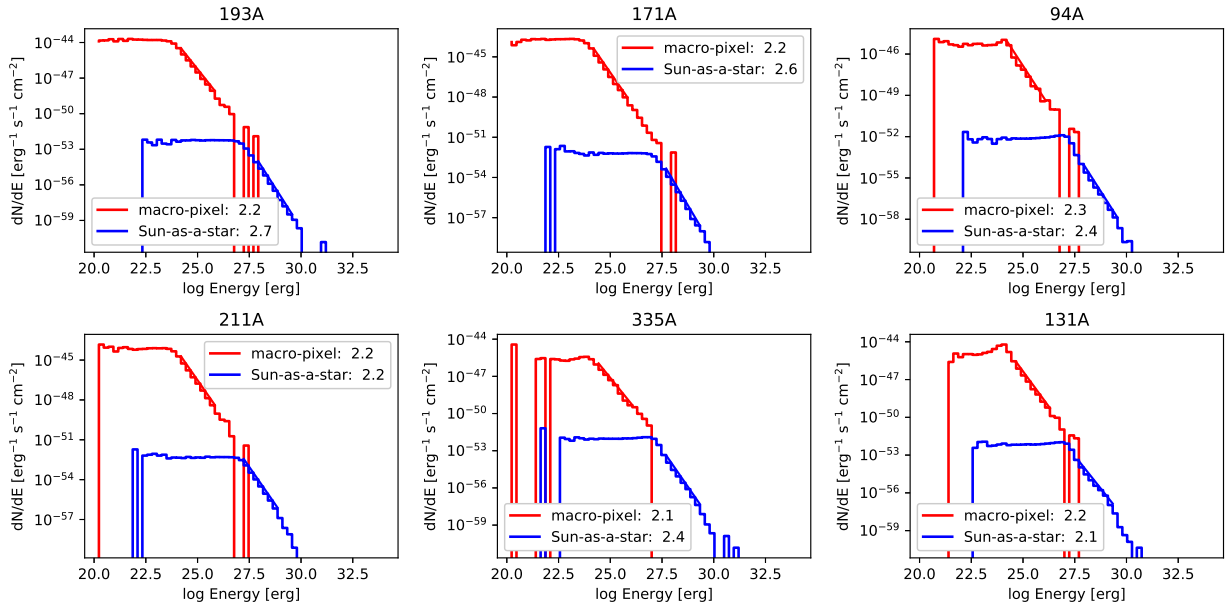

Figure 4.7: Energy distributions of flares derived by Sun-as-a-star (blue) and macro-pixel AR (red) observations with SDO/AIA EUV channels. The solid lines indicate the power-law fitted lines that were derived by the criterion described in Section 4.2.1. The values in the legend represent the power-law indices.

SHARP keyword	Description
USFLUX	Total unsigned flux
MEANGAM	Mean angle of field from radial
MEANGBT	Horizontal gradient of total field
MEANGBZ	Horizontal gradient of vertical field
MEANGBH	Horizontal gradient of horizontal field
MEANJZD	Vertical current density
TOTUSJZ	Total unsigned vertical current
MEANALP	Twist parameter
MEANJZH	Current helicity
TOTUSJH	Total unsigned current helicity
ABSNJZH	Absolute value of net current helicity
SAVNCPP	Sum of modulus of net current per polarity
MEANPOT	Proxy for mean photospheric excess magnetic energy density
TOTPOT	Proxy for total photospheric magnetic free energy density
MEANSHR	Shear angle
SHRGT45	Fractional of area with shear greater than 45°
R_VALUE	Unsigned flux R (Schrijver, 2007)
SIZE_ACR	Projected area of active pixels on image

Table 4.1: SHARP parameter list compared to power-law indices (see Bobra et al. (2014) for further details.)

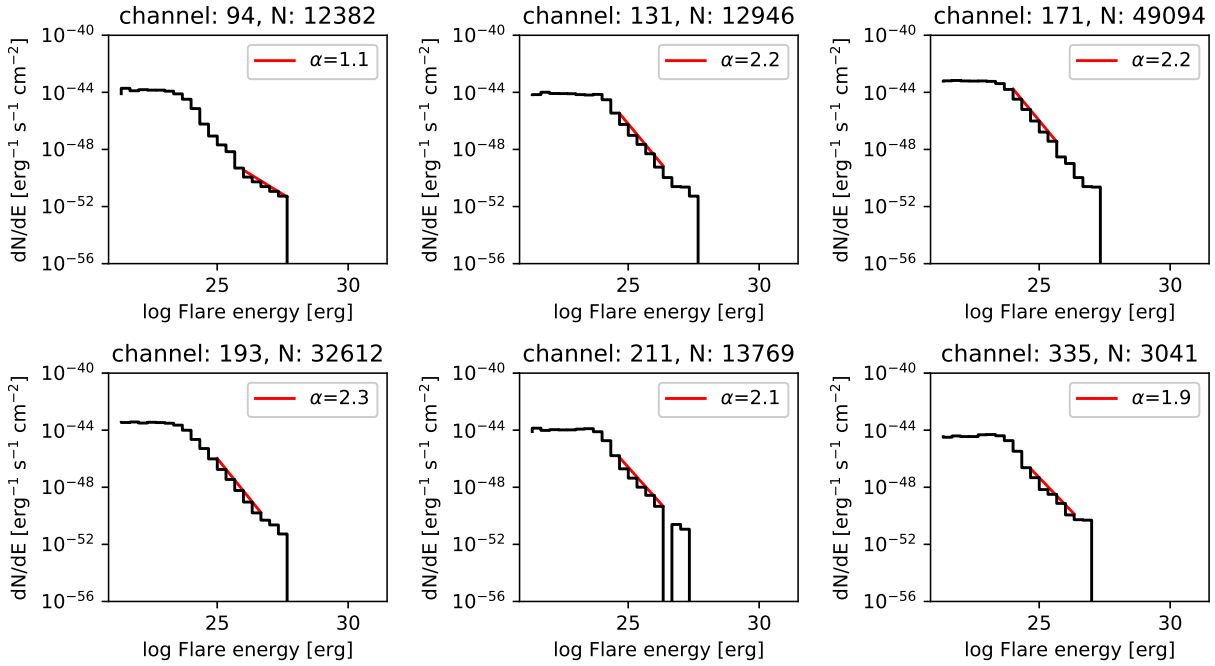

Figure 4.8: Energy distributions of flares in an AR (HARP5541) detected by each AIA channel. The red lines are the power-law fitted lines defined using the procedure described in Section 4.2.1.

the mean longitude of the AR reached the solar meridian to reduce the effects of a center-to-limb variation. The coordinates of these images were calibrated using the `LAT_MIN`, `LON_MIN`, `LAT_MAX`, and `LON_MAX` quantities in the SHARP dataset and the Stonyhurst heliographic coordinate of each AIA pixel calculated by the `Sunpy` modules (Mumford et al., 2020). The detection criterion and energy estimation method were the same as those in the previous analysis.

Figure 4.8 depicts an example of the energy distributions of flares detected in the SHARP AR by each AIA channel. The HARP number of this AR was 5541. The red line indicates the power-law fitted line, which was derived using the procedure described in Section 4.2.1.

We investigated the dependences of the power-law index on the 18 SHARP quantities listed in Table 4.1 for 108 regions. For example, Figure 4.9 presents the relationship between the power-law index and total unsigned flux (USFLUX) of the ARs in each AIA channel. Each tick corresponds to the SHARP AR. The black lines are fitted to the data points using least squares. Weak negative correlations can be observed between the factors in all channels.

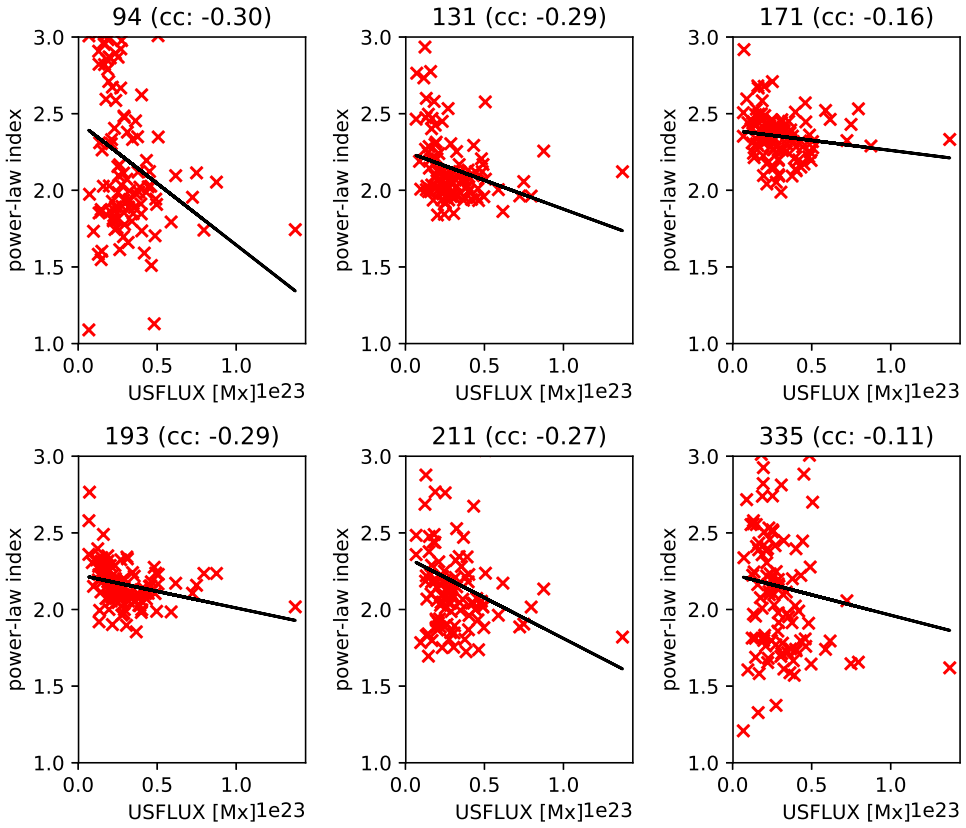

Figure 4.9: Scatter plot of unsigned magnetic flux of each AR and power-law index of energy distribution of flares detected in each AIA channel. The black lines are the linear least-squares regression fits to the data points.

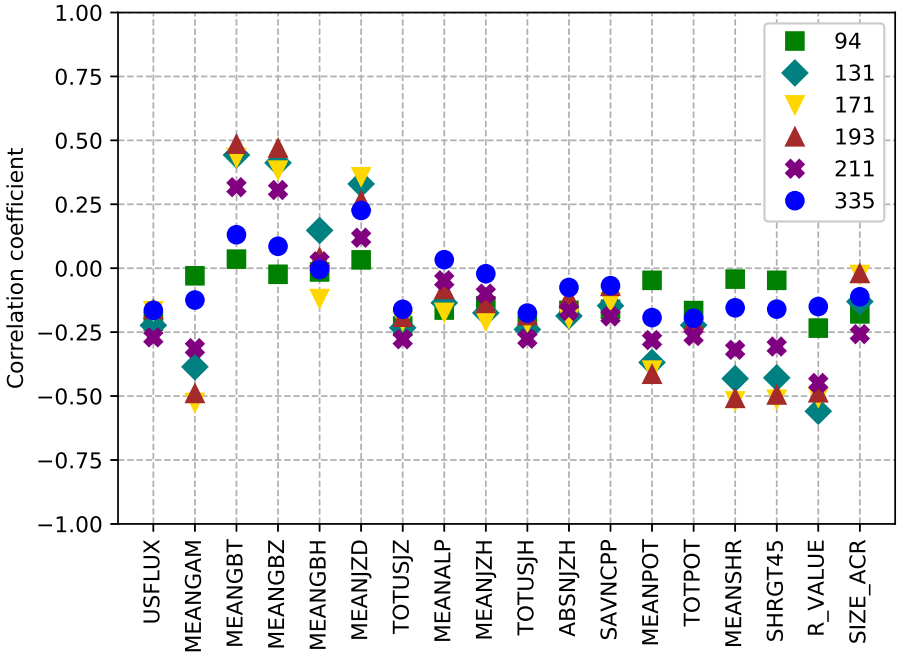

Figure 4.10: Correlation coefficients between power-law indices estimated by each AIA EUV channel and SHARP quantities.

Figure 4.10 depicts the correlation coefficients between the SHARP parameters and power-law index derived from each AIA channel. In particular, MEANGBT, MEANGBZ, and MEANJZD exhibited strong positive correlations with the power-law index. Vertical current density means rotationality, and Fursyak (2018) revealed that a higher mean vertical current density results in a higher flare index of the AR. However, MEANGAM, MEANPOT, MEANSHR, SHRGT45, and R_VALUE exhibited relatively strong negative correlations. These parameters are also important indicators for flare prediction studies (*e.g.,* Hazra et al., 2020, Yi et al., 2021). In general, ARs with more magnetic free energy tend to have smaller power-law indices.

4.3 Discussion and Summary

We statistically investigated the dependences of the power-law index of the energy distribution of flares on the solar activity, coronal features, released energy, and AR parameters. Our findings are summarized as follows:

1. The yearly power-law index derived by the Sun-as-a-star observation exhibits a negative correlation with the sunspot number.
2. The power-law index of detected flares in ARs is smaller than that of the QS and CHs.
3. The power-law index is almost constant in the energy range of $10^{24} \lesssim E \lesssim 10^{30}$ erg.
4. Active regions with greater magnetic free energy density, unsigned magnetic flux, and shear angles tend to have smaller power-law indices.

According to the first, second, and fourth results, the power-law index of the flares that are detected in magnetically active (flare productive) regions becomes smaller than those of the QS and relatively calm ARs. These results explain the differences in the indices in previous studies, as described in Table 1.2 (QS studies reported greater power-law indices than those of AR studies). The third result suggests that the energy release process is consistent, regardless of the energy scale. It appears from Figure 4.7 that the power-law index becomes larger in a higher energy range, especially in the 193 and 171 Å channels. This gap is probably caused by the difference in the analysis methods: whereas the macro-pixel method focused on AR cores, as illustrated in Figure 4.4, the Sun-as-a-star observations of these channels respond to emissions from coronal loops and QS. Moreover, with the exception of certain ARs, almost all of the power-law indices are greater than 2, which supports the nanoflare DC heating model.

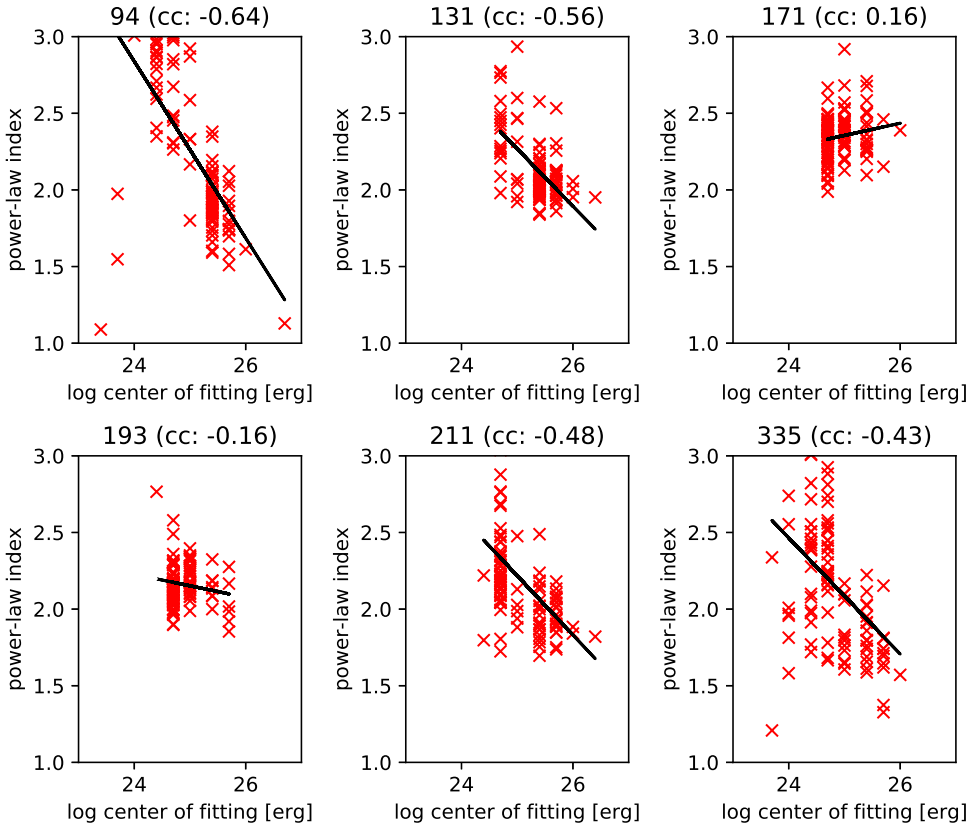

Figure 4.11: Scatter plot of power-law index of each AR and central energy of fitting. The figure format is the same as that of Figure 4.9.

Based on the above results, we describe two scenarios for the energy release process. The first is that the physical process of energy release is dependent on the magnetic properties. Using 1.5D MHD simulations, Antolin et al. (2008) suggested that a coronal loop that is heated by nanoflares has a smaller power-law index than that of wave heating. Therefore, our results imply that the ARs are mainly heated by nanoflares (magnetic reconnections), whereas the QS is heated by Alfvén waves. Moreover, the ratio of the nanoflare and wave heating is dependent on the magnetic properties, even among ARs. However, in this scenario, when nanoflare heating is dominant, the power-law index becomes smaller than 2, which does not support the nanoflare heating model.

To investigate this scenario in detail, we analyzed the dependence of the power-law index on its fitting energy range. Figure 4.11 presents scatter plots of the index and central energy of the

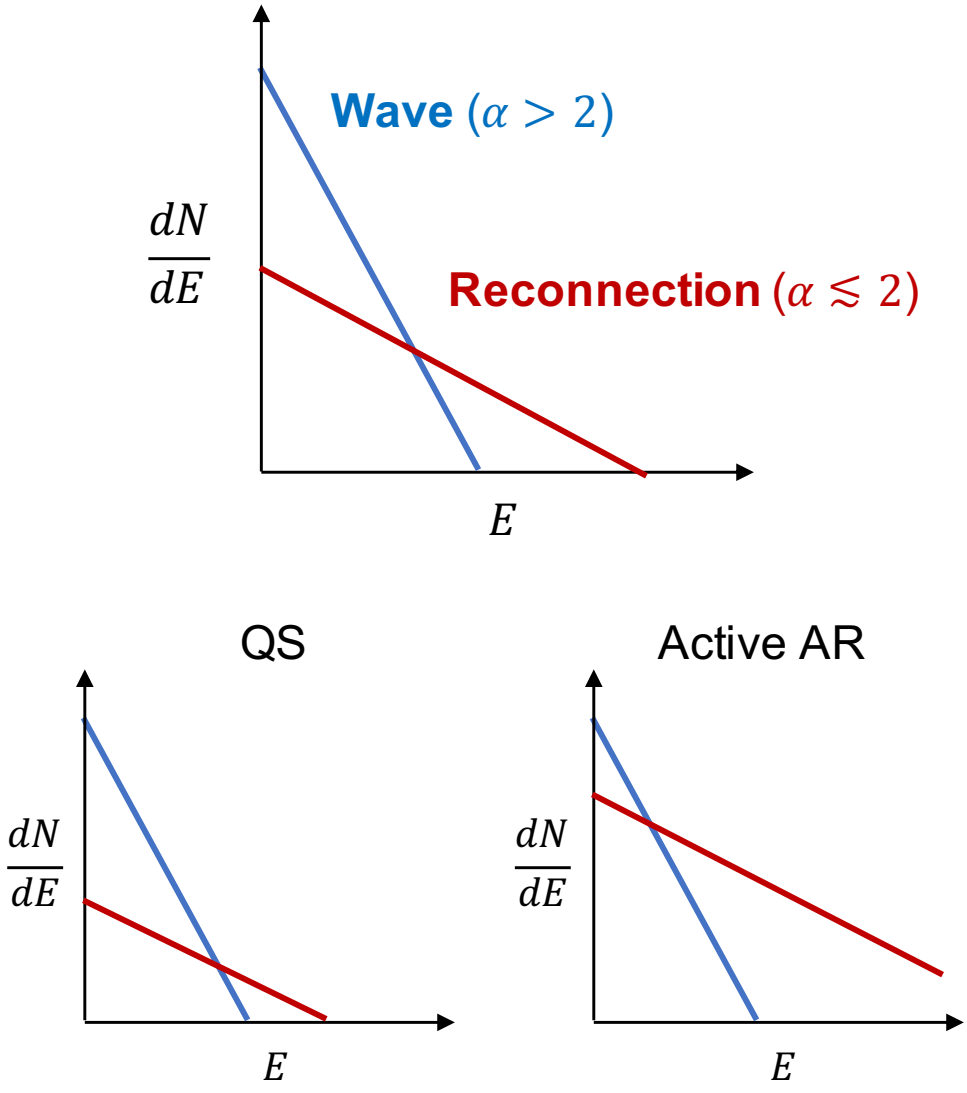

Figure 4.12: Energy distributions for former possible scenario. In QS, the distribution of waves stands out owing to the absence of reconnections (bottom left). In active ARs, the distribution of waves is hidden by that of reconnections (bottom right).

fitting. This figure indicates that the hotter channels (94, 131, 211, and 335 Å) exhibited negative correlations between the index and fitting range. According to this result and the former scenario, we suggest the energy distribution of nanoflares (waves and magnetic reconnections), as illustrated in Figure 4.12. The distribution of waves has a power-law index greater than 2 and smaller event energy, whereas the power-law index of magnetic reconnection may be smaller than 2 in a higher energy range. In QS, the distribution of waves stands out owing to the lack of reconnections, and thus, the total power-law index may be large. However, in active ARs, the distribution of waves is hidden by that of reconnections, and therefore, the total power-law index becomes small. This broken distribution can be clearly observed in Figure 4.8.

The other scenario is that the "apparent" power-law index varies, but the "actual" power-law index is consistent, regardless of the region. For example, an overlap of enhancements along the line-of-sight direction appears to cause the underestimation of the power-law index (larger events dominate). The overlap appears to occur easily because there are multiple sub-structures in the resolved coronal loops (Viall & Klimchuk, 2012, Warren et al., 2008) and they are probably smaller than a single AIA pixel (Kawai & Imada, 2021a, Tajfirouze et al., 2016). However, in this scenario, the power-law index that is derived by Sun-as-a-star observation should be smaller than that of the macro-pixel method because there are more overlapped events in Sun-as-a-star observation. Alternatively, a higher event occurrence rate results in more missed enhancements owing to the observation limitation. Aschwanden & Dudok de Wit (2021) identified the positive correlation between the sunspot number and power-law index of the waiting-time distribution of flares. The occurrence rate of smaller events is higher than that of larger events. Therefore, a lack of observation cadence may result in the underestimation of the power-law index.

The degradation of the instrument used is one of the concerns in our analysis, because we used satellite data spanning 10 years. Therefore, we investigated the dependence of the power-law index on the observation date using the ARs studied in Section 4.2.4. Figure 4.13 depicts the relationship between the power-law index and observation date (days from May 01, 2010) in each AIA channel. As indicated in this figure, no significant effects of the degradation on the power-law index analysis were observed.

We assumed the flare released energy to be the change in thermal energy. However, this assumption is not strictly correct owing to the cooling and distribution to the Doppler motion and nonthermal energies (Kawai & Imada, 2021b). Moreover, the non-equilibrium of ionization may affect the detection and energy estimation in the case of impulsive heating (Imada et al., 2011a, Orlando et al., 1999, Reale & Orlando, 2008).

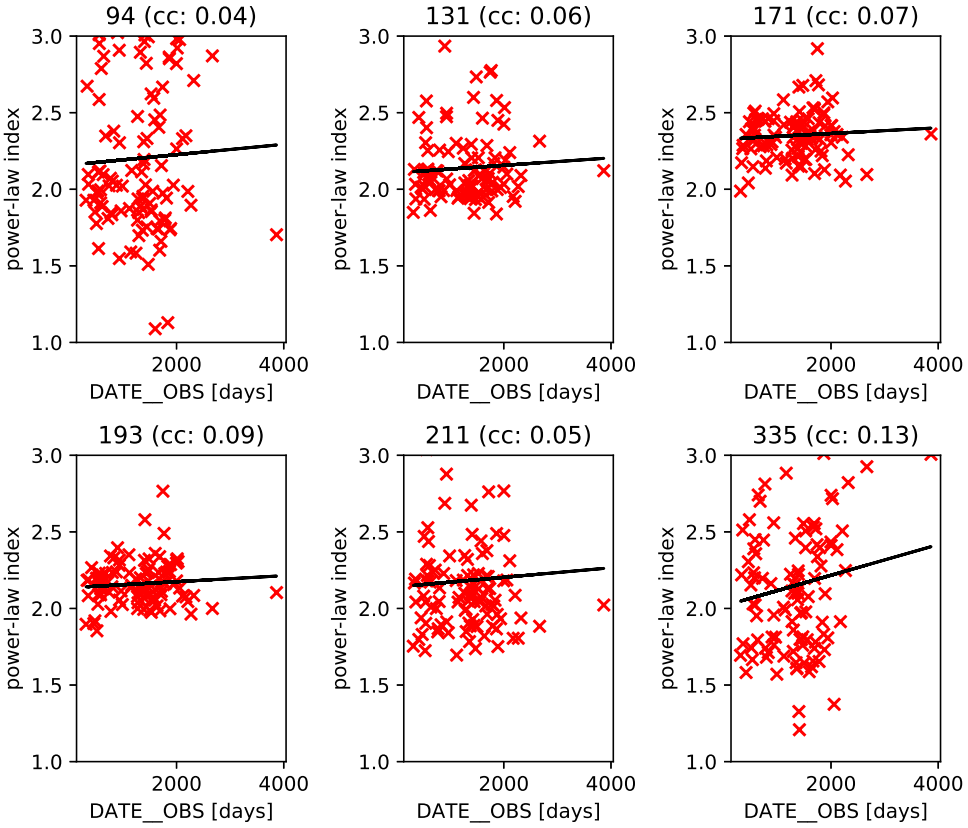

Figure 4.13: Scatter plot of observation date (days from May 01, 2010) of each AR and power-law index. The figure format is the same as that of Figure 4.9.

Chapter 5

Discussion

5.1 Dependence of power-law index on temporal resolution

We have to discuss why the power-law index of our study (Chapter 4) is much higher than that derived by previous studies. According to the consistency of power-law index between Sun-as-a-star observation and macro-pixel method, the spatial resolution is probably not so important to derive the power-law index accurately. Therefore, in this section, we investigated the effect of temporal resolution on power-law index. We used a light curve of the SDO/AIA 193 Å in 2014, which is the same as that used in Sun-as-a-star observation in Chapter 4. We changed the temporal resolution (sampling frequency) of this light curve and apply the event detection, energy estimation, and fitting procedures described in Chapter 4 to them.

Figure 5.1 represents energy distributions of flares detected by SDO/AIA 193 Å Sun-as-a-star observation with sampling cadence ranging from 24 to 576 s. Red lines are power-law fitted lines. This figure shows that the lower sampling frequency, the smaller power-law index. Figure 5.2 shows relationship between power-law index and sampling cadence with comparing previous studies. Black ticks are power-law index derived in this study. Color circles are those of previous studies. From the result, at least temporal resolution is more important than spatial resolution to derive the power-law index accurately. In addition, this figure suggests that the temporal resolution of the SDO/AIA might not be sufficient to derive the accurate power-law index. According to this figure, the value of Shimizu (1995) seems to deviate significantly from the tendency. This is probably because Shimizu (1995) observed soft X-rays whereas the other studies used EUV telescopes. Time scale of soft X-ray enhancement is smaller than that of EUV. Therefore, temporal resolution required to derive

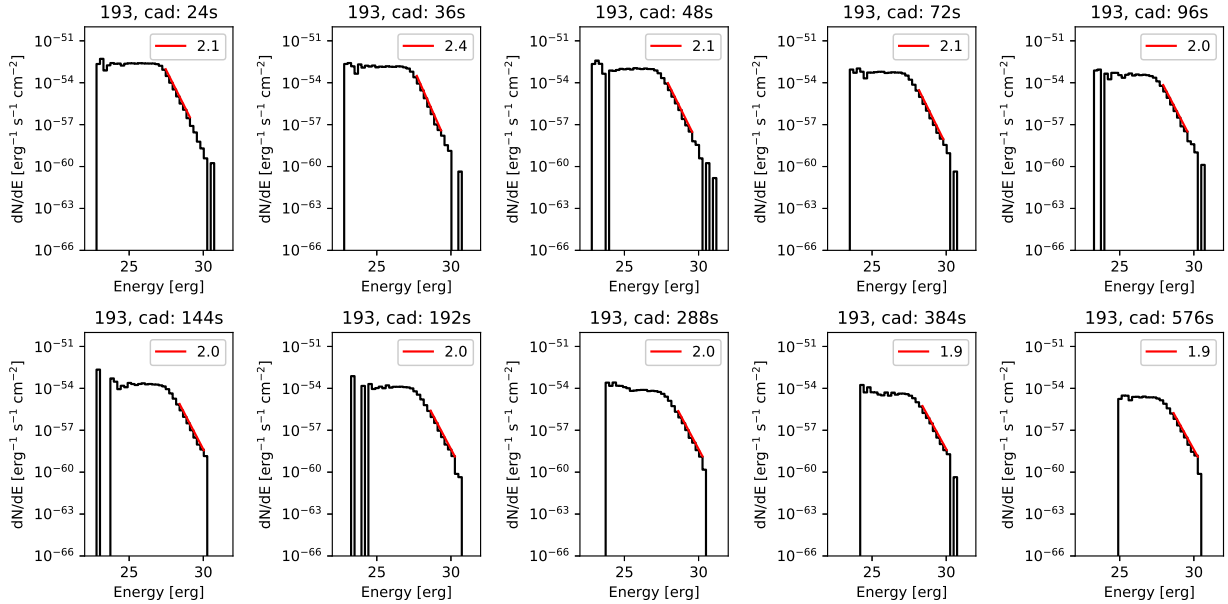

Figure 5.1: Energy distributions of flares detected by SDO/AIA 193 Å Sun-as-a-star observation with various sampling cadence. Red lines are power-law fitted lines.

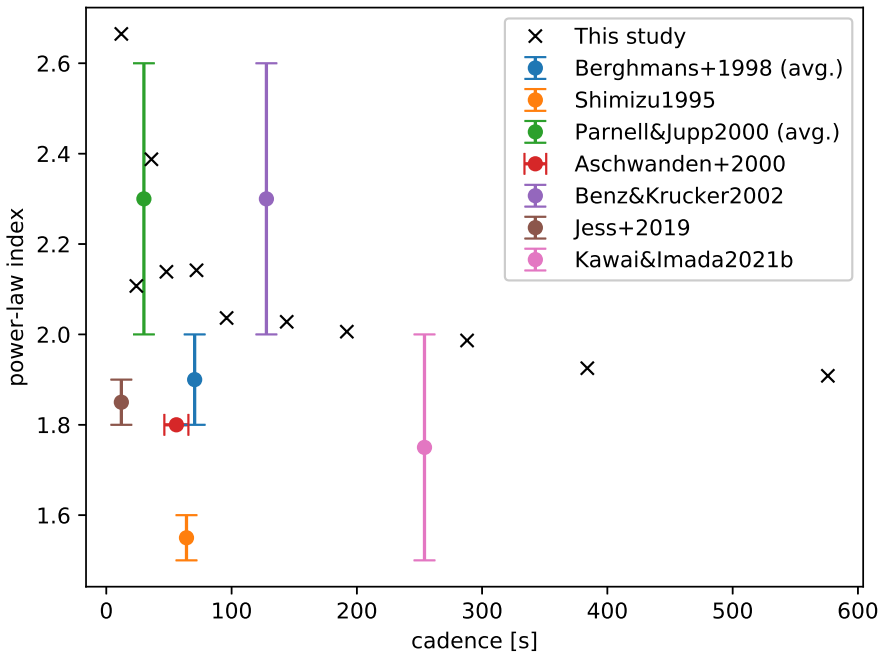

Figure 5.2: Relationship between power-law index and sampling cadence.

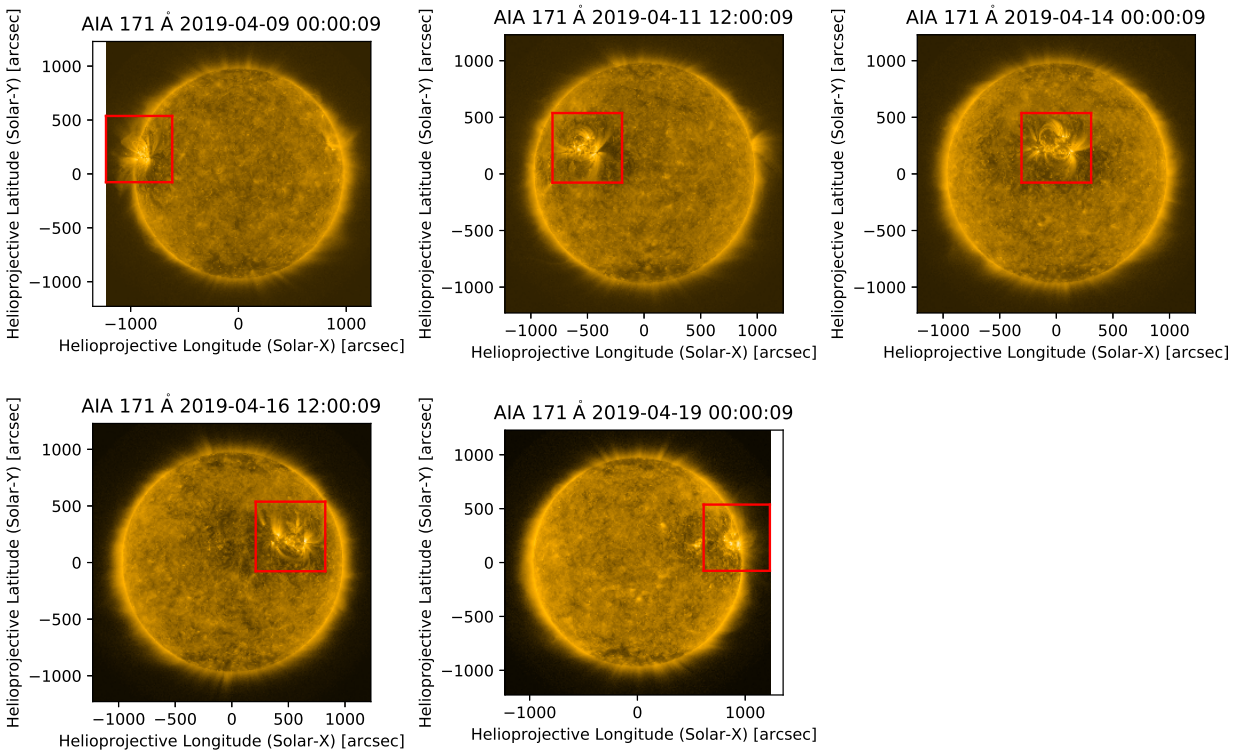

Figure 5.3: The first snapshot of each observation duration obtained from SDO/AIA 171 Å. Red squares indicate the location of AR NOAA 12738.

an accurate power-law index might be higher than that in EUV.

5.2 Center-to-limb variation of power-law index

To verify the scenario that the overlap of events in line-of-sight direction causes underestimation of "apparent" power-law index, first we investigate the center-to-limb variation of it. If the power-law index has dependence on its location, the scenario may be plausible. We used data of an AR NOAA 12738 in five phases (east limb, mid-east, meridian, mid-west, and west limb). Figure 5.3 shows the beginning of each observation duration obtained from SDO/AIA 171 Å. Red squares are locations of the target AR. Each observation duration is 20 min. We discriminated the AR from each snapshot as following criteria:

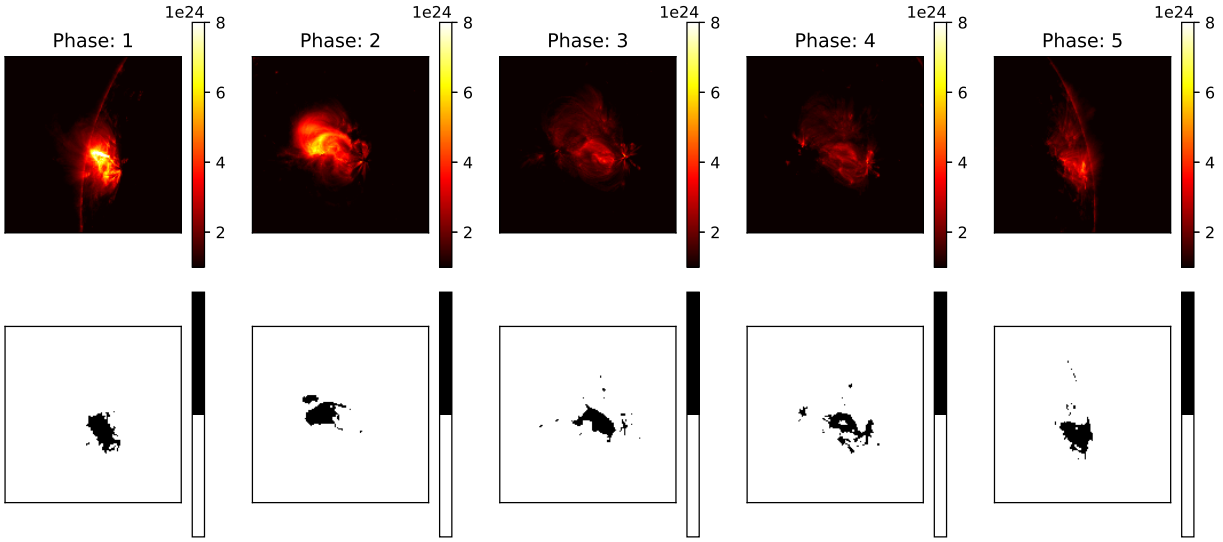

Figure 5.4: Top panels show mean thermal energy maps derived using DeepEM code. Black in bottom panels indicates discriminated AR pixels.

1. Calculate mean thermal energy in each pixel of cropped images (red square in Figure 5.3) using DEM derived by DeepEM code.

2. Detect pixels which have thermal energy greater than 98 percentile in each snapshot.

3. Apply morphological closing with 9×9 kernel to smooth the contours.

Figure 5.4 shows examples of mean thermal energy maps (top panels) and locations of identified AR (black in bottom panels) in each observation duration. We only analyzed events occurred on the AR pixels here. Event detection, energy estimation, and fitting procedures are same as those in the SHARP observation in Chapter 4.

Figure 5.5 shows energy distribution of flares detected by SDO/AIA 193 Å of AR 12738 in east limb (top-left), mid-east (top-center), meridian (top-right), mid-west (bottom-left), and west limb (bottom-center). As a result, the power-law index of an AR does not have dependence on its location. This irrelevance does not support the event overlapping scenario.

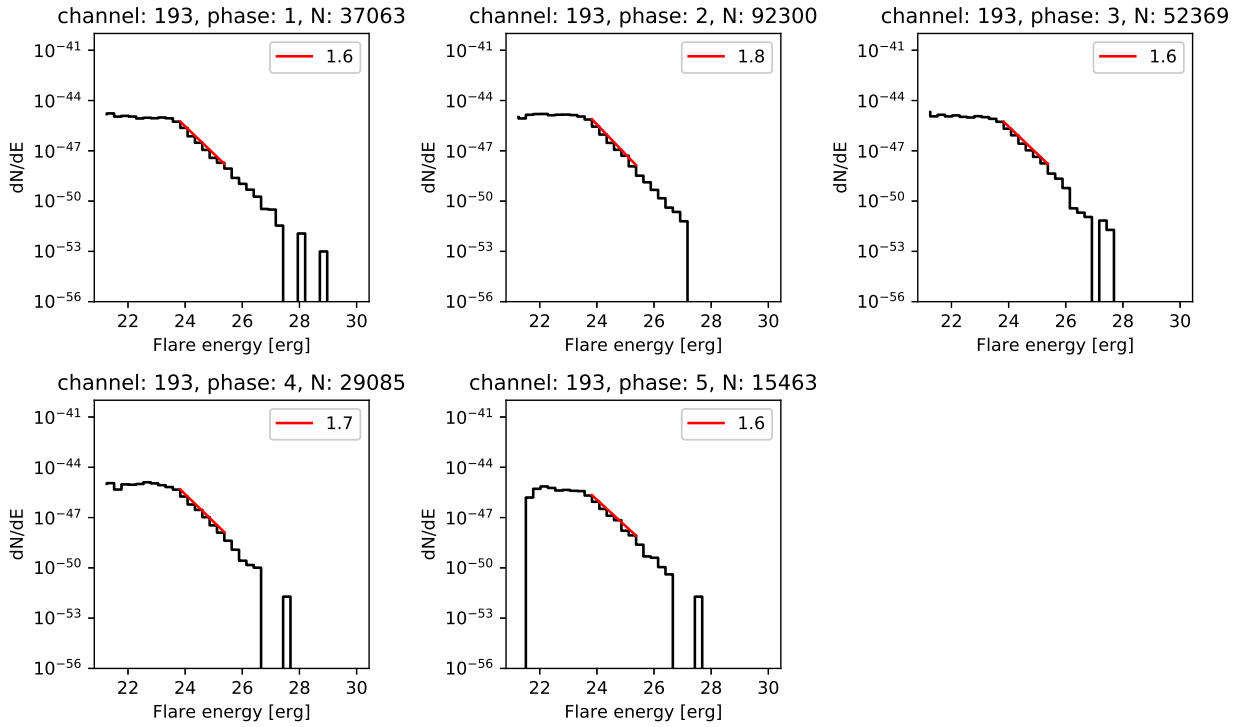

Figure 5.5: Energy distributions of flares detected by SDO/AIA 193 Å of AR 12738 in east limb (top-left), mid-east (top-center), meridian (top-right), mid-west (bottom-left), and west limb (bottom-center).

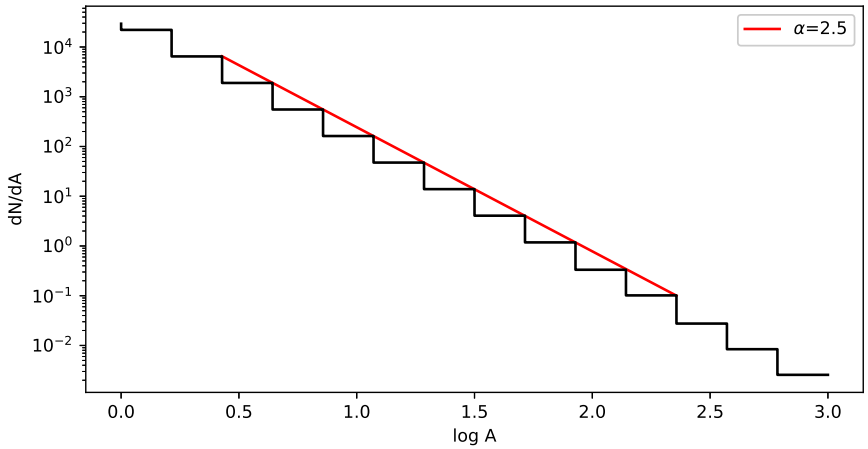

Figure 5.6: Distribution of amplitude of input enhancement. The power-law index is 2.5.

5.3 Dependence of power-law index on event occurrence rate

To decide the plausible coronal heating scenario, it is necessary to investigate the effect of temporally overlapped or missed events on the power-law index as well as spatially overlapped events as discussed in previous section. Therefore, we surveyed the dependence of power-law index on the event occurrence rate using a numerical experiment.

We made a synthetic light curve as an addition of Gaussian functions as following equation:

$$I(t) = \sum_{i}^{N} A_i \exp\left\{-\frac{(t-T_i)^2}{2\tau_i^2}\right\} \tag{5.1}$$

The amplitude A is randomly chosen following the power-law distribution as shown in Figure 5.6. In this study, we chose the distribution of the power-law index $\alpha = 2.5$. Based on the study of Shimizu (1995), the duration of each enhancement τ is defined using the following equation:

$$\log \tau = \frac{1}{3} \log A + 1 \tag{5.2}$$

T is also randomly determined according to uniform distribution between the observation duration (1200s). We generated 1000 synthetic light curves in each cases of $N = 10^{2.0}, 10^{2.5}, ..., 10^{4.5}$. Figure 5.7 shows examples of synthetic light curves for each N. The generated light curve was

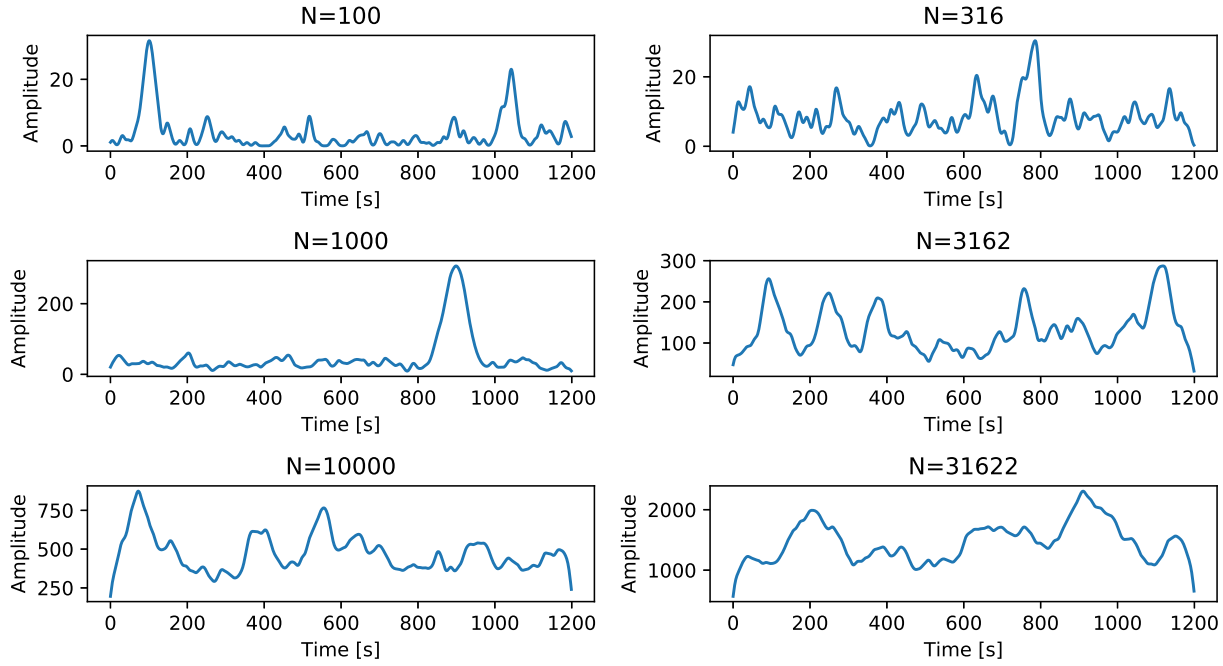

Figure 5.7: Examples of synthetic light curves in case of $N = 10^{2.0}, 10^{2.5}, ..., 10^{4.5}$.

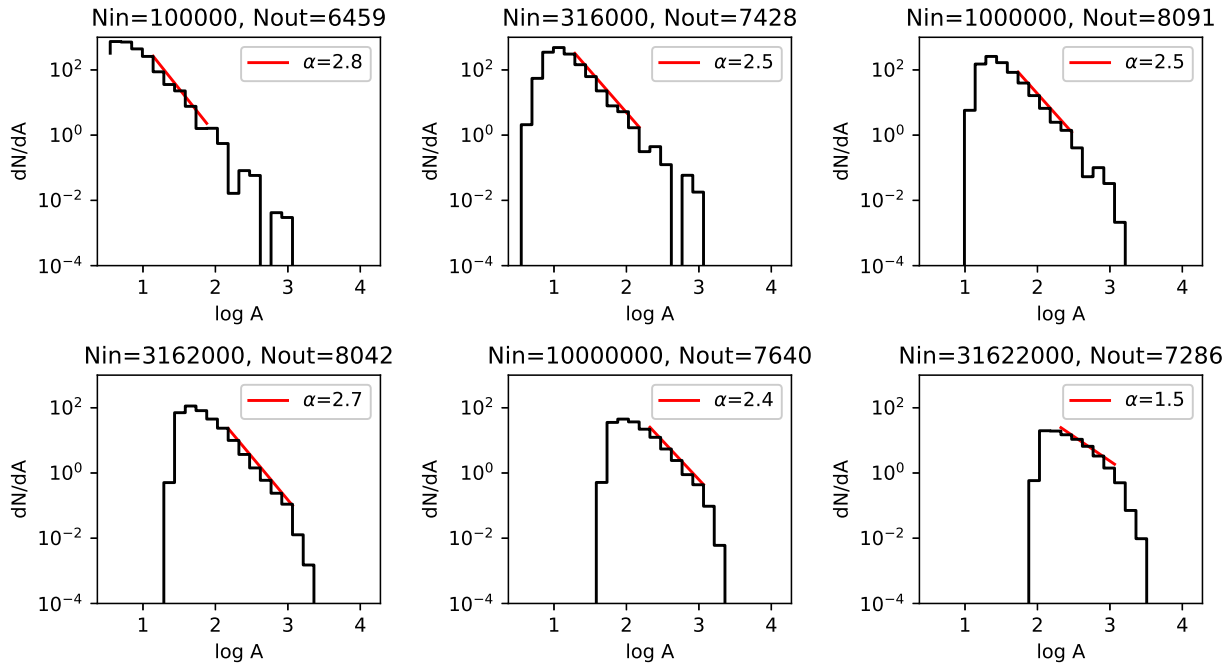

Figure 5.8: Occurrence frequency distributions of detected enhancements from the synthetic light curves in case of $N = 10^{2.0}, 10^{2.5}, ..., 10^{4.5}$. Red lines represent power-law fitted lines. $N_{\rm out}$ indicates the number of detected events.

sampled with 12s cadence as same as the SDO/AIA observation. We applied our detection criterion to synthetic light curves and derive the occurrence frequency distribution.

Figure 5.8 represents occurrence frequency distributions of detected enhancements for each N. Red lines represent power-law fitted lines using same procedure in Chapter 4. $N_{\rm out}$ indicates the number of detected events. As a result, the power-law index is almost consistent except for in case of $N = 10^{4.5}$. When the event occurrence rate is extremely high, the power-law index of detected events becomes smaller, however, its distribution is no longer following a power-law. This deformation of the distribution cannot be seen in actual observation, therefore, this is an unrealistic parameter. Considering this point, the power-law index does not depend on the event occurrence rate. This result also does not support the event overlapping scenario.

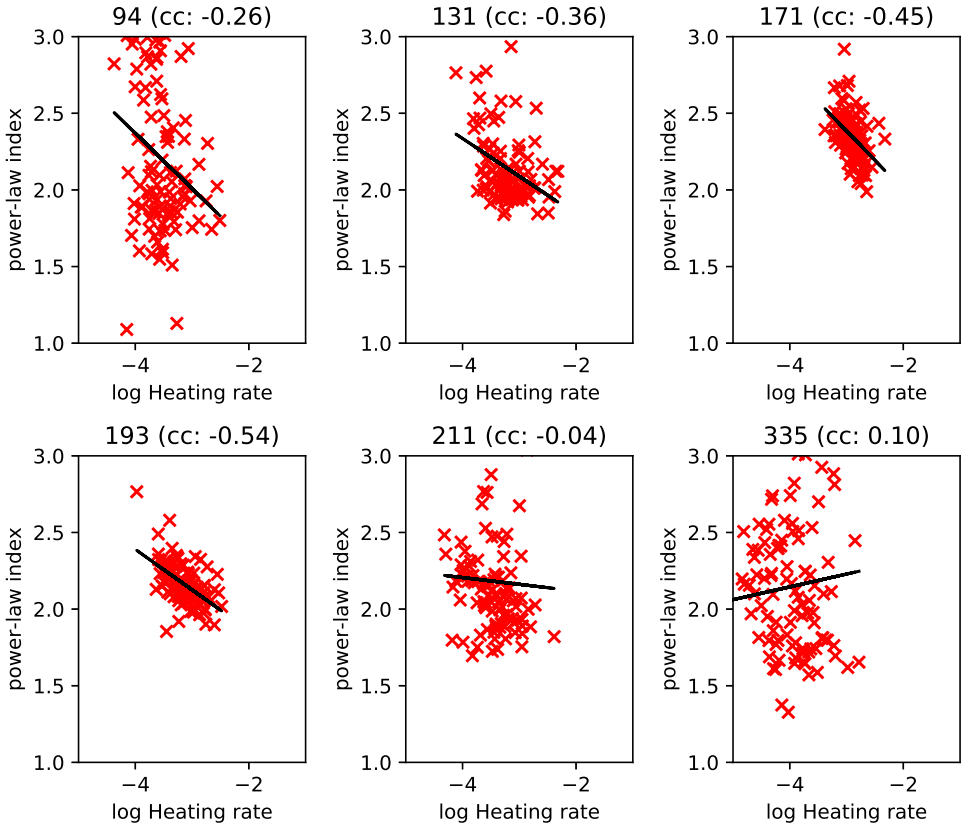

Figure 5.9: Scatter plot of power-law index and heating contribution of impulsive events $F_i/(F_r + F_c)$ to AR heating.

5.4 Contribution to Active Region Heating

We investigated the contribution of impulsive heating events to SHARP ARs studied in Chapter 4 using the results of Chapter 3 and 4. We calculated heating input F_i, radiation F_r, and conductive loss F_c fluxes in each SHARP AR using Equation 3.15, 3.16, and 3.19. The electron density and temperature used to estimated radiation loss were mean values of those estimated by DeepEM code.

Figure 5.9 represents scatter plots of power-law index and heating rate $F_i/(F_r + F_c)$ in each SHARP AR. According to this result, the contribution of impulsive energy releases to AR heating is approximately ranging from 0.01% to 1%. Considering the result that released nonthermal and Doppler motion energy is approximately 0.1–1% and 10–100% of thermal energy, the heating rate of

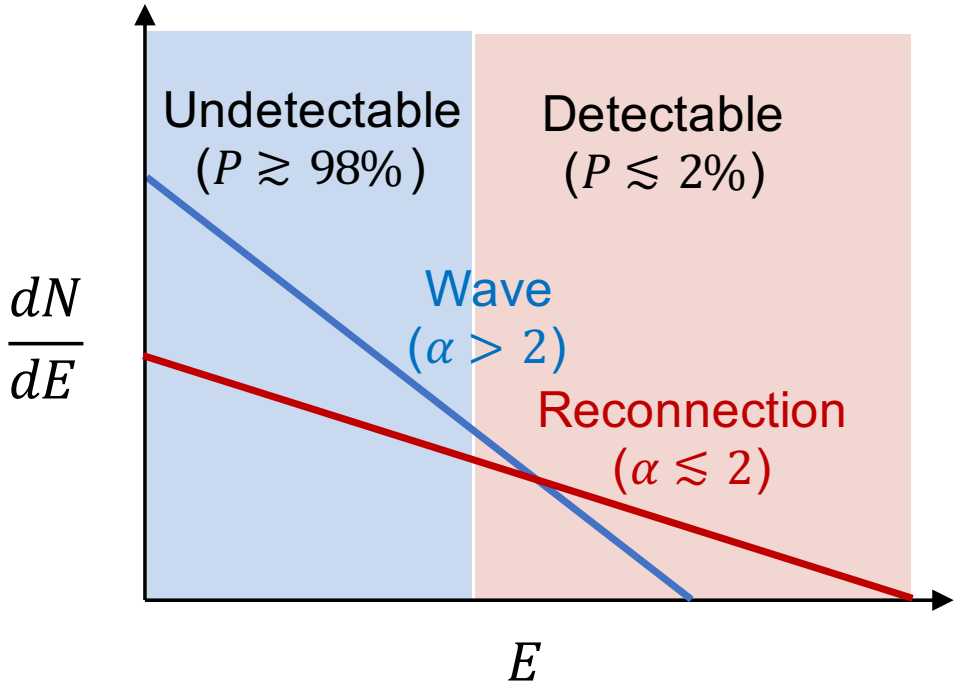

Figure 5.10: Heating scenario based on our hypothesis. The power-law index of energy distribution of magnetic reconnection is smaller than 2 (larger events dominant) whereas the index of waves is greater than 2 (smaller events dominant). According to the SDO/AIA and Hinode/EIS observation, at most 2% of required energy flux is supplied by detectable events, which is mainly composed of energy releases caused by magnetic reconnections. To meet the requirement, the remaining 98% of the heating flux should be mostly provided by waves.

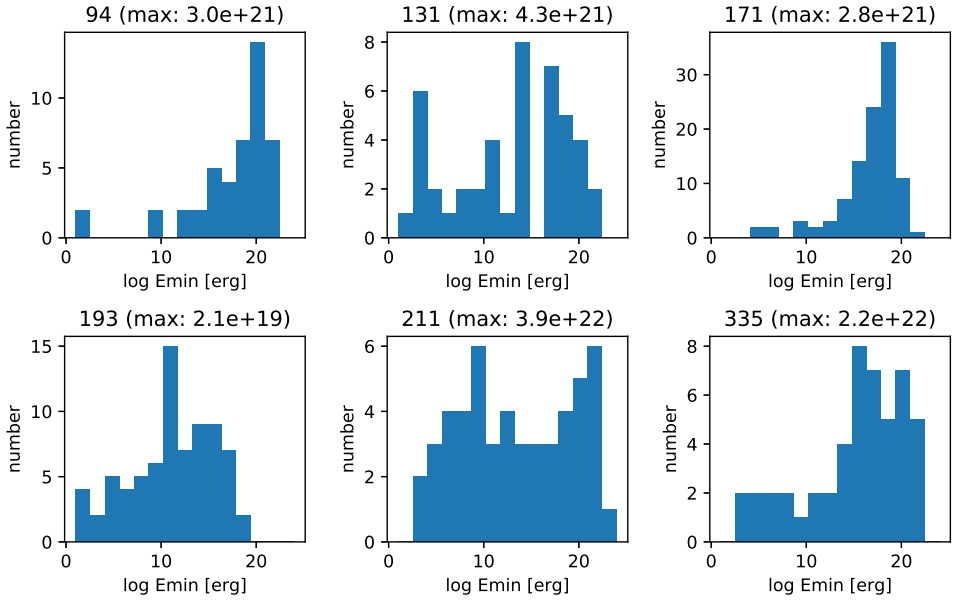

Figure 5.11: Distributions of the required minimum energy of impulsive heating to supply sufficient energy flux to ARs.

detected events is at most 2%. In this figure, there are weak or clear negative correlations between the power-law index and heating rate in some channels. Based on our hypothesis (Figure 4.12), this tendency suggests that the contribution of magnetic reconnections is dominant in ARs which have higher heating rates. However, assuming nanoflare heating model, the remaining 98% of heating flux should be supplied by events could not be detected in this study. In our model, this shortage should be mainly supplied by waves (Figure 5.10).

We calculated how small the energy the power-law index should be maintained to provide sufficient energy flux by nanoflares (waves) for SHARP ARs which have the index greater than 2. The smallest energy can be derived using Equation 1.2, required flux ($F_r + F_c$), and a power-law fitted line for each AR as following equation:

$$E_{\rm min}^{-\alpha+2} = E_{\rm max}^{-\alpha+2} - \frac{-\alpha+2}{A}(F_r + F_c) \tag{5.3}$$

where, $E_{\rm max}$ is the maximum energy in the fitting range. Figure 5.11 represents the distribution of $E_{\rm min}$ of ARs calculate using the result of each SDO/AIA channel. The power-law distribution should be maintained at least 10^{19} – 10^{22} erg to provide the sufficient energy. The existence of such

"picoflares" has been suggested for a few decades (*e.g.,* Katsukawa, 2003). Ramesh et al. (2021) reported the power-law behavior of peak flux density of type I radio bursts whose estimated energy is approximately 10^{21} erg. The derived power-law index is in the range 2.2 to 2.7. Though that index is not for energy but for peak flux density, this result might support the continuity of the power-law distribution of impulsive heating to the derived $E_{\rm min}$.

Chapter 6

Conclusion

In this thesis, we derived the power-law index of an occurrence frequency distribution of solar flares in various ways, which is one of the most important indicators for nanoflare coronal heating (if the index is greater than 2, smaller events are dominant in energy supply). Most of previous studies suggested that the power-law indices in ARs are smaller than 2, whereas that of the QS is not. In contrast, our results suggest that not only the power-law index of the QS but also those in some ARs are greater than 2, which supports the nanoflare heating model.

In Chapter 2, we derived the power-law index of an AR considering the loops and events overlapped in the line-of-sight direction by using a 1D simulation and GA. We have shown that the loops are intermittently heated by nanoflares and the volume that is heated by flares is much smaller than the observational resolution especially in hotter plasma and outer region. These results suggest that the power-law index of previous studies which do not taking into account the overlapped and unresolved events might be underestimated due to missing small events and totaling energy of multiple events.

In Chapter 3, we statistically analyzed an energy conversion rate of an AR transient brightening using Hinode/EIS spectroscopic observations. We concluded that the Doppler motion and nonthermal energy of detected events are approximately 0.1 – 1% and 10 – 100% of the change of thermal energy, respectively. As well, the contributions of Doppler motion and nonthermal energy fluxes to the AR heating is roughly 1% and 10% of that of the thermal energy flux. The power-law indices of occurrence frequency distributions as functions of Doppler motion and nonthermal energy do not exceed 2 as well as that of thermal energy. These results suggest that it might be sufficient to examine only the contribution of thermal energy when investigating the validity of the nanoflare

heating model. However, the time scale of detected brightenings is roughly ranging from several seconds to a few minutes, whereas the cadence of the used EIS data is 254 s. Therefore, the similar analysis should be executed using the next Japanese satellite mission, Solar-C/EUVST which will achieve ten times higher temporal resolution, after its launch (mid-2020s).

In Chapter 4, we investigated the dependence of the index on the solar activity, coronal features, released energy range, and active region properties. Our findings are (1) Power-law index in each year derived by Sun-as-a-star observation has a negative correlation with sunspot number. (2) Power-law index in AR is smaller than that of the QS and CHs. (3) Power-law index is almost constant in the energy range of $10^{24} \lesssim E \lesssim 10^{30}$ erg. (4) ARs which have more magnetic free energy density, unsigned magnetic flux, and shear angle tend to have smaller power-law indices. From the results, we suggest two scenarios. The first one is that the physical process of the heating is different between QS and ARs. According to Antolin et al. (2008), power-law index of wave-heated corona is greater than that of nanoflare heating. Based on this study, our result suggest that ARs are more heated by magnetic reconnections whereas the QS is mainly heated by Alfvén waves. Moreover, the ratio of reconnection and wave heating depends on the magnetic properties even among ARs (Figure 4.12). In QS, the distribution of waves is standing out due to the lack of reconnections, then, the total power-law index can be large. On the other hand, in active ARs, the distribution of waves is hidden by that of reconnections, then, the total power-law index becomes small. In addition, this bent in the distribution (steeper in lower energy range) can be seen the result of EIS spectroscopic observation (Figure 3.7).

The another scenario is that the "apparent" index is different but the "actual" index is the same regardless the activity, which implies that the energy release process is consistent even in an AR and QS. Even if the "actual" index is consistent, the "apparent" index might be underestimated due to the overlapping of the events in the direction of the line-of-sight and missing of the smaller events. These underestimation should increase as the event occurrence rate and volume of each event increase. Therefore, it is reasonable to assume that these overlapping and missing increase in Active ARs and the power-law index is underestimated. As described in Chapter 2, there are multiple coronal loops smaller than the spatial resolution of current satellite. Also, multiple events should be overlapped in the line-of-sight direction, which causes underestimation of the power-law index. However, in Chapter 4, the power-law index derived using Sun-as-a-star observation and macro-pixel method are almost same. Therefore, the spatial overlap of events may not change the power-law index. In addition, we revealed that there are no effect of center-to-limb variation on the power-law index. Moreover, we showed that temporally overlapped and missed events do not have effect on the power-law index. These results suggests that the latter scenario may not be plausible.

We also investigated contributions of impulsive heating to the AR heating using 108 SHARP ARs. Even considering the contribution of nonthermal and Doppler motion energy fluxes, the heating flux is at most 2% of radiation and conductive loss fluxes. Based on our heating scenario, the remaining 98% of heating flux should be mainly supplied by waves which are undetectable by current observation equipments (Figure 5.10). To provide sufficient energy, the power-law distribution should be maintained at least 10^{19} – 10^{22} erg with the index greater than 2.

The occurrence frequency distributions derived by the new method introduced in Chapter 2 and by the observational studies in Chapter 3 and 4 are different (Higher energy range of the distribution in Chapter 2 has steeper distribution whereas those in Chapter 3 and 4 has flatter one.) One of the causes of this difference may be the way of the optimization in the GA. Because we used correlation coefficient between synthetic and observed light curves for the evaluation, its large trend should be reproduced as priority as shown in Figure 2.10. In contrast, the small spikes can be detected well in our observational studies as shown in Figure 4.1. Therefore, the contribution of smaller flares is possibly underestimated in the GA study. But we have to notice that the distribution derived by the GA has consistencies with some simulation studies such as Bingert & Peter (2013) and Kanella & Gudiksen (2018).

Although the GA method we developed may not be perfect yet, this method has other strengths. The first one is that the estimation of released energy seems to be more valid than that of other studies (*e.g.*, change in thermal energy). In addition, It is probably able to consider the effect of NEI on the detection and energy estimation by including ionization and recombination process to the simulation. As far as we know, there are no observational studies which tried to derive the occurrence frequency distribution of flares with taking into account the NEI effect. Therefore, it is worth applying our new method to various ARs to investigate the accurate power-law indices. However, automated detection and tracking of coronal loops are technically difficult and computationally heavy (Aschwanden et al., 2013a, Aschwanden, 2010). Moreover, due to the variety of free parameters, it is necessary to carry out parameter survey. Overcoming these difficulties will contribute to an elucidation of the mechanism of the coronal heating in the future.

References

Adithya, H. N., Kariyappa, R., Shinsuke, I., Kanya, K., Zender, J., Damé, L., Gabriel, G., DeLuca, E., & Weber, M. (2021). Solar Soft X-ray Irradiance Variability, I: Segmentation of Hinode/XRT Full-Disk Images and Comparison with GOES (1 - 8 Å) X-Ray Flux. *SoPh*, *296*(4), 71.

Allred, J. C., Kowalski, A. F., & Carlsson, M. (2015). A Unified Computational Model for Solar and Stellar Flares. *ApJ*, *809*(1), 104.

Antolin, P., & Shibata, K. (2010). The Role Of Torsional Alfvén Waves in Coronal Heating. *ApJ*, *712*(1), 494–510.

Antolin, P., Shibata, K., Kudoh, T., Shiota, D., & Brooks, D. (2008). Predicting Observational Signatures of Coronal Heating by Alfvén Waves and Nanoflares. *ApJ*, *688*(1), 669–682.

Aschwanden, M., De Pontieu, B., & Katrukha, E. (2013a). Optimization of Curvilinear Tracing Applied to Solar Physics and Biophysics. *Entropy*, *15*(8), 3007–3030.

Aschwanden, M. J. (2010). A Code for Automated Tracing of Coronal Loops Approaching Visual Perception. *SoPh*, *262*(2), 399–423.

Aschwanden, M. J., Boerner, P., Ryan, D., Caspi, A., McTiernan, J. M., & Warren, H. P. (2015). Global Energetics of Solar Flares: II. Thermal Energies. *ApJ*, *802*(1), 53.

Aschwanden, M. J., Boerner, P., Schrijver, C. J., & Malanushenko, A. (2013b). Automated Temperature and Emission Measure Analysis of Coronal Loops and Active Regions Observed with the Atmospheric Imaging Assembly on the Solar Dynamics Observatory (SDO/AIA). *SoPh*, *283*(1), 5–30.

Aschwanden, M. J., & Dudok de Wit, T. (2021). Correlation of the Sunspot Number and the Waiting-time Distribution of Solar Flares, Coronal Mass Ejections, and Solar Wind Switchback Events Observed with the Parker Solar Probe. *ApJ*, *912*(2), 94.

Aschwanden, M. J., & Güdel, M. (2021). Self-organized Criticality in Stellar Flares. *ApJ*, *910*(1), 41.

Aschwanden, M. J., Tarbell, T. D., Nightingale, R. W., Schrijver, C. J., Title, A., Kankelborg, C. C., Martens, P., & Warren, H. P. (2000). Time Variability of the "Quiet" Sun Observed with TRACE. II. Physical Parameters, Temperature Evolution, and Energetics of Extreme-Ultraviolet Nanoflares. *ApJ*, *535*(2), 1047–1065.

Benz, A. O., & Krucker, S. (2002). Energy Distribution of Microevents in the Quiet Solar Corona. *ApJ*, *568*(1), 413–421.

Berghmans, D., Clette, F., & Moses, D. (1998). Quiet Sun EUV transient brightenings and turbulence. A panoramic view by EIT on board SOHO. *A&A*, *336*, 1039–1055.

Bingert, S., & Peter, H. (2013). Nanoflare statistics in an active region 3D MHD coronal model. *A&A*, *550*, A30.

Bobra, M. G., Sun, X., Hoeksema, J. T., Turmon, M., Liu, Y., Hayashi, K., Barnes, G., & Leka, K. D. (2014). The Helioseismic and Magnetic Imager (HMI) Vector Magnetic Field Pipeline: SHARPs - Space-Weather HMI Active Region Patches. *SoPh*, *289*(9), 3549–3578.

Boerner, P., Edwards, C., Lemen, J., Rausch, A., Schrijver, C., Shine, R., Shing, L., Stern, R., Tarbell, T., Title, A., Wolfson, C. J., Soufli, R., Spiller, E., Gullikson, E., McKenzie, D., Windt, D., Golub, L., Podgorski, W., Testa, P., & Weber, M. (2012). Initial calibration of the atmospheric imaging assembly (aia) on the solar dynamics observatory (sdo). *Solar Physics*, *275*(1), 41–66. URL `https://doi.org/10.1007/s11207-011-9804-8`

Botha, G. J. J., Arber, T. D., & Hood, A. W. (2011). Thermal conduction effects on the kink instability in coronal loops. *A&A*, *525*, A96.

Bowness, R., Hood, A. W., & Parnell, C. E. (2013). Coronal heating and nanoflares: current sheet formation and heating. *A&A*, *560*, A89.

Bradshaw, S. J., & Cargill, P. J. (2010). The Cooling of Coronal Plasmas. III. Enthalpy Transfer as a Mechanism for Energy Loss. *ApJ*, *717*(1), 163–174.

Bradshaw, S. J., & Klimchuk, J. A. (2011). What Dominates the Coronal Emission Spectrum During the Cycle of Impulsive Heating and Cooling? *ApJS*, *194*(2), 26.

Brooks, D. H., & Warren, H. P. (2016). Measurements of Non-thermal Line Widths in Solar Active Regions. *ApJ*, *820*(1), 63.

Cargill, P. J. (1994). Some Implications of the Nanoflare Concept. *ApJ*, *422*, 381.

Cargill, P. J., Bradshaw, S. J., & Klimchuk, J. A. (2012). Enthalpy-based Thermal Evolution of Loops. II. Improvements to the Model. *ApJ*, *752*(2), 161.

Carmichael, H. (1964). *A Process for Flares*, vol. 50, (p. 451).

Carrington, R. C. (1859). Description of a Singular Appearance seen in the Sun on September 1, 1859. *Mon. Notices Royal Astron. Soc.*, *20*, 13–15.

Cheung, M. C. M., Boerner, P., Schrijver, C. J., Testa, P., Chen, F., Peter, H., & Malanushenko, A. (2015). Thermal Diagnostics with the Atmospheric Imaging Assembly on board the Solar Dynamics Observatory: A Validated Method for Differential Emission Measure Inversions. *ApJ*, *807*(2), 143.

Christe, S., Glesener, L., Buitrago-Casas, C., Ishikawa, S.-N., Ramsey, B., Gubarev, M., Kilaru, K., Kolodziejczak, J. J., Watanabe, S., Takahashi, T., Tajima, H., Turin, P., Shourt, V., Foster, N., & Krucker, S. (2016). FOXSI-2: Upgrades of the Focusing Optics X-ray Solar Imager for its Second Flight. *Journal of Astronomical Instrumentation*, *5*(1), 1640005–625.

Collura, A., Pasquini, L., & Schmitt, J. H. M. M. (1988). Time variability in the X-ray emission of dM stars observed by EXOSAT. *A&A*, *205*, 197–206.

Culhane, J. L., Harra, L. K., James, A. M., Al-Janabi, K., Bradley, L. J., Chaudry, R. A., Rees, K., Tandy, J. A., Thomas, P., & Whillock, M. C. R. (2007). The EUV Imaging Spectrometer for Hinode. *SoPh*, *243*(1), 19–61.

Datlowe, D. W., Elcan, M. J., & Hudson, H. S. (1974). OSO-7 observations of solar x-rays in the energy range 10 100 keV. *SoPh*, *39*(1), 155–174.

De Pontieu, B., Title, A. M., Lemen, J. R., Kushner, G. D., Akin, D. J., Allard, B., Berger, T., Boerner, P., Cheung, M., Chou, C., Drake, J. F., Duncan, D. W., Freeland, S., Heyman, G. F., Hoffman, C., Hurlburt, N. E., Lindgren, R. W., Mathur, D., Rehse, R., Sabolish, D., Seguin, R., Schrijver, C. J., Tarbell, T. D., Wülser, J. P., Wolfson, C. J., Yanari, C., Mudge, J., Nguyen-Phuc, N., Timmons, R., van Bezooijen, R., Weingrod, I., Brookner, R., Butcher, G., Dougherty, B., Eder, J., Knagenhjelm, V., Larsen, S., Mansir, D., Phan, L., Boyle, P., Cheimets, P. N., DeLuca, E. E., Golub, L., Gates, R., Hertz, E., McKillop, S., Park, S., Perry, T., Podgorski, W. A., Reeves, K., Saar, S., Testa, P., Tian, H., Weber, M., Dunn, C., Eccles, S., Jaeggli, S. A., Kankelborg, C. C., Mashburn, K., Pust, N., Springer, L., Carvalho, R., Kleint, L., Marmie, J., Mazmanian, E., Pereira, T. M. D., Sawyer, S., Strong, J., Worden, S. P., Carlsson, M., Hansteen,

V. H., Leenaarts, J., Wiesmann, M., Aloise, J., Chu, K. C., Bush, R. I., Scherrer, P. H., Brekke, P., Martinez-Sykora, J., Lites, B. W., McIntosh, S. W., Uitenbroek, H., Okamoto, T. J., Gummin, M. A., Auker, G., Jerram, P., Pool, P., & Waltham, N. (2014). The Interface Region Imaging Spectrograph (IRIS). *SoPh*, *289*(7), 2733–2779.

Dennis, B. R. (1985). Solar Hard X-Ray Bursts. *SoPh*, *100*, 465.

Dere, K. P., Del Zanna, G., Young, P. R., Landi, E., & Sutherland, R. S. (2019). CHIANTI—An Atomic Database for Emission Lines. XV. Version 9, Improvements for the X-Ray Satellite Lines. *ApJS*, *241*(2), 22.

Drake, J. F. (1971). Characteristics of Soft Solar X-Ray Bursts. *SoPh*, *16*(1), 152–185.

Freeland, S. L., & Handy, B. N. (1998). Data Analysis with the SolarSoft System. *SoPh*, *182*(2), 497–500.

Fursyak, Y. A. (2018). Vertical Electric Currents in Active Regions: Calculation Methods and Relation to the Flare Index. *Geomagnetism and Aeronomy*, *58*(8), 1129–1135.

Handy, B. N., Acton, L. W., Kankelborg, C. C., Wolfson, C. J., Akin, D. J., Bruner, M. E., Caravalho, R., Catura, R. C., Chevalier, R., Duncan, D. W., Edwards, C. G., Feinstein, C. N., Freeland, S. L., Friedlaender, F. M., Hoffmann, C. H., Hurlburt, N. E., Jurcevich, B. K., Katz, N. L., Kelly, G. A., Lemen, J. R., Levay, M., Lindgren, R. W., Mathur, D. P., Meyer, S. B., Morrison, S. J., Morrison, M. D., Nightingale, R. W., Pope, T. P., Rehse, R. A., Schrijver, C. J., Shine, R. A., Shing, L., Strong, K. T., Tarbell, T. D., Title, A. M., Torgerson, D. D., Golub, L., Bookbinder, J. A., Caldwell, D., Cheimets, P. N., Davis, W. N., Deluca, E. E., McMullen, R. A., Warren, H. P., Amato, D., Fisher, R., Maldonado, H., & Parkinson, C. (1999). The transition region and coronal explorer. *SoPh*, *187*(2), 229–260.

Hannah, I. G., Christe, S., Krucker, S., Hurford, G. J., Hudson, H. S., & Lin, R. P. (2008). RHESSI Microflare Statistics. II. X-Ray Imaging, Spectroscopy, and Energy Distributions. *ApJ*, *677*(1), 704–718.

Hara, H., Watanabe, T., Harra, L. K., Culhane, J. L., & Young, P. R. (2011). Plasma Motions and Heating by Magnetic Reconnection in a 2007 May 19 Flare. *ApJ*, *741*(2), 107.

Hazra, S., Sardar, G., & Chowdhury, P. (2020). Distinguishing between flaring and nonflaring active regions. *A&A*, *639*, A44.

Hirayama, T. (1974). Theoretical Model of Flares and Prominences. I: Evaporating Flare Model. *SoPh*, *34*(2), 323–338.

Hori, K., Yokoyama, T., Kosugi, T., & Shibata, K. (1997). Pseudo-Two-dimensional Hydrodynamic Modeling of Solar Flare Loops. *ApJ*, *489*(1), 426–441.

Hudson, H. S. (1991). Solar flares, microflares, nanoflares, and coronal heating. *SoPh*, *133*(2), 357–369.

Imada, S., Aoki, K., Hara, H., Watanabe, T., Harra, L. K., & Shimizu, T. (2013). Evidence for Hot Fast Flow above a Solar Flare Arcade. *ApJL*, *776*(1), L11.

Imada, S., Bamba, Y., & Kusano, K. (2014). Coronal behavior before the large flare onset. *PASJ*, *66*, S17.

Imada, S., Hara, H., & Watanabe, T. (2009). Ion Temperature and Non-Thermal Velocity in a Solar Active Region: Using Emission Lines of Different Atomic Species. *ApJL*, *705*(2), L208–L212.

Imada, S., Hara, H., Watanabe, T., Kamio, S., Asai, A., Matsuzaki, K., Harra, L. K., & Mariska, J. T. (2007). Discovery of a Temperature-Dependent Upflow in the Plage Region During a Gradual Phase of the X-Class Flare. *PASJ*, *59*, S793.

Imada, S., Hara, H., Watanabe, T., Murakami, I., Harra, L. K., Shimizu, T., & Zweibel, E. G. (2011a). One-dimensional Modeling for Temperature-dependent Upflow in the Dimming Region Observed by Hinode/EUV Imaging Spectrometer. *ApJ*, *743*(1), 57.

Imada, S., Murakami, I., & Watanabe, T. (2015). Observation and numerical modeling of chromospheric evaporation during the impulsive phase of a solar flare. *Physics of Plasmas*, *22*(10), 101206.

Imada, S., Murakami, I., Watanabe, T., Hara, H., & Shimizu, T. (2011b). Magnetic Reconnection in Non-equilibrium Ionization Plasma. *ApJ*, *742*(2), 70.

Imada, S., & Zweibel, E. G. (2012). Self-organization of Reconnecting Plasmas to Marginal Collisionality in the Solar Corona. *ApJ*, *755*(2), 93.

Innes, D. E., McKenzie, D. E., & Wang, T. (2003). Observations of 1000 km s^{-1} Doppler shifts in 10^7 K solar flare supra-arcade. *SoPh*, *217*(2), 267–279.

Ishikawa, S., Glesener, L., Krucker, S., Christe, S., Buitrago-Casas, J. C., Narukage, N., & Vievering, J. (2017). Detection of nanoflare-heated plasma in the solar corona by the FOXSI-2 sounding rocket. *Nature Astronomy*, *1*, 771–774.

Jess, D. B., Dillon, C. J., Kirk, M. S., Reale, F., Mathioudakis, M., Grant, S. D. T., Christian, D. J., Keys, P. H., Krishna Prasad, S., & Houston, S. J. (2019). Statistical Signatures of Nanoflare Activity. I. Monte Carlo Simulations and Parameter-space Exploration. *ApJ*, *871*(2), 133.

Kamio, S., Hara, H., Watanabe, T., Fredvik, T., & Hansteen, V. H. (2010). Modeling of EIS Spectrum Drift from Instrumental Temperatures. *SoPh*, *266*(1), 209–223.

Kanella, C., & Gudiksen, B. V. (2018). Investigating 4D coronal heating events in magnetohydrodynamic simulations. *A&A*, *617*, A50.

Kashyap, V. L., Drake, J. J., Güdel, M., & Audard, M. (2002). Flare Heating in Stellar Coronae. *ApJ*, *580*(2), 1118–1132.

Katsukawa, Y. (2003). Spatial and Temporal Extent of Solar Nanoflares and Their Energy Range. *PASJ*, *55*, 1025–1031.

Kawai, T., & Imada, S. (2021a). Energy Distribution of Small-scale Flares Derived Using a Genetic Algorithm. *ApJ*, *906*(1), 2.

Kawai, T., & Imada, S. (2021b). The Energy Conversion Rate of an Active Region Transient Brightening Estimated by Hinode Spectroscopic Observations. *ApJ*, *918*(2), 51.

Kawai, T., Imada, S., Nishimoto, S., Watanabe, K., & Kawate, T. (2020). Nowcast of an EUV dynamic spectrum during solar flares. *Journal of Atmospheric and Solar-Terrestrial Physics*, *205*, 105302.

Kawai, T., Kanda, N., & Imada, S. (2019). Velocity Structure and Temperature Dependence of an Extreme-Ultraviolet Jet Observed by Hinode. *SoPh*, *294*(6), 74.

Klimchuk, J. A. (2006). On Solving the Coronal Heating Problem. *SoPh*, *234*(1), 41–77.

Klimchuk, J. A. (2015). Key aspects of coronal heating. *Philosophical Transactions of the Royal Society of London Series A*, *373*(2042), 20140256–20140256.

Klimchuk, J. A., Patsourakos, S., & Cargill, P. J. (2008). Highly Efficient Modeling of Dynamic Coronal Loops. *ApJ*, *682*(2), 1351–1362.

Kobayashi, K., Cirtain, J., Winebarger, A. R., Korreck, K., Golub, L., Walsh, R. W., De Pontieu, B., DeForest, C., Title, A., Kuzin, S., Savage, S., Beabout, D., Beabout, B., Podgorski, W., Caldwell, D., McCracken, K., Ordway, M., Bergner, H., Gates, R., McKillop, S., Cheimets, P., Platt, S., Mitchell, N., & Windt, D. (2014). The High-Resolution Coronal Imager (Hi-C). *SoPh*, *289*(11), 4393–4412.

Koch, D. G., Borucki, W. J., Basri, G., Batalha, N. M., Brown, T. M., Caldwell, D., Christensen-Dalsgaard, J., Cochran, W. D., DeVore, E., Dunham, E. W., Gautier, I., Thomas N., Geary, J. C., Gilliland, R. L., Gould, A., Jenkins, J., Kondo, Y., Latham, D. W., Lissauer, J. J., Marcy, G., Monet, D., Sasselov, D., Boss, A., Brownlee, D., Caldwell, J., Dupree, A. K., Howell, S. B., Kjeldsen, H., Meibom, S., Morrison, D., Owen, T., Reitsema, H., Tarter, J., Bryson, S. T., Dotson, J. L., Gazis, P., Haas, M. R., Kolodziejczak, J., Rowe, J. F., Van Cleve, J. E., Allen, C., Chandrasekaran, H., Clarke, B. D., Li, J., Quintana, E. V., Tenenbaum, P., Twicken, J. D., & Wu, H. (2010). Kepler Mission Design, Realized Photometric Performance, and Early Science. *ApJL*, *713*(2), L79–L86.

Kopp, R. A., & Pneuman, G. W. (1976). Magnetic reconnection in the corona and the loop prominence phenomenon. *SoPh*, *50*(1), 85–98.

Korendyke, C. M., Brown, C. M., Thomas, R. J., Keyser, C., Davila, J., Hagood, R., Hara, H., Heidemann, K., James, A. M., Lang, J., Mariska, J. T., Moser, J., Moye, R., Myers, S., Probyn, B. J., Seely, J. F., Shea, J., Shepler, E., & Tandy, J. (2006). Optics and mechanisms for the extreme-ultraviolet imaging spectrometer on the solar-b satellite. *Appl. Opt.*, *45*(34), 8674–8688. URL `http://ao.osa.org/abstract.cfm?URI=ao-45-34-8674`

Kosugi, T., Matsuzaki, K., Sakao, T., Shimizu, T., Sone, Y., Tachikawa, S., Hashimoto, T., Minesugi, K., Ohnishi, A., Yamada, T., Tsuneta, S., Hara, H., Ichimoto, K., Suematsu, Y., Shimojo, M., Watanabe, T., Shimada, S., Davis, J. M., Hill, L. D., Owens, J. K., Title, A. M., Culhane, J. L., Harra, L. K., Doschek, G. A., & Golub, L. (2007). The Hinode (Solar-B) Mission: An Overview. *SoPh*, *243*(1), 3–17.

Lean, J. (1997). The Sun's Variable Radiation and Its Relevance For Earth. *ARA&A*, *35*, 33–67.

Lemen, J. R., Title, A. M., Akin, D. J., Boerner, P. F., Chou, C., Drake, J. F., Duncan, D. W., Edwards, C. G., Friedlaender, F. M., & Heyman, G. F. (2012). The Atmospheric Imaging Assembly (AIA) on the Solar Dynamics Observatory (SDO). *SoPh*, *275*(1-2), 17–40.

Lin, R. P., Schwartz, R. A., Kane, S. R., Pelling, R. M., & Hurley, K. C. (1984). Solar hard X-ray microflares. *ApJ*, *283*, 421–425.

Liu, W., Chen, Q., & Petrosian, V. (2013). Plasmoid Ejections and Loop Contractions in an Eruptive M7.7 Solar Flare: Evidence of Particle Acceleration and Heating in Magnetic Reconnection Outflows. *ApJ*, *767*(2), 168.

Maehara, H., Shibayama, T., Notsu, S., Notsu, Y., Nagao, T., Kusaba, S., Honda, S., Nogami, D., & Shibata, K. (2012). Superflares on solar-type stars. *Nature*, *485*(7399), 478–481.

Masuda, S., Kosugi, T., Hara, H., Tsuneta, S., & Ogawara, Y. (1994). A loop-top hard X-ray source in a compact solar flare as evidence for magnetic reconnection. *Nature*, *371*(6497), 495–497.

Matsui, Y., Yokoyama, T., Kitagawa, N., & Imada, S. (2012). Multi-wavelength Spectroscopic Observation of Extreme-ultraviolet Jet in AR 10960. *ApJ*, *759*(1), 15.

McKenzie, D. E., & Hudson, H. S. (1999). X-Ray Observations of Motions and Structure above a Solar Flare Arcade. *ApJL*, *519*(1), L93–L96.

Mumford, S., Freij, N., Christe, S., Ireland, J., Mayer, F., Hughitt, V., Shih, A., Ryan, D., Liedtke, S., Pérez-Suárez, D., Chakraborty, P., K, V., Inglis, A., Pattnaik, P., Sipőcz, B., Sharma, R., Leonard, A., Stansby, D., Hewett, R., Hamilton, A., Hayes, L., Panda, A., Earnshaw, M., Choudhary, N., Kumar, A., Chanda, P., Haque, M., Kirk, M., Mueller, M., Konge, S., Srivastava, R., Jain, Y., Bennett, S., Baruah, A., Barnes, W., Charlton, M., Maloney, S., Chorley, N., Himanshu, Modi, S., Mason, J., Naman, Campos Rozo, J. I., Manley, L., Chatterjee, A., Evans, J., Malocha, M., Bobra, M., Ghosh, S., Airmansmith, Stańczak, D., De Visscher, R., Verma, S., Agrawal, A., Buddhika, D., Sharma, S., Park, J., Bates, M., Goel, D., Taylor, G., Cetusic, G., Jacob, Inchaurrandieta, M., Dacie, S., Dubey, S., Sharma, D., Bray, E., Rideout, J., Zahniy, S., Meszaros, T., Bose, A., Chicrala, A., Ankit, Guennou, C., D'Avella, D., Williams, D., Ballew, J., Murphy, N., Lodha, P., Robitaille, T., Krishan, Y., Hill, A., Eigenbrot, A., Mampaey, B., Wiedemann, B., Molina, C., Keşkek, D., Habib, I., Letts, J., Bazán, J., Arbolante, Q., Gomillion, R., Kothari, Y., Sharma, Y., Stevens, A., Price-Whelan, A., Mehrotra, A., Kustov, A., Stone, B., Dang, T., Arias, E., Dover, F., Verstringe, F., Kumar, G., Mathur, H., Babuschkin, I., Wimbish, J., Buitrago-Casas, J., Krishna, K., Hiware, K., Mangaonkar, M., Mendero, M., Schoentgen, M., Gyenge, N., Streicher, O., Mekala, R., Mishra, R., Srikanth, S., Jain, S., Yadav, T., Wilkinson, T., Pereira, T., Agrawal, Y., Jamescalixto, Yasintoda, & Murray, S. (2020). SunPy: A Python package for Solar Physics. *The Journal of Open Source Software*, *5*(46), 1832.

Ogawara, Y., Takano, T., Kato, T., Kosugi, T., Tsuneta, S., Watanabe, T., Kondo, I., & Uchida, Y. (1991). The SOLAR-A Mission - An Overview. *SoPh*, *136*(1), 1–16.

Ohyama, M., & Shibata, K. (1998). X-Ray Plasma Ejection Associated with an Impulsive Flare on 1992 October 5: Physical Conditions of X-Ray Plasma Ejection. *ApJ*, *499*(2), 934–944.

Orlando, S., Bocchino, F., & Peres, G. (1999). Non-equilibrium ionization and the interpretation of Yohkoh/SXT data during solar dynamic events. *A&A*, *346*, 1003–1008.

Parker, E. N. (1983). Magnetic neutral sheets in evolving fields. I - General theory. *ApJ*, *264*, 635–647.

Parker, E. N. (1988). Nanoflares and the Solar X-Ray Corona. *ApJ*, *330*, 474.

Parker, E. N. (1989). Solar and Stellar Magnetic Fields and Atmospheric Structures - Theory. *SoPh*, *121*(1-2), 271–288.

Parnell, C. E., & Jupp, P. E. (2000). Statistical Analysis of the Energy Distribution of Nanoflares in the Quiet Sun. *ApJ*, *529*(1), 554–569.

Pesnell, W. D., Thompson, B. J., & Chamberlin, P. C. (2012). The Solar Dynamics Observatory (SDO). *SoPh*, *275*, 3–15.

Peter, H., Bingert, S., Klimchuk, J. A., de Forest, C., Cirtain, J. W., Golub, L., Winebarger, A. R., Kobayashi, K., & Korreck, K. E. (2013). Structure of solar coronal loops: from miniature to large-scale. *A&A*, *556*, A104.

Polito, V., Galan, G., Reeves, K. K., & Musset, S. (2018a). Possible Signatures of a Termination Shock in the 2014 March 29 X-class Flare Observed by IRIS. *ApJ*, *865*(2), 161.

Polito, V., Testa, P., Allred, J., De Pontieu, B., Carlsson, M., Pereira, T. M. D., Gošić, M., & Reale, F. (2018b). Investigating the Response of Loop Plasma to Nanoflare Heating Using RADYN Simulations. *ApJ*, *856*(2), 178.

Priest, E. R. (1978). The structure of coronal loops. *SoPh*, *58*(1), 57–87.

Ramesh, R., Kathiravan, C., Mithun, N. P. S., & Vadawale, S. V. (2021). Radio, X-Ray, and Extreme-ultraviolet Observations of Weak Energy Releases in the "Quiet" Sun. *ApJL*, *918*(1), L18.

Raymond, J. C., Cox, D. P., & Smith, B. W. (1976). Radiative cooling of a low-density plasma. *ApJ*, *204*, 290–292.

Reale, F. (2014). Coronal Loops: Observations and Modeling of Confined Plasma. *Living Reviews in Solar Physics*, *11*(1), 4.

Reale, F., & Orlando, S. (2008). Nonequilibrium of Ionization and the Detection of Hot Plasma in Nanoflare-heated Coronal Loops. *ApJ*, *684*(1), 715–724.

Rosner, R., Tucker, W. H., & Vaiana, G. S. (1978). Dynamics of the quiescent solar corona. *ApJ*, *220*, 643–645.

Sakamoto, Y., Tsuneta, S., & Vekstein, G. (2009). A Nanoflare Heating Model and Comparison with Observations. *ApJ*, *703*(2), 2118–2130.

Schmelz, J. T., Scopes, R. T., Cirtain, J. W., Winter, H. D., & Allen, J. D. (2001). Observational Constraints on Coronal Heating Models Using Coronal Diagnostics Spectrometer and Soft X-Ray Telescope Data. *ApJ*, *556*(2), 896–904.

Schrijver, C. J. (2007). A Characteristic Magnetic Field Pattern Associated with All Major Solar Flares and Its Use in Flare Forecasting. *ApJL*, *655*(2), L117–L120.

Shakhovskaya, N. I. (1989). Stellar flare statistics — Physical consequences. *SoPh*, *121*(1-2), 375–386.

Shibata, K., Masuda, S., Shimojo, M., Hara, H., Yokoyama, T., Tsuneta, S., Kosugi, T., & Ogawara, Y. (1995). Hot-Plasma Ejections Associated with Compact-Loop Solar Flares. *ApJL*, *451*, L83.

Shibayama, T., Maehara, H., Notsu, S., Notsu, Y., Nagao, T., Honda, S., Ishii, T. T., Nogami, D., & Shibata, K. (2013). Superflares on Solar-type Stars Observed with Kepler. I. Statistical Properties of Superflares. *ApJS*, *209*(1), 5.

Shimizu, T. (1995). Energetics and Occurrence Rate of Active-Region Transient Brightenings and Implications for the Heating of the Active-Region Corona. *PASJ*, *47*, 251–263.

Shimizu, T., Tsuneta, S., Acton, L. W., Lemen, J. R., Ogawara, Y., & Uchida, Y. (1994). Morphology of Active Region Transient Brightenings with the YOHKOH Soft X-Ray Telescope. *ApJ*, *422*, 906.

Shimizu, T., Tsuneta, S., Acton, L. W., Lemen, J. R., & Uchida, Y. (1992). Transient Brightenings in Active Regions Observed by the Soft X-Ray Telescope on YOHKOH. *PASJ*, *44*, L147–L153.

Snodgrass, H. B., & Ulrich, R. K. (1990). Rotation of Doppler Features in the Solar Photosphere. *ApJ*, *351*, 309.

Spitzer, L. (1956). *Physics of Fully Ionized Gases*.

Sturrock, P. A. (1966). Model of the High-Energy Phase of Solar Flares. *Nature*, *211*(5050), 695–697.

Svestka, Z., & Cliver, E. W. (1992). *History and Basic Characteristics of Eruptive Flares*, vol. 399, (p. 1).

Tajfirouze, E., Reale, F., Petralia, A., & Testa, P. (2016). Time-resolved Emission from Bright Hot Pixels of an Active Region Observed in the EUV Band with SDO/AIA and Multi-stranded Loop Modeling. *ApJ*, *816*(1), 12.

Teriaca, L., Falchi, A., Cauzzi, G., Falciani, R., Smaldone, L. A., & Andretta, V. (2003). Solar and Heliospheric Observatory/Coronal Diagnostic Spectrograph and Ground-based Observations of a Two-Ribbon Flare: Spatially Resolved Signatures of Chromospheric Evaporation. *ApJ*, *588*(1), 596–605.

Testa, P., De Pontieu, B., Allred, J., Carlsson, M., Reale, F., Daw, A., Hansteen, V., Martinez-Sykora, J., Liu, W., DeLuca, E. E., Golub, L., McKillop, S., Reeves, K., Saar, S., Tian, H., Lemen, J., Title, A., Boerner, P., Hurlburt, N., Tarbell, T. D., Wuelser, J. P., Kleint, L., Kankelborg, C., & Jaeggli, S. (2014). Evidence of nonthermal particles in coronal loops heated impulsively by nanoflares. *Science*, *346*(6207), 1255724.

Testa, P., De Pontieu, B., Martínez-Sykora, J., DeLuca, E., Hansteen, V., Cirtain, J., Winebarger, A., Golub, L., Kobayashi, K., & Korreck, K. (2013). Observing Coronal Nanoflares in Active Region Moss. *ApJ*, *770*(1), L1.

Tiwari, S. K., Panesar, N. K., Moore, R. L., De Pontieu, B., Winebarger, A. R., Golub, L., Savage, S. L., Rachmeler, L. A., Kobayashi, K., Testa, P., Warren, H. P., Brooks, D. H., Cirtain, J. W., McKenzie, D. E., Morton, R. J., Peter, H., & Walsh, R. W. (2019). Fine-scale Explosive Energy Release at Sites of Prospective Magnetic Flux Cancellation in the Core of the Solar Active Region Observed by Hi-C 2.1, IRIS, and SDO. *ApJ*, *887*(1), 56.

Tsuneta, S., Acton, L., Bruner, M., Lemen, J., Brown, W., Caravalho, R., Catura, R., Freeland, S., Jurcevich, B., & Morrison, M. (1991). The Soft X-ray Telescope for the SOLAR-A mission. *SoPh*, *136*(1), 37–67.

Tsuneta, S., Takahashi, T., Acton, L. W., Bruner, M. E., Harvey, K. L., & Ogawara, Y. (1992). Global Restructuring of the Coronal Magnetic Fields Observed with the YOHKOH Soft X-Ray Telescope. *PASJ*, *44*, L211–L214.

Ulyanov, A. S., Bogachev, S. A., Reva, A. A., Kirichenko, A. S., & Loboda, I. P. (2019). The Energy Distribution of Nanoflares at the Minimum and Rising Phase of Solar Cycle 24. *Astronomy Letters*, *45*(4), 248–257.

Vekstein, G., & Katsukawa, Y. (2000). Scaling Laws for a Nanoflare-Heated Solar Corona. *ApJ*, *541*(2), 1096–1103.

Vesecky, J. F., Antiochos, S. K., & Underwood, J. H. (1979). Numerical modeling of quasi-static coronal loops. I. Uniform energy input. *ApJ*, *233*(3), 987–997.

Viall, N. M., & Klimchuk, J. A. (2012). Evidence for Widespread Cooling in an Active Region Observed with the SDO Atmospheric Imaging Assembly. *ApJ*, *753*(1), 35.

Warren, H. P., Ugarte-Urra, I., Doschek, G. A., Brooks, D. H., & Williams, D. R. (2008). Observations of Active Region Loops with the EUV Imaging Spectrometer on Hinode. *ApJL*, *686*(2), L131.

Watanabe, K., Masuda, S., & Segawa, T. (2012). Hinode Flare Catalogue. *SoPh*, *279*(1), 317–322.

Withbroe, G. L., & Noyes, R. W. (1977). Mass and energy flow in the solar chromosphere and corona. *ARA&A*, *15*, 363–387.

Wu, C.-J., Ip, W.-H., & Huang, L.-C. (2015). A Study of Variability in the Frequency Distributions of the Superflares of G-type Stars Observed by the Kepler Mission. *ApJ*, *798*(2), 92.

Yi, K., Moon, Y.-J., Lim, D., Park, E., & Lee, H. (2021). Visual Explanation of a Deep Learning Solar Flare Forecast Model and Its Relationship to Physical Parameters. *ApJ*, *910*(1), 8.

Yokoyama, T., Akita, K., Morimoto, T., Inoue, K., & Newmark, J. (2001). Clear Evidence of Reconnection Inflow of a Solar Flare. *ApJL*, *546*(1), L69–L72.

Young, P. R. (2011). Instrumental Line Widths for the Narrow Slits of EIS. *EIS Software Note No. 7*.

Young, P. R. (2015). Dark Jets in Solar Coronal Holes. *ApJ*, *801*(2), 124.

Young, P. R., & Muglach, K. (2014). Solar Dynamics Observatory and Hinode Observations of a Blowout Jet in a Coronal Hole. *SoPh*, *289*(9), 3313–3329.